Spectroscopic Study of Dielectric Barrier Discharge at Atmospheric Pressure

Keiichiro URABE

January, 2012

Abstract

Spectroscopic Study of Dielectric Barrier Discharge at Atmospheric Pressure

<u>Keiichiro URABE</u>

Department of Electronic Science and Engineering, Kyoto University

January, 2012

A research area of atmospheric-pressure plasma (APP) which has a non thermal property has rapidly become widespread rather than that using low-pressure plasmas in recent years. The APPs enable us to realize not only less expensive material processes but also novel liquid and biomedical applications. However, because of their both spatially and temporally localized characteristics, there is little accumulated knowledge about discharge mechanisms and reaction kinetics in the APPs based on experimental approaches even in dielectric barrier discharge (DBD), which is one of the most widely used APP sources. For more development of the APP science, it is indispensable to make a package about discharge behaviors and mechanisms of the DBD. This dissertation presents discussions on the discharge mechanisms of the DBD operated in some electrode structures mainly investigated by laser spectroscopic measurements. In addition to the analysis of discharge behavior, potential novel applications using the DBDs are explored based on the revealed discharge mechanisms. These basic studies for the applications include development of homogeneous plasma generation inside argon (Ar) gas flows, in order to utilize different reaction kinetics from that in helium (He) gas tested in the fundamental studies

of this dissertation.

As a first step of this study, spatiotemporal structures of electron density inside parallel-plate DBD in atmospheric-pressure He gas with a small fraction of nitrogen (N_2) were investigated. A newly developed combination measurement of CO_2-laser heterodyne interferometry (CO_2-LHI) and millimeter-wave (mm-wave) transmission methods revealed spatial distributions of temporal-peak electron density. Spatiotemporal behavior of excited species and influence of the N_2 impurity were discussed from the results of also performed spectroscopic and computational studies. It was concluded from the results that the electron density was localized near the temporal cathode because of formation of a negative glow region, and total ionization frequency was maximized around 0.25% of the N_2 impurity ratio due to enhancement of a Penning ionization process between He metastable atoms and N_2 neutral molecules.

A coaxial DBD jet configuration composed of a dielectric tube, ring electrodes, and a He gas flow ejected to ambient air, recently becomes one of the widely used DBD configurations especially for biomedical applications, because it has a cm-order long plasma plume near room temperature. Unknown basic mechanisms of the plasma-plume formation in the coaxial DBD jet were investigated by the laser spectroscopic measurements. The measured behavior of N_2^+ ions by laser induced fluorescence spectroscopy (LIF) method suggested that the formation mechanisms of the plasma plume were attributed to ionization-front propagation similar to a streamer in positive corona discharge. Experiments focused on the relationships between the DBD inside the tube and the plasma plume showed that excited-species density in the plume is strongly dependent on surface-charge density accumulated by the coaxial DBD. Moreover, calculated spatiotemporal distribution of electrical potential revealed that the ionization-front propagation was ignited at the edge of accumulated charges on the inner tube surface and the

plume length was determined by potential decay speed at the ignition point.

For better understanding of discharge behavior in jet-type DBD, which had a combined electrode structure between the parallel-plate DBD and the coaxial DBD jet and was suitable to be applied to material processes, spatiotemporal structures of excited species were measured. The difference of discharge behaviors between the rise and fall timings of applied voltage was that the radial distributions of excited species had hollow shape in the rise timing, while it had more uniform shape in the fall timing, caused by the different mechanisms in positive and negative corona discharges. Also, the plasma generation by electron impact ionization became dominant near the conductive plate, clearly shown by comparison between the excited-species density and the emission intensities.

Following the basic studies on the DBDs in the atmospheric-pressure He gas, the final topics of this dissertation are control of discharge structures and potential applications of the DBDs using Ar gas flow. Generating temporally stable and spatially homogeneous DBD inside pure Ar gas has been difficult, however, the discharge structure becomes homogeneous when some molecular impurities were added into the Ar gas flow. As additive molecules to the Ar gas flow, acetone (C_3H_6O) and ammonia (NH_3) were chosen in this study because their ionization energies are a little smaller than potential energy of Ar metastable atoms and this relationship leads to Penning ionization processes similar to the discharge in He/N_2 mixed gas. In the jet-type DBD using the acetone-vapor impurity, discharge-mode transition from filamentary to glow-like modes was clearly observed around 0.3% of the acetone fraction, and the microstructure of deposited materials on the grounded plate could be changed by the discharge mode. Also, reduction and nitrization properties of the coaxial DBD in the Ar/NH_3 mixed gas flow were evaluated from the experimental analysis of the discharge region and post-discharge gas. These

experimental approaches indicated that the novel applications of the DBDs can be realized not only using He dilute gas but also using interactions between Ar gas and molecular impurities at high and atmospheric pressures.

Contents

List of Abbreviations

AC : alternating current

AFM : atomic force microscope

AOM : acousto optical modulator

APGD : atmospheric-pressure glow discharge

APP : atmospheric-pressure plasma

APPJ : atmospheric-pressure plasma jet

CCD : charge-coupled device

CO_2-LHI : CO_2-laser heterodyne interferometry

DBD : dielectric barrier discharge

DC : direct current

DUV-AS : deep-ultraviolet absorption spectroscopy

FT-IR : Fourier-transform infrared spectroscopy

FWHM : full width of half maximum

He^m : helium metastable 2^3S_1 atom

ICCD camera : intensified charge-coupled device camera

IF : interference filter

LAS : laser absorption spectroscopy

LIF : laser induced fluorescence spectroscopy

MEMS : micro electro mechanical system

mm-wave : millimeter wave

NIR : near infrared

OES : optical emission spectroscopy

PDP :   plasma display panel

PM :   photomultiplier tube

SEM :   scanning electron microscope

VUV :   vacuum ultraviolet

List of Symbols

A_{LAS} :   ratio of absorption coefficient absorbed by 2^3S_1-2^3P_2 transition to measured at 1083.036 nm in LAS measurement

$a_{\text{He}^{\text{m}}}$:   absorption coefficient of He^{m} atom [m^2]

B_v :   rotational constant of molecules [m^{-1}]

C_{LAS} :   constant value used for calculation of absolute He^{m} density

c :   speed of light ($\cong 3.00 \times 10^8$ m/s)

D_{plasma} :   duty ratio of plasma

d :   characteristic length of discharge space [m]

d_{tube} :   inner diameter of tube [m]

E_0 :   electric-field magnitude of incident probing electromagnetic wave [V/m]

E_{P1} :   electric-field magnitude of laser beam passing through AOM in CO_2-LHI measurement [V/m]

E_{P2} :   electric-field magnitude of laser beam passing through plasma in CO_2-LHI measurement [V/m]

E_{T} :   electric-field magnitude of transmitted probing electromagnetic wave [V/m]

$E_{\text{C}}^{\text{jet}}$:   electric-field magnitude calculated by finite element method simulating "Copper sheets"

electrode configuration of coaxial DBD jet [V/m]

E_W^{jet} :   electric-field magnitude calculated by finite element method simulating "Wire and sheet"

electrode configuration of coaxial DBD jet [V/m]

e :   charge of electron ($\cong 1.60 \times 10^{-19}$ C)

$f_{Penning}$:   ionization frequency of two- and three-body Penning ionization processes [Hz]

f_{total} :   total ionization frequency [Hz]

g_1 :   statistical weight of lower level of measuring electronic transition

g_2 :   statistical weight of upper level of measuring electronic transition

H_{LAS} :   ratio of peak height of measured line profile to that of hypothetical single Doppler

profile that has same integrated area as measured one

h :   Planck constant ($\cong 6.63 \times 10^{-34}$ Js)

I_0 :   transmitted intensities of probing electromagnetic wave measured without plasma [J]

$I_{IR}(t)$:   input laser power to IR detector in CO_2-LHI measurement [J]

$I_{LIF}(J)$:   LIF signal intensity of rotational quantum number J [J]

I_T :   transmitted intensities of probing electromagnetic wave measured with plasma [J]

i_C :   discharge current flowing into grounded electrode in "Copper sheets" electrode configu-

ration of coaxial DBD jet [A]

i_P :   discharge current flowing into grounded electrode in "Parallel type" electrode configura-

tion of coaxial DBD jet [A]

i_{P2} :   discharge current flowing into upstream powered electrode in "Parallel type" electrode

configuration of coaxial DBD jet [A]

i_{P3} :   discharge current flowing out from downstream powered electrode in "Parallel type"

electrode configuration of coaxial DBD jet [A]

i_S :   discharge current flowing into grounded electrode in "Spiral type" electrode configuration of coaxial DBD jet [A]

i_W :   discharge current flowing into grounded electrode in "Wire and sheet" electrode configuration of coaxial DBD jet [A]

J_{rot} :   rotational quantum number of lower level

j :   imaginary unit

K_B :   Boltzmann constant ($\cong 1.38 \times 10^{-23}$ J/K)

k_0 :   wavenumber of probing electromagnetic wave in vacuum [m^{-1}]

k_{plasma} :   wavenumber of probing electromagnetic wave in plasma [m^{-1}]

l_{plasma} :   length of plasma along probing electromagnetic wave's path [m]

m_e :   mass of electron ($\cong 9.11 \times 10^{-31}$ kg)

N_{plasma} :   refractive index of plasma

n_0 :   number density of ground state gas particles [m^{-3}]

$n_{C\text{-}C}$:   charge density in "Copper sheets" configuration of coaxial DBD jet [m^{-3}]

$n_{C\text{-}W}$:   charge density in "Wire and sheet" configuration of coaxial DBD jet [m^{-3}]

n_e :   electron density [m^{-3}]

$n_e(x)$:   spatial distribution of electron density along x axis [m^{-3}]

$n_e(t)$:   temporal evolution of electron density [m^{-3}]

$n_{e\text{-}peak}$:   temporal-peak electron density [m^{-3}]

n_{He^m} :   He^m density [m^{-3}]

P_A and P_B :   constants for gas species used in calculation of Paschen curve

p :   gas pressure [Pa]

T :   time period of one cycle of AC applied voltage [s]

T_{EM} :   transmittance of propagating electromagnetic wave's electric field

T_{e} :   electron temperature [K]

T_{g} :   gas temperature [K]

T_{rot} :   rotational temperature of molecules [K]

u_{e} :   mean thermal velocity of electron [m/K]

$V_{0\text{p}}$:   peak value of applied voltage [V]

V_{b} :   breakdown voltage [V]

$V_{\text{P-C}}^{\text{jet}}$:   electric potential calculated by finite element method simulating "Copper sheets" configuration of coaxial DBD jet [V]

$V_{\text{P-W}}^{\text{jet}}$:   electric potential calculated by finite element method simulating "Wire and sheet" configuration of coaxial DBD jet [V]

$V_{\text{PI-C}}^{\text{jet}}$:   electric potential at ignition point of ionization front calculated by finite element method simulating "Copper sheets" configuration of coaxial DBD jet [V]

$V_{\text{PI-W}}^{\text{jet}}$:   electric potential at ignition point of ionization front calculated by finite element method simulating "Wire and sheet" configuration of coaxial DBD jet [V]

α_{EM} :   attenuation constant of electromagnetic wave [m^{-1}]

β_{EM} :   phase constant of electromagnetic wave [m^{-1}]

γ_{se} :   secondary electron emission coefficient

$\Delta(N_{\text{plasma}} - 1)_{\text{e}}$:   difference of $(N_{\text{plasma}} - 1)$ caused by change of electron density

$\Delta\lambda_{\text{L}}$:   FWHM of Lorentzian component in spectrum broadening [m]

$\Delta\nu_{\text{D}}$:   FWHM of Doppler component in spectrum broadening [Hz]

$\Delta\Phi$:   phase shift of probing electromagnetic wave due to presence of plasma [rad]

$\Delta\Phi_{\text{e}}$:   electron density component in measured phase shift [rad]

$\Delta\omega_{\mathrm{AOM}}$:   modulation frequency of AOM in CO_2-LHI measurement [Hz]

ε_0 :   permittivity of vacuum ($\cong 8.85 \times 10^{-12}$ F/m)

$\varepsilon_{\mathrm{plasma}}$:   complex permittivity of plasma [F/m]

$\eta_{\mathrm{He\text{-}C}}$:   line-integrated He^m density in "Copper sheets" configuration of coaxial DBD jet [m^{-2}]

$\eta_{\mathrm{He\text{-}W}}$:   line-integrated He^m density in "Wire and sheet" configuration of coaxial DBD jet [m^{-2}]

$\eta_{\mathrm{He\text{-}S}}$:   line-integrated He^m density in "Spiral type" configuration of coaxial DBD jet [m^{-2}]

$\eta_{\mathrm{He\text{-}P}}$:   line-integrated He^m density in "Parallel type" configuration of coaxial DBD jet [m^{-2}]

κ :   rate coefficient for two- and three-body collision processes [cm^3/s or cm^6/s]

λ :   wavelength of probing electromagnetic wave [m]

ν_{m} :   momentum transfer collision frequency [Hz]

τ :   radiative lifetime of measuring transition [s]

ω_{pe} :   electron plasma frequency [rad/s]

ω_{EM} :   frequency of probing electromagnetic wave [Hz]

Chapter 1

General Introduction

1.1 Background and Basic History of Atmospheric-Pressure Plasma Engineering

A word of "plasma" has had a meaning of "ionized gaseous media" with electrical neutrality including electrons, ions, and neutral particles, since the late 1920s. [1.1] Plasmas generated in laboratories and used for industrial applications are in a category of weakly-ionized plasma, whose electron density is much less than gas-particle density. Meanwhile, strongly- and fully-ionized plasmas are only treated in research areas of nuclear fusion [1.2] and astrophysics. [1.3] The weakly-ionized plasmas are also classified based on their nature of mean thermal energies of electrons and gas particles, which are called electron temperature T_e and gas temperature T_g. When $T_e \gg T_g$ and $T_e \approx T_g$, these plasmas are named as "cold plasma" and "thermal plasma" respectively, as shown in solid lines in Fig. 1.1. [1.4] In conditions of lower gas pressure, the energies of electrons and gas particles are different and the gas temperature is kept near room temperature because of low collision frequency between electrons and gas particles. When the gas pressure increases toward atmospheric pressure, frequent collisions between electrons and gas particles makes the gas temperature high, and the electron and gas temperatures eventually become equal around several thousands °C. These temperature discussions are applicable with assumptions that the plasma is generated in a enough large volume and long time to be a static state.
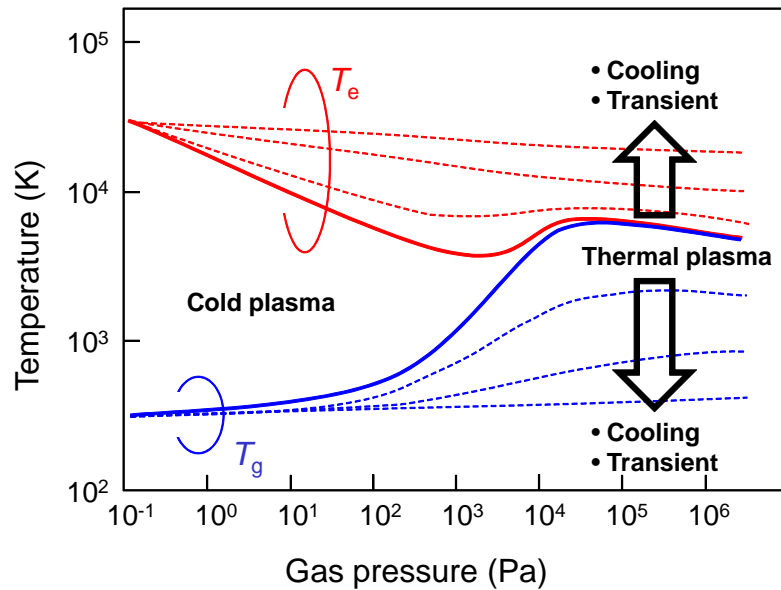
Figure 1.1   Dependences of electron temperature T_e and gas temperature T_g on gas pressure. [1.4]

Industrial applications of the plasma sources was started from development of ozonizers [1.5] and fluorescent lamps, [1.6] and the main research topic of the plasma applications in electronic engineering is now material processes. The material processes using plasmas (called "plasma processes") had spread to wide application areas, for example, etching, deposition, and surface modification processes using cold plasmas, [1.7] and welding and spraying processes using thermal plasmas. [1.8] Since the pressure ranges in which generate cold and thermal plasmas are generated easily are different as shown in Fig. 1.1, cold and thermal plasma processes have been developed in gas pressure conditions at low and atmospheric pressures, respectively. In order to achieve fine-structure formation for fabrication of semiconductors, flat displays, and MEMS devices, plasma processes using well-controlled cold plasmas generated at low pressure has occupied a main part of the plasma engineering for several decades. However, the application area of the low-pressure cold plasmas has been limited in high-value added products, because

these plasma processes need expensive vacuum chambers and take long processing time.

   In order to overcome this cost problem in the low-pressure plasma processes, there was a need to develop novel generation methods of cold plasma at high and atmospheric pressures for the material processes. It has been difficult to generate temporally stable and spatially homogeneous cold plasmas at high pressure, because of increases of the gas temperature (Fig. 1.1) and high ignition voltage decided by Paschen's law. [1.9] The Paschen's law gives a relationship between breakdown voltage V_b and a product of gas pressure and discharge space pd as follows (called a "Paschen curve")

$$V_b = \frac{P_B pd}{\ln\left\{\dfrac{P_A pd}{\ln\left(1 + 1/\gamma_{se}\right)}\right\}} \tag{1.1}$$

where P_A and P_B are the constants for gas species and γ_{se} is the secondary electron emission coefficient of electrode surfaces. Using P_A and P_B values for air, helium, nitrogen, and
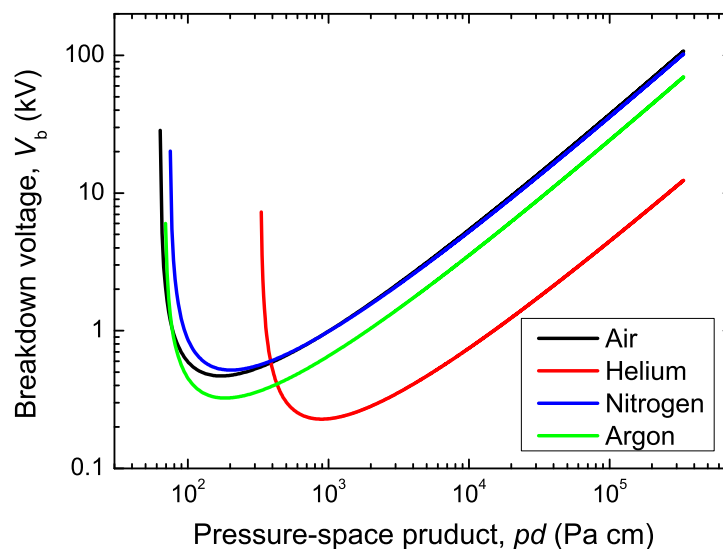

Figure 1.2   Breakdown voltage V_b of gaseous media as a function of pressure-space product pd, given by Paschen's law [1.9] and constants for each gas. [1.10]

argon, [1.10] the Paschen curves for each gas are calculated as shown in Fig. 1.2. From these Paschen curves, if the discharge space d is in several cm which is used for the low-pressure cold plasmas, the breakdown voltage V_b increased toward tens kV with increasing the gas pressure towards atmospheric pressure at 101.3 kPa.

For the generation of atmospheric-pressure cold plasmas using applied voltage in a easy-handled range, many kinds of the generation method have been developed for example decreasing discharge space d to mm or μm order (setting pd value to get minimum V_b in the Paschen curve (Fig. 1.2)). In addition to the ignition-voltage decrease, it is also important to keep the gas temperature low in the generated plasmas, in order to protect the discharge electrodes and the process objects for enough long time. For the purpose of gas-temperature reduction, some techniques are introduced such as decreasing presence time of gas particles in the discharge gap with a fast gas flow and igniting the discharge using short pulse voltage (differentiate T_e and T_g as shown in vertical arrows of Fig. 1.1), and so on.

In the end of 1980s, a group of Professor Sachiko Okazaki in Sophia University suggested a generation method of homogeneous cold plasma at atmospheric pressure (called atmospheric-pressure glow discharge: APGD), using helium dilute gas, kHz-order applied voltage, and dielectric covers on the electrode. [1.11] After this discovery, generation methods and applications of cold plasmas at atmospheric pressure (called atmospheric-pressure plasma: APP[‡]) are developed with an accelerated speed, as shown in Fig. 1.3. [1.12] Figure 1.4 shows discharge images of the APPs generated using applied voltage in a frequency range from DC to GHz order. Generation methods of the APPs can be sorted by applied-voltage waveforms, electrode

---

[‡]The phrase of "atmospheric-pressure plasma" (APP) in this dissertation means the cold plasma generated at atmospheric pressure, as widely used in the research area of plasma technology.

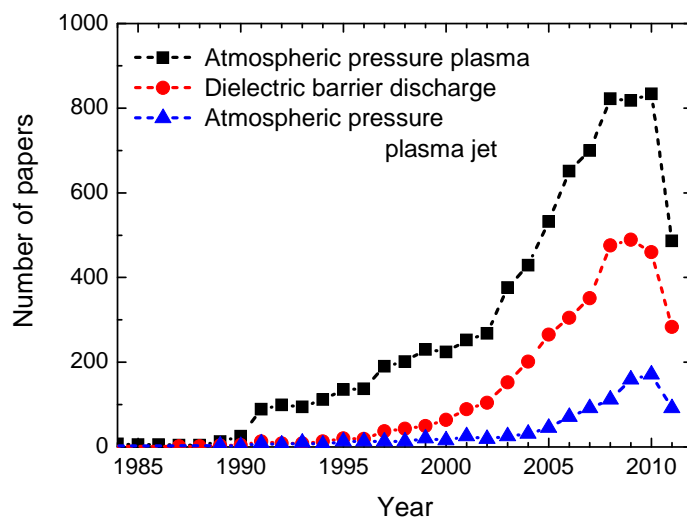Figure 1.3   Numbers of published paper including topics of atmospheric-pressure plasma (APP, black square), dielectric barrier discharge (DBD, red circle), and atmospheric-pressure plasma jet (APPJ, blue triangle), scored in Web of Science [1.12] on August 19th, 2011
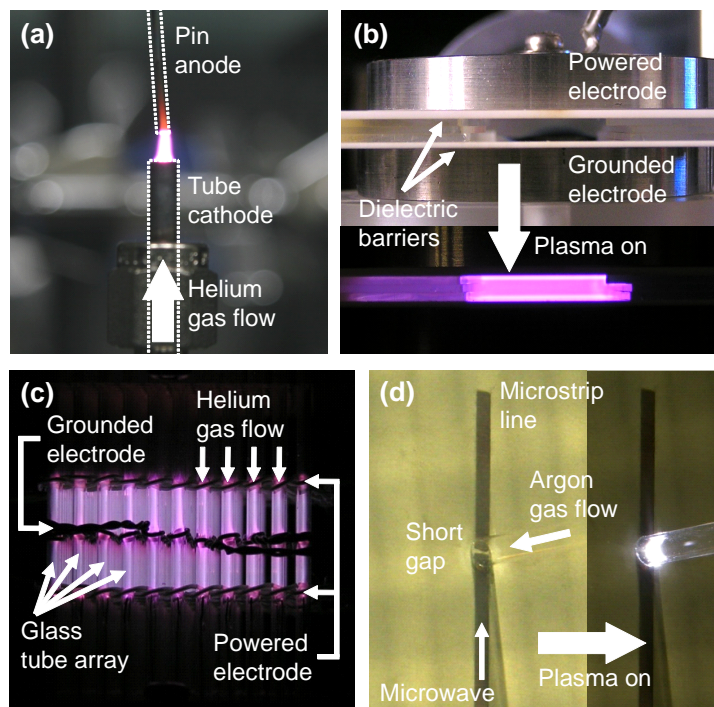

Figure 1.4   Examples images of atmospheric-pressure plasmas (APPs) generated using (a) DC, (b) kHz-, (c) MHz-, and (d) GHz-order applied voltages.

configurations, and their plasma parameters. Some of the generation methods strongly related to plasma sources tested in this dissertation are listed and briefly explained below.

Dielectric barrier discharge: DBD [1.13, 14]

In this generation method, inserting dielectric layers between metal electrodes limits automatically discharge duration below ms order, and it has an effect to keep the plasma low-gas temperature. Its gas temperature becomes lower when the gas flow in the discharge gap is faster, because the presence time of gas particles in the discharge region is decreased. The DBD is one of the most widely used APPs as shown in Fig. 1.3. Details of the DBD generation method investigated in this study will be explained in following section.

Short-pulsed discharge [1.15, 16]

Similar to the discharge-duration limitation in the DBD, the increase of gas temperature can be avoided by using applied voltage with very short pulse duration from ns to μs order. Using the short pulse voltage, the high electric power can input to the discharge in the very short time to achieve high instantaneous electron and excited-species densities inside the plasma.

Microplasma [1.4, 17]

In order to keep ignition voltage low, decreasing discharge space is an effective way as explained in Fig. 1.2, and the presence time of gas particles in the discharge space can also be shortened for the generation of cold plasmas (Fig. 1.1). Using small-scale electrode configuration made by microfabrication processes, cold plasmas can be generated continuously even

by DC, [1.18] kHz-, [1.19] MHz-, [1.20] and GHz-order [1.21] applied voltages. The most famous application of the microplasma source is plasma display panels (PDPs) used for plasma TVs. [1.22]

Atmospheric-pressure plasma jet: APPJ [1.23, 24]

To achieve more easy-handled plasma sources in open space, a novel-type APP source in a gas flow ejected from a tube (called a atmospheric-pressure plasma jet: APPJ) has been developed extensively. Many kinds of the APPJ were developed using various frequency ranges of applied voltage from DC to GHz order similar to the microplasmas. [1.25–29] Using the APPJ, the gas temperature in the plasma plume can be kept near the room temperature by the effect of fast gas-flow cooling. This low-temperature feature of the APPJ enables us to apply this cold plasma not only to the material processes and but also to novel process objects to which we cannot apply the low-pressure plasmas.

After the development of these APP sources, many kinds of material processes (thin film deposition, [1.30, 31] ashing, [1.32] surface modification, [1.33, 34] etc.) using the APP sources were reported, and these APP applications has a potential to replace the low-pressure plasma processes to both easier and less expensive ways. Also, the newly-developed microplasmas and APPJs with a spatially-localized property enabled us to realize maskless microfabrication [1.35–37] and nanomaterial synthesis processes. [1.38, 39] In addition to solid material processes, two kinds of novel plasma processes, which are never done in low-pressure gaseous media, are being developed. One of the novel processes is biomedical application. Sterilization [1.40–42] and wound healing (called "plasma medicine") using the

APP sources [1.43–45] have received extended interests in the world. The other is plasma processes with liquid media. [1.46, 47] Generating plasmas in small bubbles and on liquid surface, cleaning of polluted water, [1.48, 49] nanomaterial synthesis, [1.50, 51] and control of oxidation-reduction reactions [1.52] have been reported.[‡]

As plotted in Fig. 1.3, the generation methods and applications of the APP sources have been developed in this 21th century. However, understanding of these plasma sources from view points of discharge physics and chemical kinetics are still not enough, since their spatial and temporal localities in the APP sources makes detailed observation difficult. In order to achieve industrial applications of APPs, controlling plasma properties (such as electron density, electron temperature, and excited-species density) based on diagnostics and modeling of the plasma source, as same as design procedures of low-pressure plasmas, is indispensable. Many groups in the world including the author's group have been continuously studying "spectroscopic diagnostic" methods for measurements of plasma parameters inside the APPs, because importance of the spectroscopic methods in APP's diagnostics is higher than that in the low-pressure plasmas. The reason why the spectroscopic diagnostics are important for APPs will be explained in the next section. Constructing accurate discharge models of the APP sources based on results of the spectroscopic diagnostics and comparing the models with that based on numerical calculations are one of the most effective ways for better understanding of their discharge phenomena, and these approaches are certain to open the next door of the APP engineering tracing similar history to the low-pressure cold plasma engineering.

[‡]International conferences in these novel research fields have been started, for example "International Conference on Plasma Medicine" since 2007 and "International Workshop on Plasmas with Liquids" since 2010.

1.2 Spectroscopic Measurements for Atmospheric-Pressure Plasmas

For conventionally used low-pressure plasmas, a combination method of Langmuir probe measurement (electron density and temperature) [1.53] and computational calculations (excited species density and their behaviors) [1.54–56] has been widely performed to analyze characteristics of the plasmas and to control their plasma parameters. However, for the small-scale APPs, it is very difficult to apply the Langmuir probe method, because of its theoretical difficulty under the frequent-collision condition of gas particles to the probe at high pressure and the change of discharge conditions by inserting the conductive probe. Also, there are more variety of collision processes in the APPs than that in the low-pressure plasmas, for example three-body collision processes, and temporal non-equilibrium states are utilized to generate the cold plasmas at high pressure. For investigating characteristics of the APPs, from these facts, estimation of excited-species density only from the electron's information with an assumption of being an equilibrium state is not enough. In addition to them, since the discharge space of APPs is usually much smaller than that of the low-pressure plasmas, spatial resolution of the diagnostics method becomes crucial. Therefore, it is important to develop the APP diagnostic methods for the electron and excited-species measurements without perturbations and having good spatial resolutions.

Following these reasons, I have made a point that the development of spectroscopic measurements is indispensable for better understanding of the discharge mechanisms in the APP sources. Spectroscopic methods have the non-perturbation property and their spatial resolutions can be controlled and limited by the wavelengths of probing lights or electromagnetic waves.

Spectroscopic measurement methods for plasmas can be fallen roughly into three categories as listed below.

- To detect lights emitted from plasmas

- To use absorption, fluorescence, and scattering of lights inserted into plasmas

- To measure interaction between plasmas and electromagnetic waves

Using these phenomena, many kinds of plasma parameters can be measured, for example electron density, electron temperature, and excited-species density. In the author's group, measurement methods for excited-species density inside low-pressure cold plasmas applied to material processing have been mainly developed. For instance, hydrocarbon radicals' distributions generated in deposition processes were investigated using an infrared laser absorption spectroscopy method, [1.57] and fluorine, carbon, oxygen, nitrogen, and hydrogen atoms' densities were measured by a vacuum ultraviolet laser absorption spectroscopy and a two-photon absorption laser induced fluorescence spectroscopy methods. [1.58] For the investigation of discharge mechanisms in the small-scale APP sources, these spectroscopic methods have been modified for the high-pressure gaseous media. Fundamental physics and measurement examples of spectroscopic methods used in this study are briefly explained in the followings.

CO_2 laser heterodyne interferometry: CO_2-LHI

In order to achieve nonperturbing plasma diagnostics, a refractive index of plasma mainly decided by its electron density has been measured using electromagnetic waves as a probe. The refractive index of plasma N_{plasma} can be written as $N_{\mathrm{plasma}}^2 = 1 - \omega_{\mathrm{pe}}^2/\omega_{\mathrm{EM}}^2$ where ω_{pe} is the electron plasma frequency and ω_{EM} is the frequency of probing wave, assuming that the
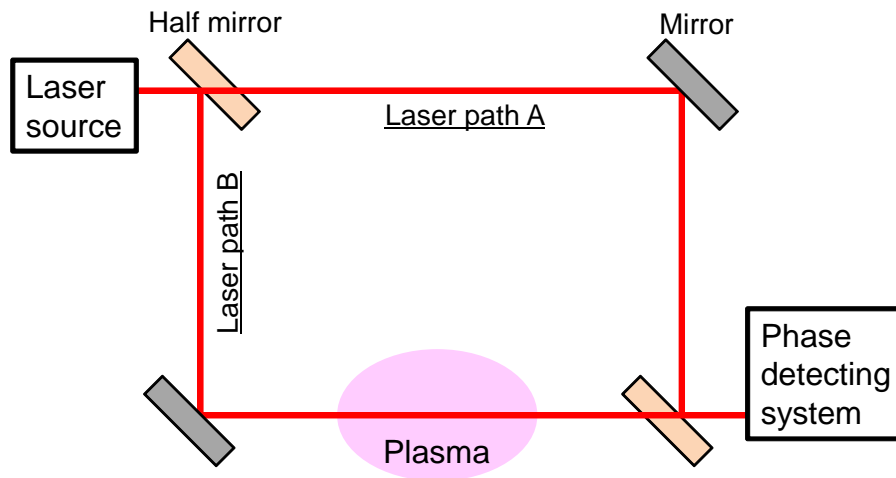
Figure 1.5   Schematic diagram of laser interferometry using Mach-Zehnder configuration for electron-density measurement inside plasma source.

probing wave's frequency is sufficiently higher than an elastic collision frequency of electron in the plasma. And this electron plasma frequency $\omega_{\mathrm{pe}} = \sqrt{n_{\mathrm{e}}e^2/\varepsilon_0 m_{\mathrm{e}}}$ where n_{e} is the electron density, e is the charge of electron, ε_0 is the permittivity of vacuum, and m_{e} is the mass of electron.

The measurements of refractive index of any medium are mostly in some forms of interferometry. Figure 1.5 is a schematic diagram of refractive-index measurement for the plasma source with a Mach-Zehnder interferometer configuration used in our study. The Mach-Zehnder configuration is one of the three typical interferometers[‡] and has two laser paths (paths A and B in Fig. 1.5) where the beams travel in only one direction. Both of the beam paths are separated from one original laser beam and the phase changes in the path B are caused by variations of the refractive index in the plasma. The merged laser beam after passing through the plasma has information of the phase differences between the two beams.

With a WKB approximation, the difference of a phase lag between the two conditions with

---

[‡]The other typical interferometers are Michelson and Fabry-Perot configurations.

and without the presence of plasma in the laser path B $\Delta\Phi$ becomes

$$\Delta\Phi = \int \left(k_{\text{plasma}} - k_0\right) \mathrm{d}l = \int \left(N_{\text{plasma}} - 1\right) \frac{\omega_{\text{EM}}}{c} \mathrm{d}l \tag{1.2}$$

where k_{plasma} is the wavenumber in plasma, $k_0 = \omega_{\text{EM}}/c$ is the wavenumber in vacuum, c is the speed of light, and $\mathrm{d}l$ is the line element along the laser path. When the proving beam has enough larger frequency than the electron plasma frequency ($\omega_{\text{EM}} \gg \omega_{\text{pe}}$), the relationship between the phase difference and the electron density is written as below. [1.59]

$$\Delta\Phi = \frac{\omega_{\text{EM}}}{c} \int \left[\sqrt{1 - \omega_{\text{pe}}/\omega_{\text{EM}}} - 1 \right] \mathrm{d}l \simeq -\frac{e^2}{2\omega_{\text{EM}}c\varepsilon_0 m_{\text{e}}} \int n_{\text{e}} \mathrm{d}l \tag{1.3}$$

To determine the electron density requires to measure precisely the output power of the interferometer, which is directly related to the phase difference $\Delta\Phi$. For the purpose of precise measurement, a heterodyne technique with additional frequency modulation in the laser path A is frequently used instead of the homodyne measurement. Also, the amplitude of the phase difference is inversely proportional to the probing wave's frequency and using lower-frequency probing wave meeting the condition of $\omega_{\text{EM}} \gg \omega_{\text{pe}}$ gains a resolution of the phase difference measurement. Therefore, a CO_2 laser beam with a frequency in far infrared is suitable to realize a reasonable detection limit of phase difference and a good spatial resolution at the same time, for the measurement of small-scale APPs. [1.60, 61]

Millimeter-wave (mm-wave) transmission method

Different from the CO_2-laser interferometry utilizing the phase shift in the probing laser beam, this millimeter-wave (mm-wave) transmission method measures absorption of the mm-wave in plasma for the measurement of electron density. The mm-waves are in a frequency range between 30 and 300 GHz, and it is suitable for the absorption measurement of the APPs because their electron plasma frequencies are also in this frequency range usually.

In plasmas with spatially uniform electron density n_e and elastic collision frequency of electron ν_m, the complex relative permittivity of plasma ε_{plasma} can be written as

$$\varepsilon_{plasma} = \varepsilon_{pr} - j\varepsilon_{pi} = 1 - \left(\frac{\omega_{pe}}{\omega_{EM}}\right)^2 \left(\frac{1}{1 + (\nu_m/\omega_{EM})^2}\right) - j\left(\frac{\omega_{pe}}{\omega_{EM}}\right)^2 \left(\frac{\nu_m/\omega_{EM}}{1 + (\nu_m/\omega_{EM})^2}\right) \quad (1.4)$$
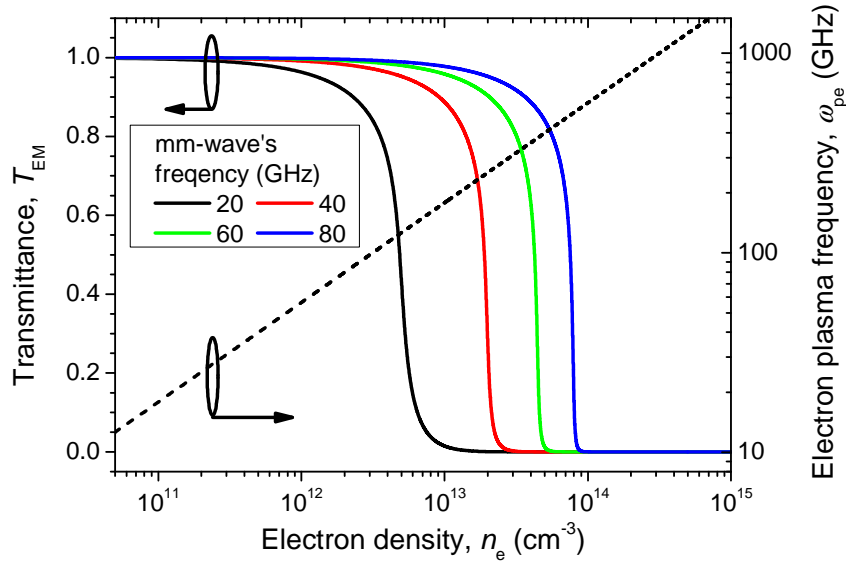

Figure 1.6 Dependences of mm-wave's transmittance T_{EM} and electron plasma frequency ω_{pe} on electron density inside plasma source, calculated with unbounded assumption. Calculation conditions are 1.0 eV of electron temperature, 300 K of gas temperature, 1.0 cm of plasma thickness, and atmospheric-pressure He gas.

where ω_{EM} is the frequency of probing mm-wave. [1.62] For a plane homogeneous mm-wave, attenuation constant α_{EM} and phase constant β_{EM} are calculated as follows

$$\alpha_{EM} = k_0 \sqrt{\frac{|\varepsilon_{plasma}| - \varepsilon_{pr}}{2}}, \quad \beta_{EM} = k_0 \sqrt{\frac{|\varepsilon_{plasma}| + \varepsilon_{pr}}{2}} \tag{1.5}$$

where $|\varepsilon_{plasma}| = \sqrt{\varepsilon_{pr}^2 + \varepsilon_{pi}^2}$ and $k_0 = \omega_{EM}/c$ is the wavenumber in vacuum. From these propagation constants, transmittance of the propagating mm-wave's electric field is given by $T_{EM} = \exp(-\alpha_{EM}l_{plasma})$ where l_{plasma} is the plasma length along the mm-wave's path, when reflections of the mm-wave at the boundaries between plasma and free space is ignored (called an unbounded assumption). Figure 1.6 shows dependences of the mm-wave's transmittance on the electron density in plasma together with the electron plasma frequency. From the calculation results, it is obviously important to choose appropriate frequency of the proving mm-wave in this measurement method.

To apply the unbounded assumption to the measurement gives us accurate electron density in the plasma, if its refractive index is close to unity. In practical use of the mm-wave transmission method, there is a need to consider the reflections of mm-wave at the plasma boundaries. Therefore, the mm-wave transmission method was developed for the APPs [1.63] using a theory including effects of the boundaries, which are reflection of the incident wave and multiple reflections inside the plasma, called a plasma slab model developed by Bachynski and Graf. [1.64]

Also, when the scale of each plasma is enough smaller than that of the probing mm-wave, it is effective to enlarge the discharge area integrating the small-scale APPs in a plane perpendicular to the mm-wave's propagating direction because of the mm-wave's diffraction limit. [1.65]

Optical emission spectroscopy: OES

As a diagnostics method of excited species inside plasma sources, an optical emission spectroscopy (OES) method has been one of the most widely used methods for a long time because of its easier-handled property than other spectroscopic methods requiring external light sources. For the measurement of emission spectra, a Czerney-Turner type spectrometer with one- or multi-channel detectors is typically used and the emission from the tested plasma sources is inserted the spectrometer through its narrow slit using a lens or an optical fiber. Wavelength resolution in the OES method is determined by a width of the slit or detecting device and a focal length of the spectrometer. In recent years, small multi-channel spectrometers with a 5- or 10-cm focal length has been developed and applied to analyze kinds of excited species inside the APPs. [1.66] For detailed analysis of the line broadenings of atomic emission or the rotational structures of molecular emission, there is still a need to prepare the large-size spectrometer with a few meter focal length. [1.67]

In addition to identification of the kinds of excited species, the OES method gives us information about vibrational and rotational distributions of electronic states in molecular emission spectra. Spectra shoen in Fig. 1.7 are examples showing vibrational distribution of N_2 emission (Fig. 1.7(a)) and rotational structure of OH emission (Fig. 1.7(b)). The distributions of molecular electronic states become corresponding to electron temperature and gas temperature, when the plasma generation has enough time duration for energy relaxation processes from electrons to molecular excited states. However, in the case of APPs, lifetimes of emissive excited molecules are much shorter than its spontaneous radiation lifetimes because of very high collision frequency with gas particles, and calculation of the electron and gas temperatures from the electronic-state distributions of molecular emissions is often inaccurate because of the short
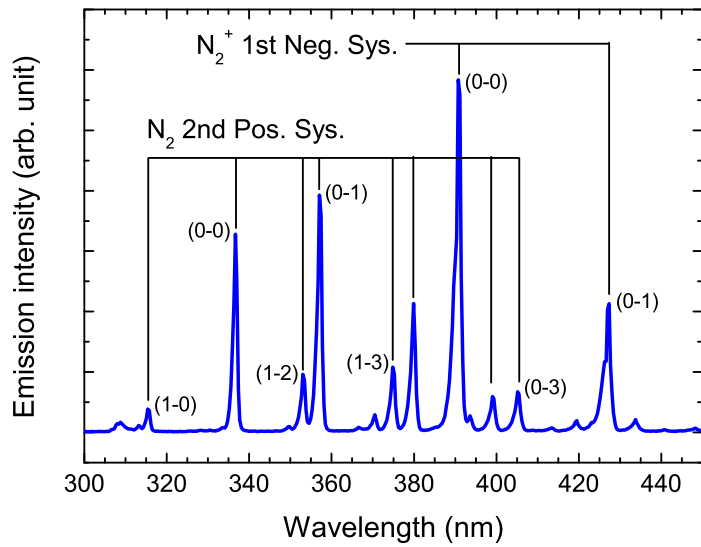
(a)
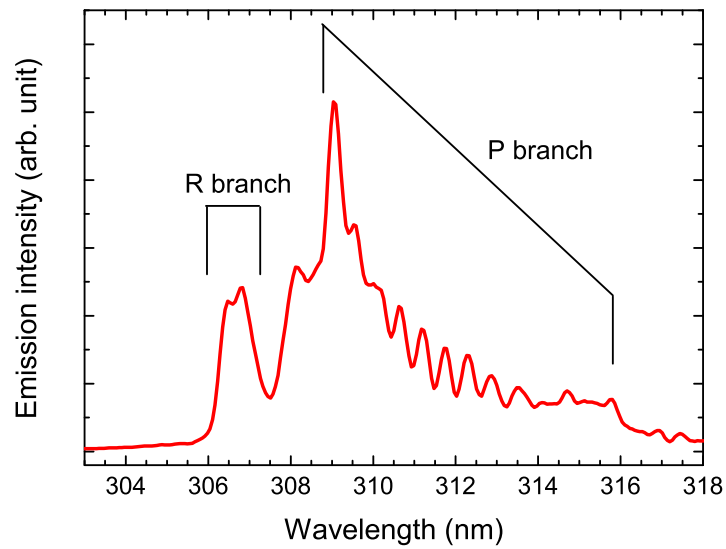
(b)

Figure 1.7   Example spectra of optical emission from atmospheric-pressure plasmas, showing (a) vibrational structures of N_2 second positive and N_2^+ first negative systems; (b) rotational structure of OH 3064Å system (0-0) band.

lifetimes.

Also, temporal evolution of the emission intensity is below ms order in the APPs driven by AC or pulsed voltage waveforms. For the purpose of measurement in these plasma sources, a intensified charge-coupled device (ICCD) camera or a photomultiplier tube having ns-order response time are connected to the spectrometer and used as detecting devices of the emission spectra. [1.68]

Laser absorption spectroscopy: LAS

A laser absorption spectroscopy (LAS) method is measurement of absolute density of excited species inside plasma sources. Wavelength of the laser beam is set at a wavelength corresponding to transition energy of the target species and the density of the lower state in the transition can be derived from the absorption ratio of the laser beam. A tunable wavelength laser source is used for the LAS measurement to get information about absorption line width of the target species, because the line width is a critical factor for the calculation of absolute density and easily changed by conditions of plasma and surrounding gas parameters. There are four line broadenings considered in the plasma measurement, which are natural, Doppler, Stark, and collision broadenings, included in the absorption spectrum, and the Doppler and collision broadenings are major components in the APPs. [1.69] The Doppler broadening is due to random thermal motion of the target species and has a Gaussian shape; the collision broadening is due to collisions between the target species and other gas particles and has a Lorentzian shape. From the Voigt-shape absorption spectrum which is the superposed spectrum of the Gaussian and Lorentzian broadenings, the absolute density of the target species can be calculated. [1.70]

Figure 1.8 shows an example of a detected signal waveform of the transmitted diode laser
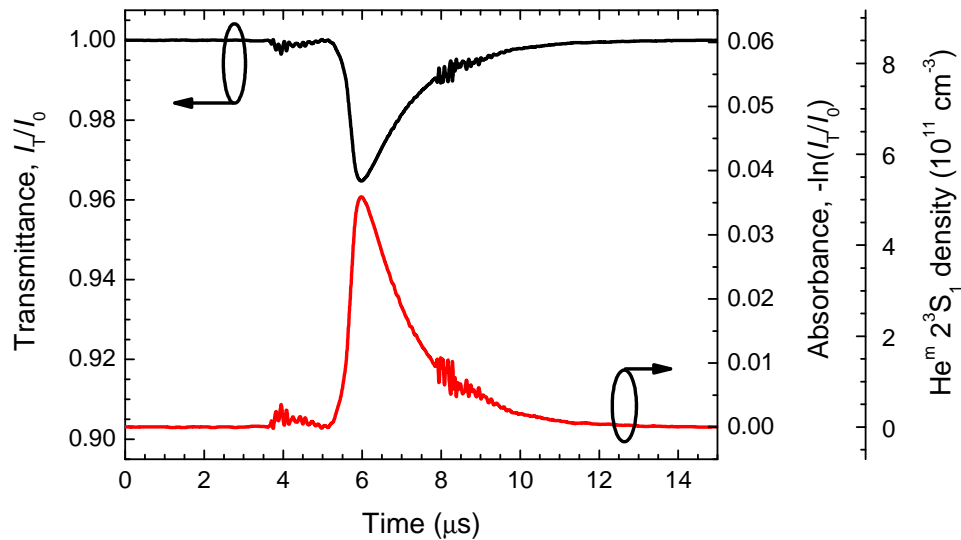
Figure 1.8   Example waveforms of transmittance I_T/I_0 and corresponding He metastable 2^3S_1 density (which is proportional to absorbance $-\ln(I_T/I_0)$) measured in atmospheric-pressure plasma by LAS method.

beam through a pulsed APP source. Absorbance in this figure was calculated from the ratio between the transmitted signal amplitudes measured with and without the discharge (I_T and I_0), and the absolute density was derived from the absorbance considering the broadening parameters explained in previous paragraph. Detectors with high sensitivity and fast response time are need for the measurement of small-scale APPs because the absorption length becomes short and the temporal evolution of excited-species density is in μs or ns order.

The LAS method has a good feature to be able to detect the presence of excited states whose emissive relaxations are forbidden such as metastable states and grounded states of ions and radicals. A near infrared (NIR) tunable diode laser source with an external cavity system was used in this study for the measurement of excited-atom density in the metastable states. For the measurement of atomic density in the grounded states, for example F and C atoms, vacuum ultraviolet (VUV) laser beam made by a four wave mixing process was required because the

smallest transition energies from the ground state to excited state are corresponding to the VUV wavelength range in these atoms. [1.71]

Laser induced fluorescence spectroscopy: LIF

A laser induced fluorescence spectroscopy (LIF) method is another measurement method of excited-species density having no emissive transition pathway to lower states. In this measurement, relative density of the target species can be estimated from increments of the spontaneous emission from the tested plasma source whose intensity is increased by an inserted laser beam for excitation of the target species. The excitation and fluorescence emission schemes are shown in Fig. 1.9. When the excitation and detection wavelength are set at one same transition (two-level system, Fig. 1.9(a)), there is a need to remove stray light signal of the excitation laser beam from detected total emission intensity carefully. Compared with the two-level system, a three-level system (Fig. 1.9(b)) is easier to remove the influence of the excitation laser beam by using a wavelength filter. Even in the three-level system, there is spontaneous emission in the detected wavelength by electron excitation in the plasma, and a boxcar averager is used to limit
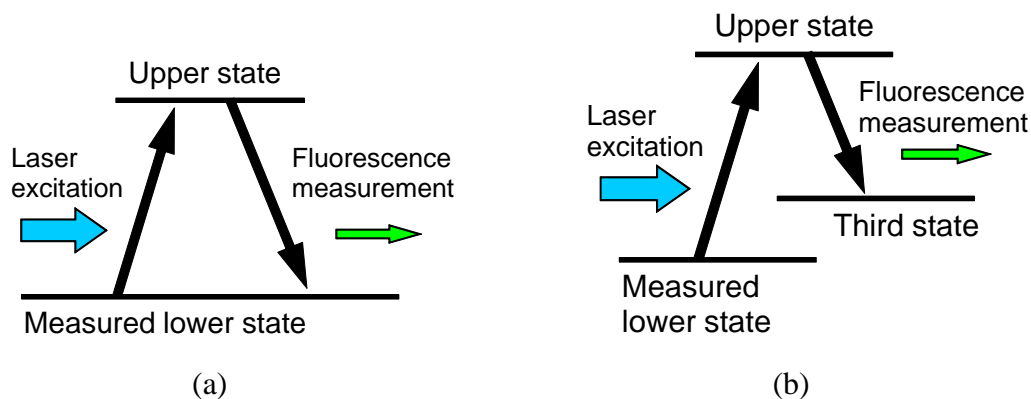
Figure 1.9   Schematic diagrams of excited levels and transitions used in laser induced fluorescence method in (a) two-level and (b) three-level systems.

the detecting time to the pulse laser inserting.

For the analysis of electronic states of the target species using its line shape and rotational distribution, the wavelength of excitation laser beam is scanned, and the spectrum is recorded as the temporal evolution of detected fluorescence intensity. A dye laser source excited by excimer or YAG laser beams is typically used for the LIF measurement because of its wide wavelength tuning availability and high laser power. In order to calculate absolute density of the target species, there is a need to evaluate all energy relaxation processes of the upper state and a detection solid angle in the LIF measurement system, in order to know the fraction of target species which emit the photon detected by the LIF measurement. [1.72] This precise evaluation is very difficult both theoretically and experimentally, therefore, reference LIF measurements of other species having similar electronic transition systems to the target species, whose density can be measured in other way, are usually used for the absolute-density measurement. [1.73] Especially in high-pressure plasma measurement, collision energy-relaxation processes of the upper-state species, which are very different in each species, have to be included in the calculation. [1.74] For the measurement of excited species having only transitions which need higher excitation energy than the photon energy of dye lasers, frequency doubling [1.75] or two-photon absorption [1.58] methods are applied to the LIF measurement.

Utilizing these spectroscopic measurement methods, we can get accurate information of electrons and excited species densities in the APPs. Spatiotemporal behaviors and discharge mechanisms in the DBDs are discussed from the spectroscopic measurement results in this dissertation.

1.3 Generation Methods of Dielectric Barrier Discharge (DBD)

Discussions in this dissertation are focused on investigating discharge mechanisms and exploring potential applications of the dielectric barrier discharge (DBD), which is one of the most widely used APP generation methods in recent years as shown in Fig. 1.3. For getting stable cold plasmas inside high-pressure gaseous media, it is essential to stop the discharge in short time duration for several hundreds ns. The DBD has an automatic scheme of the discharge termination by presence of the dielectric barriers between the discharge gap. Because of the presence of dielectric barrier layers, charged particles (electrons and ions) cannot flow into the metallic electrodes directly but they are stored on the barrier surface. This accumulated charges form an electric field having a reverse polarity with that formed by the applied voltage. Then, the reverse-voltage amplitude increases as the discharge current flows, and the discharge is terminated by the decrease of gap voltage which is superposition between the applied and reverse voltages. Using this effect of the automatic discharge termination by the dielectric barrier, the DBD's gas temperature can be kept below several hundreds °C, and it does not require an expensive power supply applying the short pulse voltage.

The charge accumulation in the DBD driven by an AC high voltage also has additional effect to decrease its sustain voltage. This is because that the reverse voltage formed by the accumulated charges becomes forward voltage added to the applied voltage when the voltage polarity changed to be opposite after one discharge pulse. This forward voltage reduces the applied-voltage amplitude required for the discharge ignition in each discharge pulse. Also, the sustain voltage is kept lower than the discharge using bare-metal electrodes.
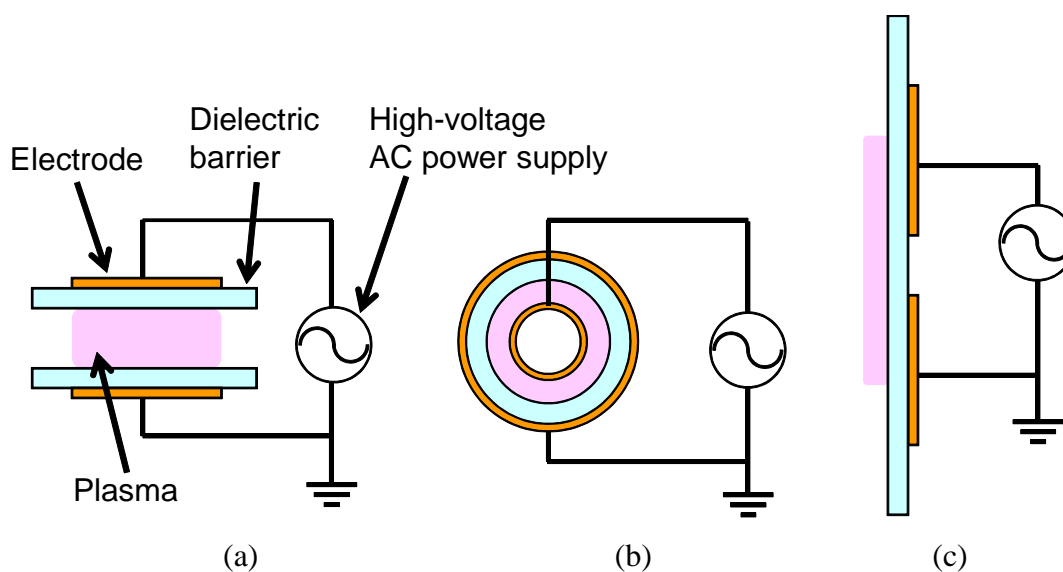
Figure 1.10   Two-dimensional schematic diagrams of electrode structures used for dielectric barrier discharge, (a) parallel plate type, (b) tubular type, and (c) surface barrier discharge type.

Figure 1.10 introduces three examples of the electrode configuration typically used for the DBD generation. A parallel-plate electrode configuration (Fig. 1.10(a)) is the simplest configuration composed of two plate electrodes covered by the dielectric barriers. Materials for the dielectric barrier are chosen in dielectric materials having a good heat resistance, for example glass (SiO_2) and alumina (Al_2O_3) plates. Plasmas are generated between the two dielectric barriers, and the area of the barrier is larger than that of the electrode to prevent formation of the discharge path going around the barrier and connecting the metal electrodes directly. This electrode type have been used for many kind of applications since the discovery of atmospheric-pressure glow discharge used this configuration, [1.11, 76] and the discharge area can be enlarged easily for large-area processes. [1.77] Weak points of this electrode configuration are that it has to be operated in a chamber system to control gas composition inside the discharge region and its process objectives are required to be plane and thin because its electrode gap is typically in a few mm. In order to respond well to needs for specific industrial applications,
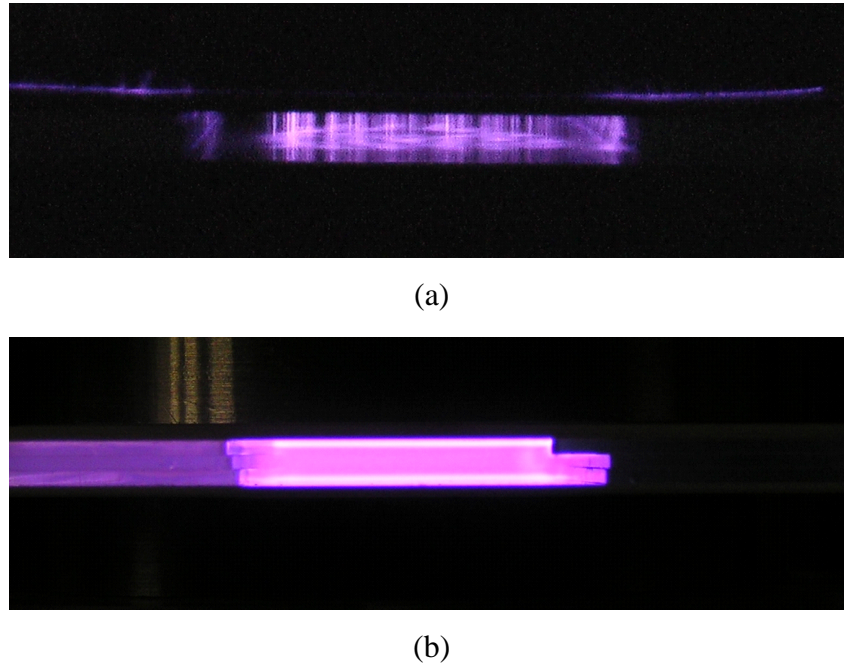
(a)

(b)

Figure 1.11   Photographs of discharge emission using parallel-plate dielectric barrier discharge configuration, (a) in filamentary discharge mode inside atmospheric air and (b) in glow-like discharge mode using helium gas flow at atmospheric pressure.

many types of the DBD electrode configuration have been developed. Representative examples are a tubular configuration (Fig. 1.10(b)) for gas cleaning processes inside the tube [1.78] and a surface-barrier discharge configuration (Fig. 1.10(c)) for micro-scale discharges inside the PDPs. [1.79]

Discharge behaviors in the DBD can be classified into two kinds of discharge mode, which are filamentary and glow-like modes, as shown in Fig. 1.11. The filamentary discharge has many thin filaments bridging the discharge gap in parallel, and their movement and discharge current show random behaviors (Fig. 1.11(a)). Under some specific conditions, the filaments are self-aligned in stable crystal structures called as a self organization. [1.80] On the other hand, the glow-like discharge mode can fill whole discharge gap by the homogeneous plasma (Fig. 1.11(b)). Generation of the glow-like discharge at atmospheric pressure without using ns-order
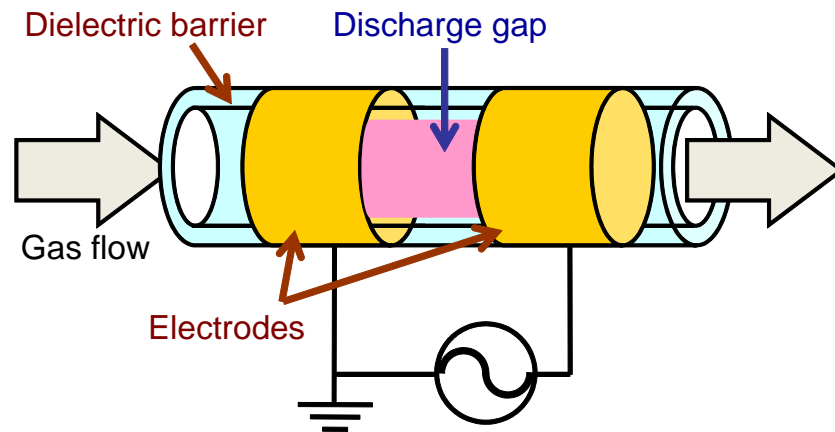
Figure 1.12   Schematic diagrams of coaxial dielectric barrier discharge.

pulse voltage is reported only in pure helium gas [1.11] and argon gas with some molecular impurities. [1.81, 82] Although generation mechanisms of the glow-like DBDs have been investigated from both view points of experimental studies and computational calculations, there is still no clear explanation for constructing the homogeneous structure in helium gas and no simple technique to generate glow-like DBD in nitrogen and atmospheric air. The study in this dissertation has approached this important topic in the research area of APPs by acquisition of detailed spatiotemporal behaviors of electron and excited-species densities using the spectroscopic methods.

In our Plasma Physics and Technology Laboratory in Kyoto University, an electrode configuration of "coaxial DBD" has been developed and applied to the material processes. As shown in Fig. 1.12, a gas flow inside a tubular dielectric material and an electric field formed by applied voltage to ring electrodes around the tube are both along the same axis. Using this configuration, there is no need to prepare vacuum chamber and is a cooling effect of the gas flow on the electrodes and the dielectric barriers, and it is easy to apply it to material processes by placing target materials in front of the exit of the dielectric tube. Also, compared with the tubular DBD

<div align="center">(a)   (b)</div>
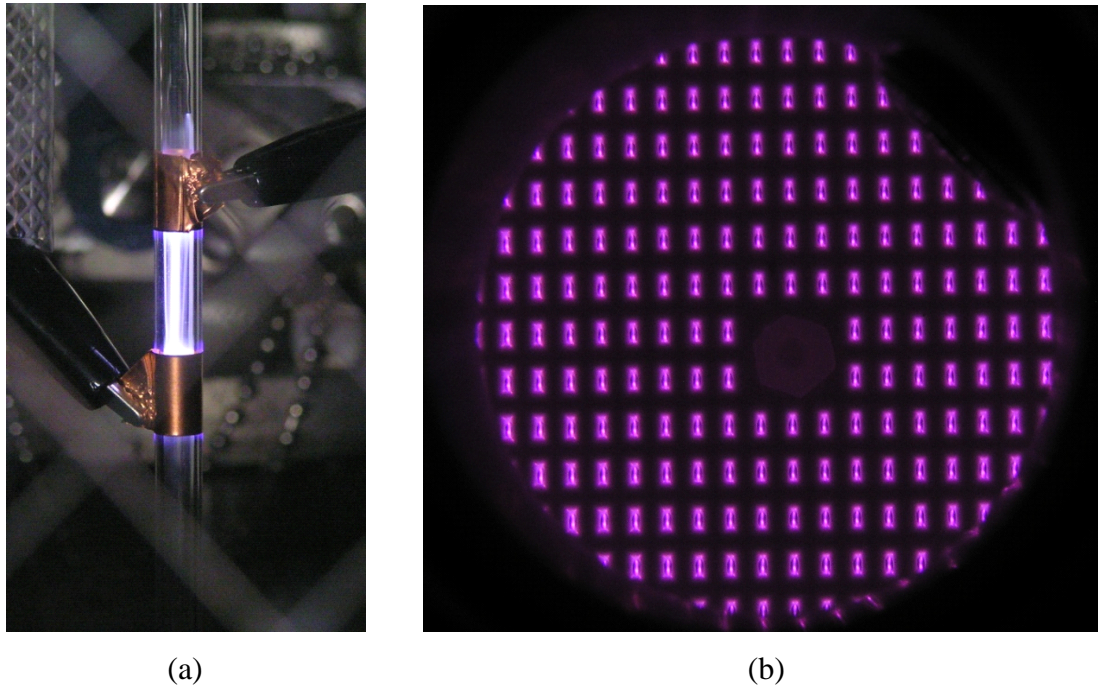
Figure 1.13   Photographs of discharge emission using coaxial dielectric barrier discharge configuration, (a) inside glass tube in argon gas flow and (b) using array of micro coaxial DBD in helium gas flow.

shown in Fig. 1.10(b), damages of the electrodes and contamination of metal particles into the gas flow are prevented by the dielectric tube in the coaxial DBD. The coaxial DBDs in glass tubes can be built very easily in tubular systems for gaseous chemical processes as shown in Fig. 1.13(a). [1.83] For large-area material processes, it is effective to integrate small coaxial DBDs in array structure shown in Fig. 1.13(b). [1.19] It has been already reported that the coaxial DBD can be applied to fast deposition processes of oxide films at atmospheric pressure. [1.84]

In 2005, it was found that a plume-like emissive region in a cm order is elongated along a helium gas flow ejected from a glass tube into atmospheric air, when the coaxial DBD is driven near the tube exit as shown in Fig. 1.14. [1.85] Features of this novel plasma jet compared with other APPJs are a longer plume length effused into ambient air than that in mm order of others and a very low gas temperature which we can touch the plume directly. It is also well known that
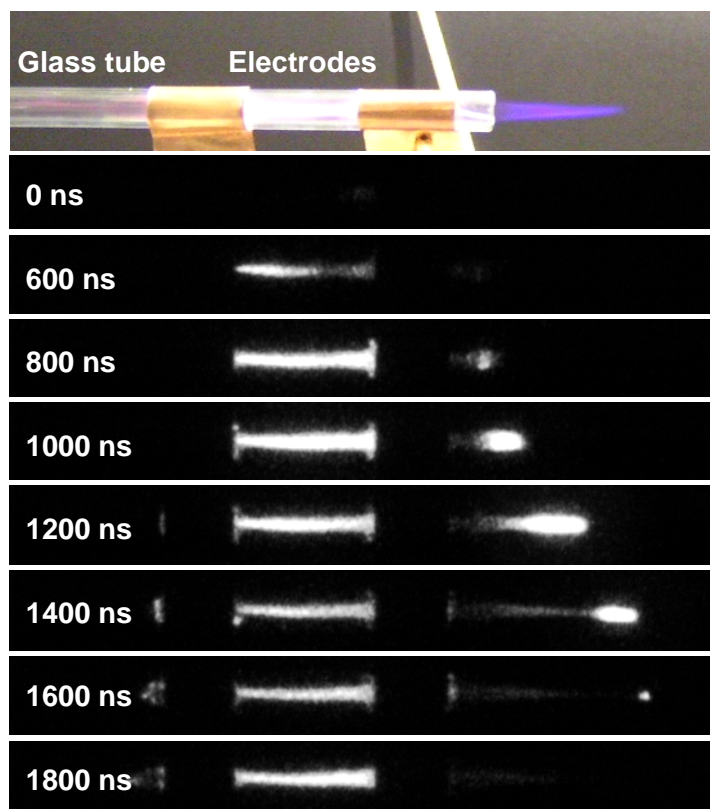
Figure 1.14   Photograph of electrode configuration and discharge emission in coaxial DBD plasma jet using helium gas ejected into atmospheric air, together with temporally-resolved images in rise timing of applied voltage observed by ICCD camera.

(a)   (b)
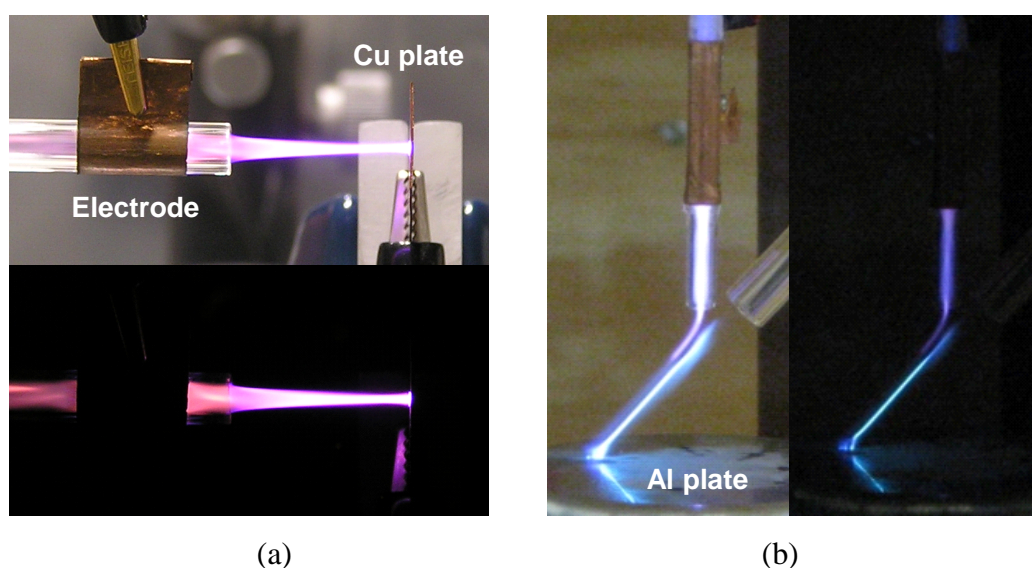
Figure 1.15   Photographs of electrode configuration and discharge emission structure in jet-type DBD using (a) single helium gas flow and (b) crossed flows of vertical pure helium and tilted argon/acetone mixed gases.

a bunched emission like a "plasma bullet" ejected from the tube exit is observed in the rise tim-ing of applied voltage by an ICCD camera and it has a velocity of several tens of km/s, which is much faster than the gas flow speed. [1.86–88] For applications of the APPJ to biomedical pro-cesses and sterilization, which recently attract much interest in the world, [1.24, 44] discharge mechanisms and plasma parameters inside the plasma plume have to be accurately determined for the assurance of safety. This unrevealed formation mechanisms of the plasma plume in the plasma jet driven by the coaxial DBD (called as a "coaxial DBD jet" in this dissertation) are investigated in chapters 3 and 4.

In addition to the coaxial DBD jet configuration, when a conductive is placed plate in front of the plasma plume, the discharge emission intensity and current amplitude in the plume were increased drastically as you can see in difference between Figs. 1.14 and 1.15(a). Applying the coaxial DBD jet to the material processes, [1.89] the discharge mode often automatically changed into this high-current mode; however, there was no study about the difference of dis-charge characteristics between the two discharge modes before the author's paper explained in this dissertation. [1.90] Also, as shown in Fig. 1.15(b), the gas flow for the discharge ignition at the powered electrode and the flow for the material process touching the substrate can be con-trolled independently in this jet-type DBD using crossed gas flows between the tube exit and the substrate. This novel gas-flow configuration has a good potential to be applied to deposition processes, [1.35] and it cannot be realized other types of the DBD generated in a closed space.

In this dissertation, fundamental discharge mechanisms of the DBDs, for instance ignition and ionization processes, are revealed by experimental approaches. Specific tested electrode configurations of the DBD and the spectroscopic measurement methods used for the discussion are introduced in the following section.

1.4   Purpose of This Study

For more development of atmospheric-pressure plasma engineering, as mentioned in above sections, it is indispensable to make a package about discharge behavior and mechanisms inside the dielectric barrier discharge operated at atmospheric pressure from experimental measurement results. Using interacting phenomena between lights (electromagnetic waves) and plasmas, for example absorption and phase shift of probing lights, spatiotemporal behaviors of electrons and excited species can be measured by appropriate spectroscopic methods for each species. In this study, the mainly used measurement methods are based on light-inserting spectroscopic techniques which can directly measure the target excited species, and these sophisticated spectroscopy's results can be referred to the readers' plasma sources through contents comparing measurement results with optical emission spectra in this dissertation.

In addition to the investigation of discharge mechanisms, potential applications using the DBDs are discussed and explored based on the revealed discharge mechanisms in this dissertation. This basic study for the applications includes development of homogeneous discharge generation inside argon gas, which is less expensive than helium gas in Japan, to reduce costs for conventional material processes and to utilize different reaction kinetics from the He-gas DBDs.

This dissertation is separated into 6 chapters including this introducing chapter. For the ease of understanding, the chapters are classified as the kinds of tested plasma sources driven by the DBD scheme, and ordered from fundamental to application studies. Specific purposes and tested plasma sources treated in each chapter of are as follows.

In chapter 2, formation mechanisms of electron-density distribution in a parallel-plated DBD

are discussed. The electron-density distribution was measured by a newly developed combination method of CO_2-laser heterodyne interferometry and millimeter-wave transmission. The discharge mechanisms in the parallel-plate DBD, which is the most basic DBD configuration, are confirmed in comparison with measured excited-species distributions and numerical calculation results of ionization frequency.

In chapter 3, from measurement results of the laser-aided spectroscopic methods, basic discharge mechanisms in a plasma jet driven by a coaxial DBD (coaxial DBD jet) are investigated. This type of plasma jet is recently developed and applied to material and biomedical processes; however, the discharge mechanisms forming its plasma plume have not been clarified yet. The formation mechanisms of the plasma plume are discussed from measured behavior of N_2^+ ions and revealed relationships between the coaxial DBD inside the tube and the plasma plume.

In chapter 4, in order to apply the coaxial DBD jet to material processes, differences of discharge behaviors between with and without a conductive substrate in front of the plasma plume are discussed. The driving mode, when a grounded conductive plate is placed there, is called a jet-type DBD. Mechanisms of discharge ignition and maintaining stable discharge in a cm-order longer gap than the parallel-plate DBD are investigated, through the comparison between spatiotemporal discharge structures of the jet-type DBD with and without the conductive plate.

In chapter 5, novel material-process applications at atmospheric pressure are tried to be realized by developing generation methods of glow-like DBDs mainly using inexpensive argon gas flows. Influence of small fraction of molecular impurity put into the argon flow on the glow-like discharge generation and criteria of a discharge-mode transition from filamentary and glow-like modes are investigated. Also, trial experimental results of hydrocarbon material's deposition by the jet-type DBD using an argon/acetone mixed gas flow and surface modification by the

coaxial DBD using an argon/ammonia flow are introduced in this chapter.

Finally in chapter 6, following whole experimental and discussing results, the total discharge mechanisms of the DBD and future perspectives of the DBD engineering are written up as concluding remarks.

References

[1.1] L. Tonks and I. Langmuir: Phys. Rev. **33** (1929) 195.

[1.2] D. J. Rose and M. Clark Jr.: *Plasmas and Controlled fusion* (Wiley, New York, 1961).

[1.3] E. N. Parker and G. Burbidge: in *Plasma Dynamics*, ed. F. H. Clauser (Addison-Wesley Publishing, Massachusetts, 1960).

[1.4] K. Tachibana: IEEJ Trans. Electr. Electron. Eng. **1** (2006) 145.

[1.5] E. W. von Siemens: Poggendorff's Ann. Phys. Chem. **102** (1857) 66.

[1.6] P. C. Hewitt: US Pattent 682,699 (1891).

[1.7] M. A. Lieberman and A. J. Lichtenberg: *Principles of Plasma Discharges and Material Processing* (Wiley, New York, 1994).

[1.8] C. E. Jackson and M. A. Levinsterin: in *Welding Handbook*, ed. A. L. Phillips (American Welding Society, Miami, 1969) 6th ed.

[1.9] F. Paschen: Ann. Physik **273** (1889) 69.

[1.10] E. Nasser: *Fundamentals of Gaseous Ionization and Plasma Electronics* (John Wiley & Sons, New York, 1971).

[1.11] S. Kanazawa, M. Kogoma, T. Moriwaki, and S. Okazaki: J. Phys. D **21** (1988) 838.

[1.12] Thomson Reuters: Web of Science (version 5.3) [http://apps.webofknowledge.com]

[1.13] U. Kogelschatz: Plasma Chem. Plasma Process. **23** (2003) 1.

[1.14] A. Chirokov, A. Cutsol, and A. Fridman: Pure Appl. Phys. **77** (2005) 487.

[1.15] P. Tardiveau, N. Moreau, S. Bentaleb, C. Postel, and S. Pesquier: J. Phys. D **42** (2009) 175202.

[1.16] J. L. Walsh and M. G. Kong: Appl. Phys. Lett. **91** (2007) 251504.

[1.17] K. H. Becker, K. H. Schoenbach, and J. G. Eden: J. Phys. D **39** (2006) R55.

[1.18] K. H. Schoenbach, M. Moselhy, W. Shi, and R. Bentley: J. Vac. Sci. Technol. A **21** (2003) 1260.

[1.19] O. Sakai, Y. Kishimoto, and K. Tachibana: J. Phys. D **38** (2005) 431.

[1.20] J. A. Hopwood: J. Microelectromech. Syst. **9** (2000) 309.

[1.21] T. Takahashi, Y. Takao, K. Eriguchi, and K. Ono: Phys. Plasmas **16** (2009) 083505.

[1.22] J. P. Boeuf: J. Phys. D **36** (2003) R53.

[1.23] A. Schutze, J. Y. Jeong, S. E. Babayan, J. Park, G. S. Selwyn, and R. F. Hicks: IEEE Trans. Plasma Sci. **26** (1998) 1685.

[1.24] M. Laroussi and T. Akan: Plasma Process. Polym. **4** (2007) 777.

[1.25] N. Shirai, H. Shito, S. Ibuka, and S. Ishii: Appl. Phys. Express **2** (2009) 076001.

[1.26] J. L. Walsh, J. J. Shi, and M. G. Kong: Appl. Phys. Lett. **88** (2006) 171501.

[1.27] V. Leveille and C. Coulombe: Plasma Sources Sci. Technol. **14** (2005) 467.

[1.28] T. Ichiki, T. Koidesawa, and Y. Horiike: Plasma Sources Sci. Technol. **12** (2003) S16.

[1.29] J. Kim, M. Katsurai, D. Kim, and H. Ohsaki: Appl. Phys. Lett. **93** (2008) 191505.

[1.30] S. Kanazawa, M. Kogoma, S. Okazaki, and T. Moriwaki: Nucl. Instrum. Methods Phys. Res. B **37/38** (1989) 842.

[1.31] G. R. Nowling, S. E. Babayan, V. Jankovic and R. F. Hicks: Plasma Sources Sci. Technol. **11** (2002) 97.

[1.32] K.H. Han, J. G. Kang, H. S. Uhm, and B. K. Kang: Curr. Appl. Phys. **7** (2007) 211.

[1.33] F. Massines and G. Gouda: J. Phys. D **31** (1998) 3411.

[1.34] H. Inui, K. Takeda, H. Kondo, K. Ishikawa, M. Sekine, H. Kano, N. Yoshida, and M Hori: Appl. Phys. Express **3** (2010) 126101.

[1.35] Y. Ito, K. Urabe, N. Takano, and K. Tachibana: Appl. Phys. Express **1** (2008) 067009.

[1.36] T. Ideno and T. Ichiki: Thin Solid Films **506-507** (2006) 235.

[1.37] R. Kakei, A. Ogino, F. Iwata, and M. Nagatsu: Thin Solid Films **518** (2010) 3457.

[1.38] Z. Yang, H. Shirai, T. Kobayashi, and Y. Hasegawa: Thin Solid Films **515** (2007) 4153.

[1.39] T. Nozaki, K. Sasaki, T. Ogino, D. Asahi, and K. Okazaki: Nanotechnology **18** (2007) 235603.

[1.40] M. Laroussi: IEEE Trans. Plasma Sci. **30** (2002) 1409.

[1.41] E. Stoffels, Y. Sakiyama, and D. B. Graves: IEEE Trans. Plasma Sci. **36** (2008) 1441.

[1.42] S. Ikawa, K. Kitano, and S. Hamaguchi: Plasma Process. Polym. **7** (2010) 33.

[1.43] G. Fridman, G. Friedman, A. Gutsol, A. B. Shekhter, V. N. Vasilets, A. Fridman: Plasma Process. Polym. **5** (2008) 503.

[1.44] M. G. Kong, G. Kroesen, G. Morfill, T. Nosenko, T. Shimizu, J. van Dijk, and J. L. Zimmermann: New J. Phys. **11** (2009) 115012.

[1.45] J. Ehlbeck, U. Schnabel, M. Polak, J. Winter, T. von Woedtke, R. Brandenburg, T. von dem Hagen, and K.-D. Weltmann: J. Phys. D **44** (2011) 013002.

[1.46] P. Bruggeman and C. Leys: J. Phys. D **42** (2009) 053001.

[1.47] N. Y. Babaeva and M. J. Kushner: Plasma Sources Sci. Technol. **18** (2009) 035009 and 035010.

[1.48] H. Akiyama: IEEE Trans. Dielectr. Electr. Insul. **7** (2000) 646.

[1.49] A. Yamatake, J. Fletcher, K. Yasuoka, and S. Ishii: IEEE Trans. Plasma Sci. **34** (2006) 1375.

[1.50] K. Baba, T. Kaneko, and R. Hatakeyama: Appl. Phys. Express **2** (2009) 035006.

[1.51] H. Furusho, K. Kitano, S. Hamaguchi, and Y. Nagasaki: Chem. Mater. **21** (2009) 3526.

[1.52] O. Sakai, T. Morita, N. Sano, T. Shirafuji, T. Nozaki, and K. Tachibana: J. Phys. D **42** (2009) 202004.

[1.53] J. D. Swifr and M. J. R. Schwar: *Electrical Probes for Plasma Diagnostics* (Iliffe Books, London, 1970).

[1.54] T. Makabe: *Plasma Electronics* (Baifukan, Tokyo, 1999) [in Japanese].

[1.55] P. L. G. Ventzek, R. J. Hoekstra, and M. J. Kushner: J. Vac. Sci. Technol. B **12** (1994) 461.

[1.56] R. A. Stewart, P. Vitello, and D. B. Graves: J. Vac. Sci. Technol. B **12** (1994) 478.

[1.57] K. Tachibana, M. Nishida, H. Harima, and Y. Urano: J. Phys. D **17** (1984) 1727.

[1.58] K. Tachibana: Plasma Souces Sci. Technol. **11** (2002) A166.

[1.59] I. H. Hatchinson: *Principles of Plasma Diagnostics* (Cambridge University Press, Cambridge, 2002) 2nd ed.

[1.60] F. Leipold, R. H. Stark, A. El-Habachi, and K. H. Schoenbach: J. Phys. D **33** (2000) 2268.

[1.61] J.-Y. Choi, N. Takano, K. Urabe, and K. Tachibana: Plasma Sources Sci. Technol. **18** (2009) 035013.

[1.62] M. P. Bachynski, T. W. Johnston, and I. P. Shkarofksy: Proc. I.R.E. **48** (1960) 317.

[1.63] K. Tachibana, Y. Kishimoto, and O. Sakai: J. Appl. Phys. **97** (2005) 123301.

[1.64] M. P. Bachynski and K. A. Graf: RCA Rev. **25** (1964) 3.

[1.65] O. Sakai, T. Sakaguchi, Y. Ito, and K. Tachibana: Plasma Phys. Control. Fusion **47** (2005) B617.

[1.66] *for example* Ocean Optics Inc. [http://www.oceanoptics.com]

[1.67] C. Laux, T. G. Spence, C. H Kruger, and R. N. Zare: Plasma Sources Sci. Technol. **12**

(2003) 125.

[1.68] N. K. Bibinov, A. A. Fateev, and K. Wiesemann: J. Phys. D **34** (2001) 1819.

[1.69] H. R. Griem: *Spectral Line Broadening by Plasmas* (Academic Press, New York, 1974).

[1.70] E. D. Hinkley, K. W. Nill, and F. A. Blum: in *Laser Spectroscopy of Atoms and Molecules*, ed. H. Walter (Springer, Berlin, 1976).

[1.71] K. Tachibana and H. Kamisugi: Appl. Phys. Lett. **74** (1999) 2390.

[1.72] V. M. Donnelly, D. L. Flamm, and G. Collins: J. Vac. Sci. Technol. **21** (1982) 817.

[1.73] N. Abramzon, R. B. Siegal, and K. Becker: J. Phys. B **32** (1999) L247.

[1.74] K. Niemi, V. Schulz-von der Gathen, and H. F. Dobele: Plasma Sources Sci. Technol. **14** (2005) 375.

[1.75] K. Tachibana, T. Mukai, and H. Harima: Jpn. J. Appl. Phys. **30** (1991) L1208.

[1.76] F. Massiness, A. Rabehi, P. Decomps, R. B. Gadri, P. Segur, and C. Mayoux: J. Appl. Phys. **83** (1998) 2950.

[1.77] J. L. Walsh, Z. Cao, and M. G. Kong: IEEE Trans. Plasma Sci. **36** (2008) 1314.

[1.78] S. Kado, Y. Sekine, T. Nozaki, and K. Okazaki: Catarysis Today **89** (2004) 47.

[1.79] J. P. Boeuf: J. Phys. D **36** (2003) R53.

[1.80] I. Radu, R. Bartnikas, G. Czeremuszkin, and M. R. Wertheimer: IEEE Trans. Plasma. Sci. **31** (2003) 411.

[1.81] S. Okazaki, M. Kogoma, and H. Uchiyama: Proc. 3rd Int. Symp. High Pressure Low Temperature Plasma Chemistry, 1991, p. 101.

[1.82] F. Massines, N. Gherardi, N. Naude, and P. Segur: Eur. Phys. J. Appl. Phys. **47** (2009) 22805.

[1.83] Y. Hiraoka, K. Urabe, and O. Sakai: presented at DPS2011, 33rd Int. Symp. Dry Process,

2011.

[1.84] O. Sakai, K. Tachibana, K. Tatsugawa, K. Ohishi, and R. Inoue: Trans. Mater. Res. Soc. Jpn. **31** (2006) 453.

[1.85] M. Teschke, J. Kedzierski, E. G. Finantu-Dinu, D. Korzec, and J. Engemann: IEEE Trans. Plasma. Sci. **33** (2005) 310.

[1.86] J. Kedzierski, J. Engemann, M. Teschke, and D. Korzec: Solid State Phenom. **107** (2005) 119.

[1.87] X. P. Lu and M. Laroussi: J. Appl. Phys. **100** (2006) 063302.

[1.88] B. L. Sands, B. N. Ganguly, and K. Tachibana: Appl. Phys. Lett. **92** (2008) 151503.

[1.89] Y. Ito, K. Urabe, M. Kubo, and K. Tachibana: Proc. 18th Int. Symp. Plasma Chemistry, 2007, p. 173.

[1.90] K. Urabe, T. Morita, K. Tachibana, and B. N. Ganguly: J. Phys. D **43** (2010) 095201.

Chapter 2

Parallel-Plate Dielectric Barrier Discharge[†]

2.1 Introduction

In this chapter, a CO_2-laser heterodyne interferometry (CO_2-LHI) method was applied to the parallel-plate dielectric barrier discharge (DBD). Spatial distributions of electron density, which is one of the crucial plasma parameter, inside the small scale plasmas operated at high pressure, have been measured by the CO_2-LHI method with good spatial resolution of μm order. [2.1, 2] This interferometry method is a kind of refractive-index measurement detecting the laser beam's phase shift caused by a tested plasma source. [2.3] Therefore, in CO_2-LHI measurements, the excitation and scattering processes that are largely dependent on gas composition and density can be ignored, which are indispensable for other spectroscopic methods for example Stark broadening [2.4] and Thomson scattering [2.5] measurements.

Different from previous works on the CO_2-LHI method applied to the high-pressure plasmas generated by DC voltages, [2.1, 2] the DBD is a pulsed discharge whose duration is within a few μs. In this time scale, the CO_2-LHI measurement's result only includes the temporally-averaged information of electron density because of the insufficient response time of its phase-detecting system. To learn the temporal evolution of electron density in the DBD, we also used

a millimeter-wave (mm-wave) transmission method [2.6–9] that can measure the ns-order temporal evolution of electron density, even though its spatial resolution is limited by the diffraction limit of the mm-wave. For the investigation of discharge mechanisms in the parallel-plate DBD, using both spatially and temporally resolved measurement methods has been required. There are some reports about spatiotemporally resolved electron density measurements using discharge current and optical emission intensity [2.10] and a ns-order temporally-resolved CO_2-LHI method [2.11] for pulsed plasmas. In this experimental study, the instantaneous images of spatial electron-density distribution when the density peaks were measured using a combination measurement of CO_2-LHI and mm-wave transmission. These two methods could reveal both direct time and position information on spatiotemporal structures of electron density.

Applying this combination measurement to an atmospheric-pressure glow discharge (APGD), which is a DBD that uses helium (He) gas with small nitrogen (N_2) impurity and kHz-order AC applied voltage, [2.12] the formation mechanisms of electron-density distribution inside the APGD is analyzed in this study. The results of the combination measurement showed the spatial distribution of temporal-peak electron density in the following N_2 impurity ratio conditions: 0% (pure He), 0.25%, and 0.50%. In addition to the electron-density measurements, the spatiotemporal structures of He metastable atom density and optical emission spectra were also measured using laser absorption spectroscopy (LAS) and optical emission spectroscopy (OES) methods and the total ionization frequencies in each gas composition using were discussed from calculations of Boltzmann and rate equations with a simple zero-dimensional ionization model.

2.2 Parallel-Plate DBD in He Gas with N$_2$ Impurity

Figure 2.1 shows a schematic diagram of the parallel-plate DBD tested in this chapter. The *xyz*

axes explain the directions of the laser beams and the oscillating fields used in the spectroscopic

measurements. A parallel-plate DBD configuration for the APGD generation was installed in

a vacuum chamber to control the gas composition and pressure. The powered (upper side) and

grounded (lower side) stainless-steel electrodes were round, and their radii were 30 mm. To

avoid discharge ignition between the upper-side powered electrode and the chamber wall, the

powered electrode was covered by a fluorocarbon cap. The lower-side electrode was attached to

the chamber floor, and the outer surface of the chamber wall was connected to the ground. The

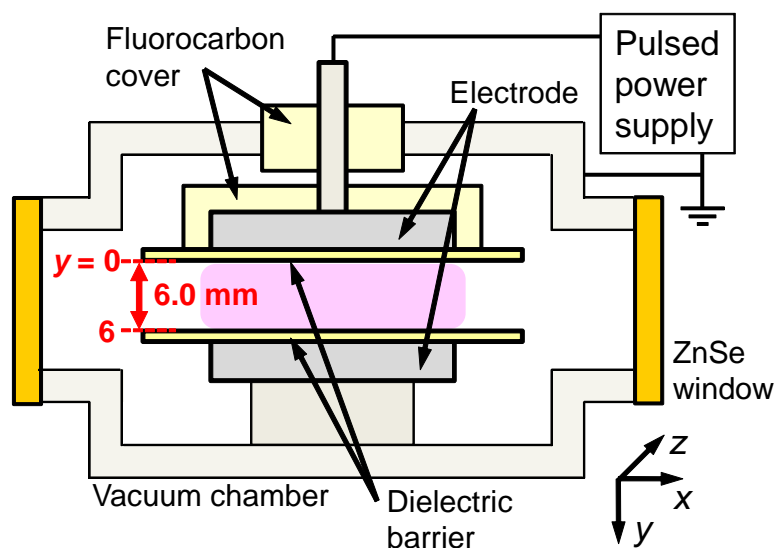dielectric barriers placed on the electrodes were made by 1-mm thick alumina and separated by

Figure 2.1 Experimental setup for parallel-plate DBD generation with *xyz* axes to explain directions of laser beams and oscillating fields in spectroscopic measurements. Origin of *y* axis is set at surface of dielectric barrier attached to upper-side powered electrode. Pair of ZnSe windows is only used in CO$_2$-LHI measurement to transmit far-infrared CO$_2$ laser beam, and quartz windows are used in other spectroscopic measurements.

6.0 mm by stacking small pieces of glass plate between the barriers to avoid interrupting the optical path for the spectroscopic measurements. To explain the measurement point, the origin of the *y* axis was set on the surface of the dielectric barrier placed on the powered electrode. The He gas flow was fed into the chamber as a main component of the gas mixture, and the flow rates of the He and N_2 gas were changed to control the N_2 impurity ratio at 0% (pure He), 0.25%, and 0.50%. The total gas flow rate and gas pressure inside the chamber were kept at 1.0 L/min and atmospheric pressure.

An AC high voltage including positive- and negative-main pulses (at 2.0 kV of peak voltage and 30 kHz of frequency) and large ringing components (smaller voltage oscillation than the main pulses) was applied between the two main pulses. Using such voltage waveform probably helped keep the homogeneous APGD in the relatively large discharge gap, because a glow-like discharge generation in the N_2 gas with a small discharge gap was observed only in larger
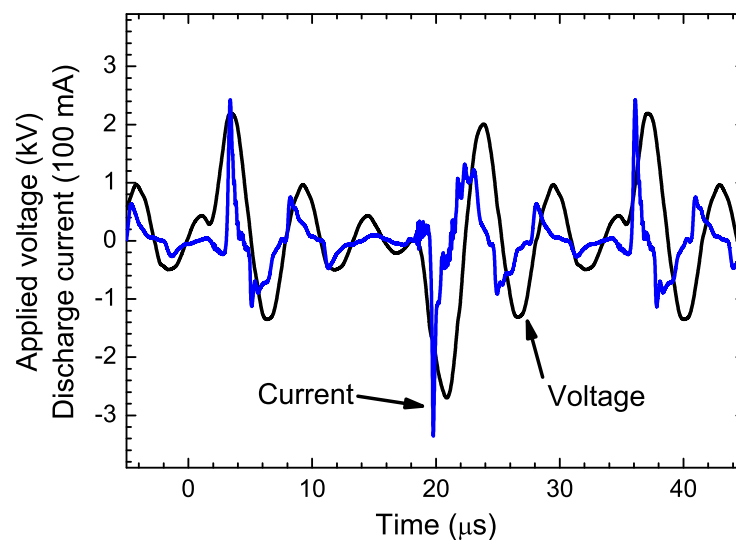

Figure 2.2   Example waveforms of applied voltage to upper-side powered electrode and discharge current flowing into grounded electrode and vacuum chamber.

amplitude of the ringing components. [2.13] The waveforms of the applied voltage to the upper-side powered electrode and the electric current flowing into the grounded electrode and the vacuum chamber were recorded by a high-voltage probe and a Rogowski coil connected to a digital oscilloscope. Figure 2.2 shows example waveforms of the applied voltage and the discharge current. The discharge-current waveform was derived by subtracting the displacement current, which was calculated from the differentiation of the applied-voltage waveform, from the original measured current waveform.

2.3   Spectroscopic Measurements

2.3.1 CO_2-laser heterodyne interferometry (CO_2-LHI)

A schematic diagram of the CO_2-LHI measurement is shown in Fig. 2.3. The original CO_2 laser beam at a wavelength of $10.6\,\mu$m was split into two paths, where the frequency in one path was shifted 40 MHz by an acousto-optical modulator (AOM), and in the other path the laser beam phase was shifted by the tested plasma. A pair of ZnSe windows on the chamber was used to transmit the CO_2 laser beam (see Fig. 2.1). These two laser beams were merged again, and their beat signal at 40 MHz was detected by a HgCdTe IR detector. The output signal of IR detector $I_{IR}(t)$ becomes

$$I_{IR}(t) = E_{P1}^2 + E_{P2}^2 + E_{P1}E_{P2}\cos(\Delta\omega_{AOM}t - \Delta\Phi) \qquad (2.1)$$

where E_{P1} and E_{P2} are the magnitudes of electric field in the laser beam passing through the AOM and the APGD, $\Delta\omega_{AOM}$ is the modulation frequency of the AOM (40 MHz), and $\Delta\Phi$ is
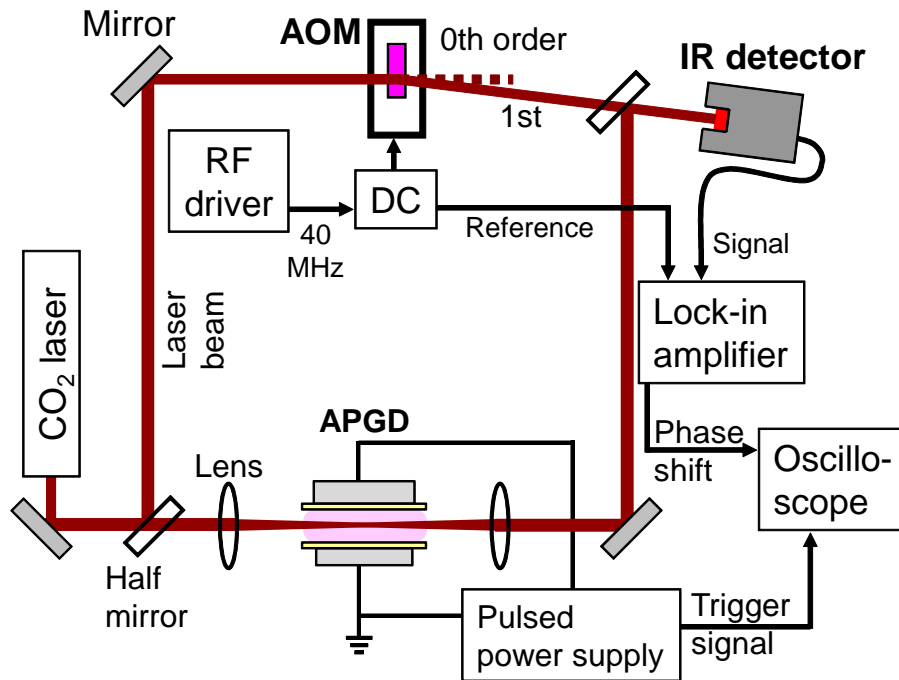
Figure 2.3   Schematic diagram of CO_2-LHI measurement. Component named "DC" indicates directional coupler used to input 40-MHz reference signal to lock-in amplifier.

the phase shift of the laser beam due to the presence of the APGD. From the output signal of

IR detector $I_{IR}(t)$ and the reference signal from AOM driver $\cos(\Delta\omega_{AOM}t)$, the phase shift by

APGD $\Delta\Phi$ was measured in a lock-in amplifier with a phase-shift resolution of 0.02°. The

temporal evolution of the phase-shift signal from the lock-in amplifier was recorded by the

digital oscilloscope.

A response time of the lock-in amplifier was was sufficiently longer (approximately 200

μs [2.2]) than the time scale of the temporal evolution of electron density inside the APGD.

Therefore, the output phase-shift signal of the lock-in amplifier only includes information of

the temporally-averaged electron density inside the APGD. Also, there is temporal variation of

the gas temperature associated with plasma generation, and this variation affects the refractive

index of plasma as well as the phase-shift signal measured in the lock-in amplifier. [2.14] To

divide the phase-shift signal into two components of the electron density and the gas temperature in a similar way used in the CO_2-LHI measurement for small-scale APPs driven by pulsed DC voltage, [2.1, 2] a square-pulse amplitude modulation at 125 Hz was applied to the 30-kHz applied voltage.

In the experiment, the CO_2 laser power fluctuated between 1.0 and 1.5 W in a time scale of ten minutes which was much longer than the characteristic times of discharges. The phase shift was also affected not only by the plasma generation but also by a small change of gas pressure along the laser path caused by wind or convections. These factors decreased the phase-shift resolution in the electron-density measurement. Therefore, we used the lock-in amplifier and the digital oscilloscope for the detection system. The lock-in amplifier eliminated the influence of the laser-power fluctuation and output the temporal evolution of the phase shift in the 40-MHz beat signal regardless of the CO_2 laser power. The phase shift variation, which was not associated with plasma generation, could be removed from the output signal of the lock-in amplifier using an AC coupling mode and the averages of 10,000 times in the digital oscilloscope synchronized with the 125-Hz modulation signal of the applied voltage, because the time constant of the phase shift variation by wind or convections was much longer than that by the plasma generation and these phenomena occurred randomly.

The 11 CO_2-LHI measurement points were scanned by 0.5 mm between the two dielectric barriers. The CO_2 laser beam was focused by a pair of ZnSe lenses with a focal length of 20 cm. Figure 2.4 shows a profile of the CO_2 laser beam radius after passing through the lens. [2.15] The center position of the APGD electrode was set at the CO_2-laser beam waist, and the spot radii near the outer edge and center of the APGD were 0.60 and 0.55 mm, respectively. The overlap of each measurement spot was not considered in the calculation for the spatial electron-
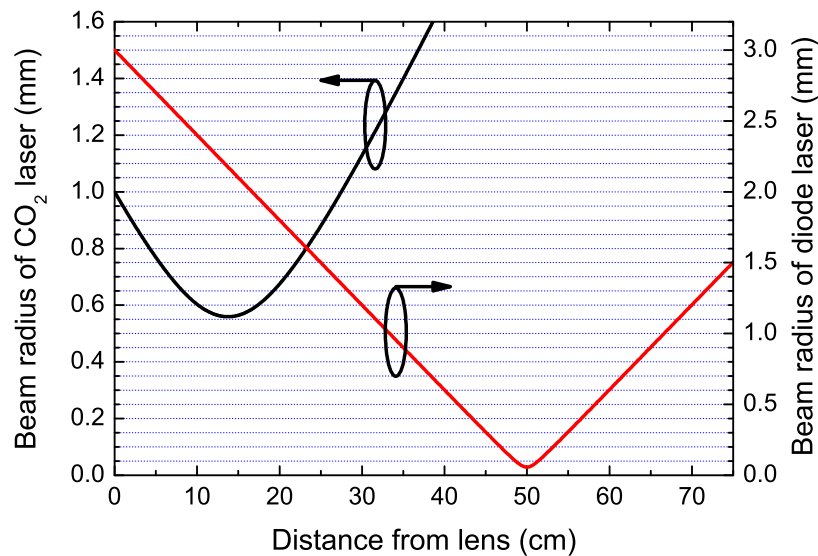
Figure 2.4   Beam spot radii of CO_2 laser beam at 10.6 μm and diode laser beam at 1083 nm as a function of distance from lens. Initial beam spot radii (1.0 mm for CO_2 laser and 3.0 mm for diode laser) and focal lengths of lens (20 cm for CO_2 laser and 50 cm for diode laser) correspond to real conditions used in CO_2-LHI and LAS measurements.

density distribution.

2.3.2   Millimeter-wave (mm-wave) transmission

The temporal evolutions of the electron density inside the APGD were measured using the mm-wave transmission method. Figure 2.5 shows a schematic diagram of the measurement method. For mm-wave generation at a frequency of 55 GHz, a swept signal generator, whose output frequency was up-converted by a mm-wave source module, was used as in our previous studies. [2.6–9] Pyramidal horn antennas were used as a transceiver and a receiver, and the received mm-wave intensity was observed by a Schottky-barrier-diode. The oscillation directions of the electric and magnetic fields in the mm-wave were aligned along the *y* and *z* axes, respectively. A pair of quartz windows on the vacuum chamber was equipped to transmit the
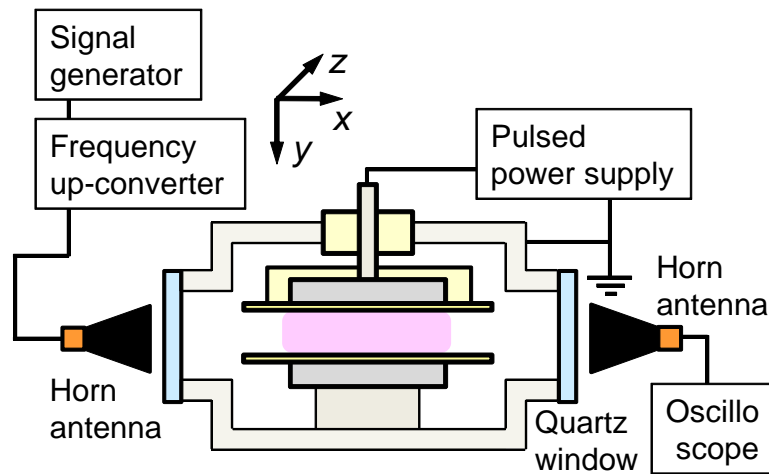
Figure 2.5   Schematic diagram of mm-wave transmission measurement. Mm-wave at a frequency of 55 GHz transmitted through vacuum chamber and APGD from left-hand side to right-hand side. Oscillation directions of electric and magnetic fields of mm-wave are aligned along y and z axes, respectively.

mm-wave in this measurement.

The spatial distribution of the mm-wave's electric field between the two electrodes can be described by an analogy of TEM mode in a parallel-plate waveguide for microwaves, because the wavelength of mm-wave and the gap length between two electrodes are in the same order. In this propagation mode, the electric field does not have any inhomogeneous property perpendicular to the parallel plate (along the y axis), regardless of the relationship between the mm-wave wavelength and the gap length. The plane wave propagates through the electrode configuration without variation of its plane's shape when the plasma is spatially homogeneous along the y axis. [2.16] If the spatial distribution of electron density between two dielectric barriers is inhomogeneous along the y axis, considering the distortion of the mm-wave plane (constant phase surface) by the generated plasma is indispensable for the calculation of the electron density. Two-type distortions of the mm-wave plane can be distinguished, focusing and defocusing effects, as reported by Bachynski and Graf. [2.17] The focusing effect of the mm-wave plane

can be seen when the electron density near the electrodes is larger than that in the middle of discharge gap. On the other hand, the mm-wave plane has a convex shape emerging from the plasma (defocusing effect) when the density in the middle is larger than that near the electrodes.

The absolute values of electron density were derived from the mm-wave's transmittance $|E_T/E_0|^2$, using the following equations and assuming the length of plasma l_{plasma} at 60 mm [2.9, 17]

$$\left|\frac{E_T}{E_0}\right|^2 = \left|\cosh\left\{(\alpha_{EM} - j\beta_{EM})l_{plasma}\right\} + (Z_r - jZ_i)\sinh\left\{(\alpha_{EM} + j\beta_{EM})l_{plasma}\right\}\right|^{-2} \tag{2.2}$$

with

$$Z_r = \frac{1}{2}\left(\frac{\beta_{EM}}{k_0}\right)\frac{|\varepsilon_{plasma}| + 1}{|\varepsilon_{plasma}|}, \quad Z_i = \frac{1}{2}\left(\frac{\alpha_{EM}}{k_0}\right)\frac{|\varepsilon_{plasma}| - 1}{|\varepsilon_{plasma}|}$$

where E_0 and E_T are the electric-field strengths of the incident and transmitted mm-waves, α_{EM} and β_{EM} are the imaginary and real parts of wavenumber vector k_{plasma}, ε_{plasma} is the complex permittivity of plasma, ω_{EM} is the angular frequency of the incident mm-wave, c is the light speed, ω_{pe} is the electron plasma frequency, and ν_m is the momentum transfer collision frequency. This equation includes influence of a multiple reflection effect at the boundary of the plasma. The collision frequency ν_m was parametrically changed by mean thermal velocity u_e (cm/s) given by electron temperature T_e as $\nu_m = 5.6\times10^{-16}u_e n_0$, where n_0 (cm^{-3}) is the number density of the ground state He atoms. [2.18] In this study, considering previous reported results inside He DBD at atmospheric pressure, electron temperature T_e was set at 0.5 eV. [2.6, 19] Finally, the electron density n_e was derived from electron plasma frequency $\omega_{pe} = \sqrt{n_e e^2/\varepsilon_0 m_e}$, which is a term in ε_{plasma}. Please refer section 1.2 for more detailed descriptions of α_{EM}, β_{EM}, and ε_{plasma}.

2.3.3 Laser absorption spectroscopy (LAS)

The LAS method was used to measure the spatiotemporal structures of He metastable 2^3S_1 (He^m) densities inside the APGD and to discuss the formation mechanisms of electron-density distribution and the influence of Penning ionization process by a collision between He^m atoms and N_2 neutral molecules. A diode laser beam entered into the APGD at a wavelength of 1083 nm was absorbed in 2^3S_1-2^3P_J ($J = 0,1,2$), and the transmitted laser-beam intensity was dected by a p-i-n photodiode with a response time of around 50 ns. The 11 LAS measurement points were identical to the CO_2-LHI measurement, and a pair of quartz windows were equipped to transmit the diode laser beam. A spot radius of the diode laser beam around the APGD was approximately 0.2 mm (see Fig. 2.4). A focal length of focusing quartz lens was 50 cm and the center position of the APGD electrode was set at the diode-laser beam waist.

Absolute He^m density was derived from the transmittance of laser beam I_T/I_0 with the following equation [2.8, 20]

$$n_{\mathrm{He^m}} = \frac{-\ln(I_T/I_0)}{l_{\mathrm{plasma}}} \frac{A_{\mathrm{LAS}}}{H_{\mathrm{LAS}}} \frac{\Delta \nu_D}{2} \sqrt{\frac{\pi}{\ln 2}} \frac{8\pi}{\lambda^2} \frac{g_1}{g_2} \tau \qquad (2.3)$$

where I_T and I_0 are the transmitted and incident laser beam intensities, A_{LAS} is the ratio of the absorption coefficient absorbed by the 2^3S_1-2^3P_2 transition to that measured at the peak wavelength of the transition, H_{LAS} is the ratio of the peak height of the measured line profile to that of the hypothetical single Doppler profile that has the same integrated area as the measured one, $\Delta \nu_D$ is the full width of half maximum (FWHM) of the Doppler broadening, λ is the laser beam wavelength, g_1 and g_2 are the statistical weights of the lower and upper levels of the

transition, and τ is the radiative lifetime. In this measurement, the absorbance of the diode laser beam corresponded to the line-integrated He^m density along the laser path, including the He^m atoms diffused from the electrode configuration in the chamber. The absolute He^m density was calculated under the assumptions that plasma length l_{LAS} was 60 mm (the diffused He^m atoms from the discharge gap are negligible) and the gas composition was pure He gas at atmospheric pressure. Note that the N_2 impurity ratio in the calculation of absolute He^m density makes little difference within such a small range of the N_2 impurity ratio used in this study. [2.20]

2.3.4 Optical emission spectroscopy (OES)

The OES method was performed to compare the emission spectra from the APGD in a wavelength range from 300 to 800 nm in each gas composition. The APGD emission was inserted into an optical fiber placed outside the chamber through a quartz window. The spectrometer, which was connected to the optical fiber, had a focal length of 5 cm and recorded the spectra by a 2048-pixel CCD linear array inside its package. The recorded spectra in this measurement were spatially averaged, because the numerical aperture of the optical fiber and the distance between the fiber tip and APGD were 0.22 and around 15 cm. Calculated from the numerical aperture and the distance, the detection spot radius became 3.8 cm near the APGD, which was much larger than the discharge gap. The spectra were also temporally averaged by the 1.0-s shutter speed of the CCD array in the spectrometer, which was much longer than the time scale of the APGD generation.

2.4 Density Distributions of Electrons and Excited Species

2.4.1 Spatial distribution of temporally-averaged electron density

Figure 2.6 shows the temporal evolutions of the CO_2 laser beam's phase shift due to the APGD generation measured by the CO_2-LHI method and the waveform of the 125-Hz modulation signal (Fig. 2.6(c)) of the applied voltage. The measurement positions were the nearest point to the dielectric barrier (Fig. 2.6(a), $y = 0.5$ mm) and near the middle of discharge gap (Fig. 2.6(b), $y = 2.5$ mm). The phase shift was divided into two components associated with the variations of electron density and gas temperature, using the time constant differences of these two phenomena, as explained in previous reports. [2.1, 2] In this experiment, the phase-shift signal at the start-up timing of the applied voltage (around -3.5 ms in Fig. 2.6) was unsuitable for the derivation of the electron density component in the signal. In this timing, the signal associated with the electron-density component was smoothed by the step-wise increase with the intermittent discharge in the APGD, and the influence of the smoothing effect on the signal could not be resolved. Therefore, the measured phase-shift waveform was divided into two components in the cut-off timing of the applied voltage (around 0 ms in time axis of Fig. 2.6). The electron-density component was derived by subtracting the gas-temperature component with a slower time constant from the measured waveform, fitting the slow time-constant component using the exponential curve, as shown in Fig. 2.6(a). From the measured results at each measurement point, the electron-density component was only observed near the dielectric barrier and could not be resolved around the middle of the discharge gap (Fig. 2.6(b)).

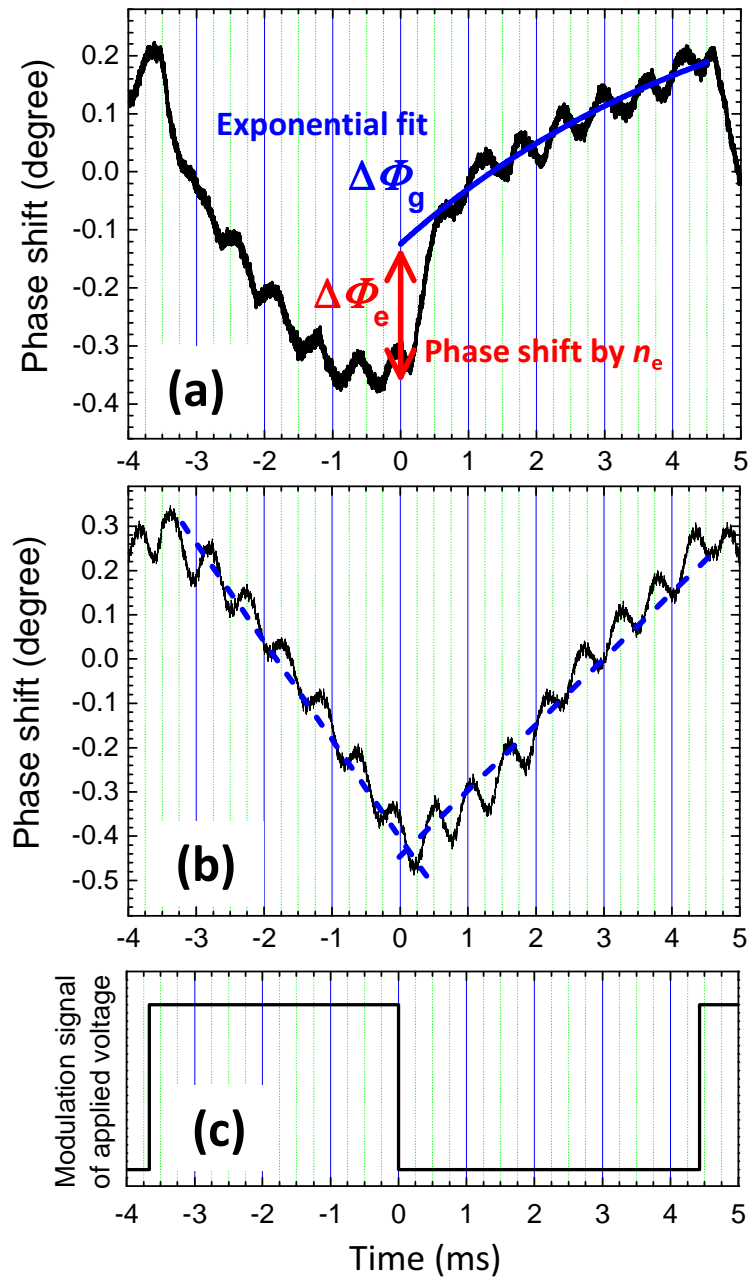After deriving the amplitude of the electron-density component in the phase shift in each gas

Figure 2.6 Waveforms of phase-shift signal measured by CO_2-LHI method at $y =$ (a) 0.5 and (b) 2.5 mm from dielectric barrier, together with (c) 125-Hz modulation signal of applied voltage. N_2 impurity ratio is 0.50%.

composition and measurement point, the temporally-averaged electron density was calculated as follows [2.3]

$$\Delta\Phi_e = \frac{2\pi}{\lambda} \int \Delta\left(N_{plasma} - 1\right)_e (x)dx = -\frac{e^2\lambda}{4c^2 m_e \varepsilon_0 \pi} \int n_e(x)dx = -\frac{e^2\lambda}{4c^2 m_e \varepsilon_0 \pi} n_e l_{plasma} \quad (2.4)$$

where $\Delta\Phi_e$ is the electron-density component in the phase shift, N_{plasma} is the refractive index of plasma, $\Delta\left(N_{plasma} - 1\right)_e$ is the difference of $(N_{plasma} - 1)$ caused by the change of the electron density, and $n_e(x)$ is the electron-density distribution along the laser path (x axis). The calculation in this study was with an assumption of homogeneous electron-density distribution along the x axis, and the plasma length along laser path l_{plasma} is 60 mm, as shown on the right hand side of Eq. (2.4) as $n_e l_{plasma}$.

The spatial distribution of the electron-density component in the phase shift and the calculated
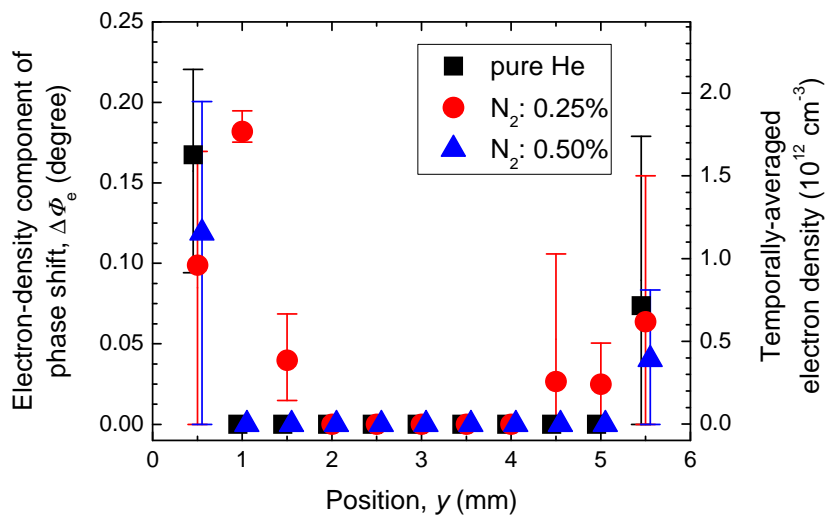

Figure 2.7 Spatial distributions of electron-density component in phase shift and temporally-averaged electron density in each gas composition derived from CO_2-LHI measurement results.

temporally-averaged electron density from the four signal waveforms measured under the same condition were plotted in Fig. 2.7. The points and both ends of the error bars indicate the averaged value and the maximum and minimum values in each measurement. The electron-density distributions inside the APGD were localized near the dielectric barriers in each gas composition, and small electron density could be observed at 1.5 mm from the barriers only in the 0.25% condition of the N_2 impurity ratio. In the following section, the reasons for this localized distribution and the influence of N_2 impurity on the distribution are discussed. The electron density near the powered electrode was approximately two times larger than that near the grounded electrode in each gas composition. This asymmetric distribution was probably caused by the diffusion of the discharge path to the chamber wall, not only by the flowing into the grounded electrode from the powered electrode.

2.4.2 Temporal evolution of spatially-averaged electron density

Based on the electron-density distribution measured by the CO_2-LHI method, the propagation characteristics of mm-wave inside the APGD are discussed again. Because the spatial distribution of the temporally-averaged electron density had a concave shape in each gas composition (Fig. 2.7), the mm-wave plane was affected by the focusing effect, as explained in subsection 2.3.2. However, the mm-wave's beam spot cannot be focused theoretically near its wavelength (due to the diffraction limit), and the wavelength (5.45 mm) and the gap length of the discharge region (6.0 mm) were similar in this experimental condition. Therefore, the mm-wave propagates in the APGD with little distortion of the mm-wave plane by the plasma, and it is confirmed that the mm-wave transmission method measured the spatially-averaged electron density between the two dielectric barriers in each gas composition. If the spatial distribution
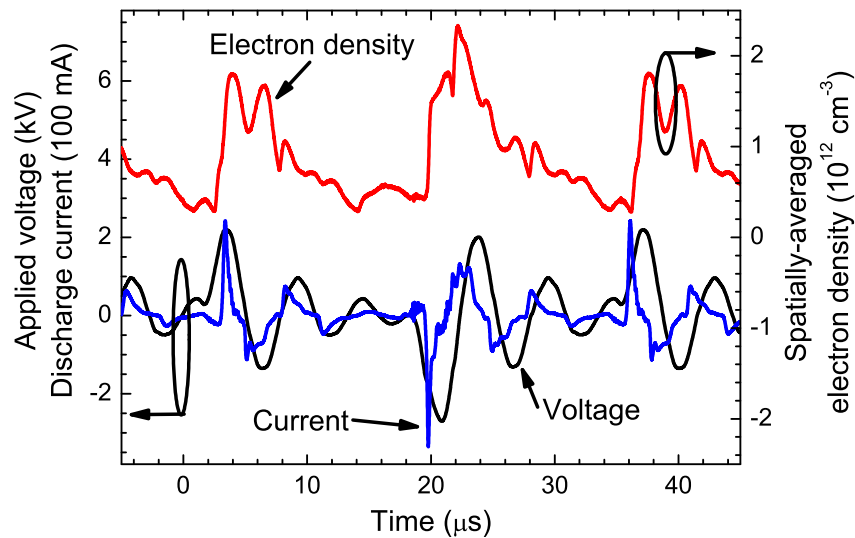
Figure 2.8   Temporal evolution of spatially-averaged electron density measured by mm-wave transmission method with waveforms of applied voltage and discharge current flowing into grounded electrode and vacuum chamber. N_2 impurity ratio is 0.50%.

of the electron density had been convex (center-peaked distribution), the decrease of the detected mm-wave intensity in the horn antenna caused by the defocusing effect should have been considered.

From the temporal evolution of the transmitted signal intensity in the mm-wave transmission measurement in each gas composition, the temporal evolution of the spatially-averaged electron density inside the APGD was calculated, following the procedure explained in subsection 2.3.2. The calculated temporal evolution of the electron density at the 0.50% condition of N_2 impurity ratio is shown in Fig. 2.8; the waveforms of the applied voltage and the discharge current flowing into the grounded electrode and the vacuum chamber. The electron density increased after the positive- and negative-main pulses around 2.6 and 19.0 μs in the abscissa axis of Fig. 2.8, and there were short increments after the main pulses, caused by the discharge currents flowing in the ringing part of the applied voltage.

For comparison of the decay processes of the electron density in each gas composition, the ratio of the temporally-averaged electron density to the temporal-peak electron density was calculated and it was named as a "duty ratio of plasma" D_{plasma} with the following equation

$$D_{\text{plasma}} = \frac{\int_{\text{1cycle}} n_{\text{e}}(t)\mathrm{d}t}{n_{\text{e-peak}} \times T} \tag{2.5}$$

where $\int_{\text{1cycle}} \mathrm{d}t$ is the temporal integration over one period of the alternating voltage at 30 kHz, $n_{\text{e}}(t)$ is the temporal evolution of the electron density, $n_{\text{e-peak}}$ is the temporal-peak electron density, and T is the time period of one applied-voltage cycle.

Table 2.1 lists the temporal-peak, the temporally-averaged electron density, and the duty ratio of plasma, derived from the measurement results in each gas composition. The duty ratio of plasma decreases with the increase of the N_2 impurity ratio, and this phenomenon is mainly caused by the increase of the quenching effects on the drifting electrons because of the larger inelastic-collision cross sections of the N_2 excitation than He. The largest electron density was

Table 2.1 Spatially-averaged data of temporal-peak electron density (n_{e}), temporally-averaged n_{e}, and duty ratio of plasma (D_{plasma}) measured by mm-wave transmission method in each gas composition.

Gas mixture	Temporal-peak n_{e} (cm^{-3})	Temporally-averaged n_{e} (cm^{-3})	Duty ratio of plasma D_{plasma}
Pure He	3.22×10^{12}	1.10×10^{12}	0.343
N_2: 0.25%	3.36×10^{12}	1.11×10^{12}	0.332
N_2: 0.50%	2.32×10^{12}	0.70×10^{12}	0.302

observed in the 0.25% condition of the N_2 impurity ratio. This result has a good agreement with the results of the CO_2-LHI measurement shown in subsection 2.4.1, since the result of the mm-wave transmission measurement indicates the total number of electrons along the mm-wave propagation direction and the broad electron-density distribution in the 0.25% condition of N_2 impurity ratio leads to a larger output value of the spatially-averaged electron density in the measurement.

The results of the mm-wave transmission measurement might suggest that the differences of the spatially-averaged electron density and the duty ratio of plasma, which depend on the N_2 impurity ratio, are too small for discussing the difference of the ionization processes, since the 0.25% and 0.5% of the N_2 impurity ratio are both much less than the He gas. However, I believe that the measurement results shown in this subsection correctly indicate the difference of the discharge phenomena, because our group, [2.8] Zhang and Kortshagen, [2.21] and Martens *et al.* [2.22, 23] have already reported that N_2 impurity not only in the % order but also in the ppm order significantly influences the discharge characteristics. The difference of the discharge phenomena in the very small range of the N_2 impurity ratio is due to the differences of the inelastic collision cross sections and the energy state structure between the He atoms and the N_2 molecules. The excitation and ionization energies of the N_2 molecules are also lower than those of the He atoms and rotational and vibrational relaxations of the electrons occur in N_2 plasma. Therefore, even in the ppm-order impurity ratio of the molecules put into the rare gas, the excitation, ionization, and energy relaxation processes of the electrons in plasma can be changed drastically from the pure rare gas plasma. Also, especially in the mixture of the He and N_2 gases, Penning ionization by the collision between the He^m atoms and the N_2 neutral molecules often becomes the dominant ionization process because the transition energy from

N_2 ($X^1\Sigma_g^+$) to N_2^+ ($B^2\Sigma_u^+$) at 18.9 eV is slightly smaller than the potential energy of the He^m

atoms at 19.8 eV.

2.4.3 Spatiotemporal structure of He metastable (He^m) density

Figure 2.9 shows the temporal evolutions of He^m density measured near both dielectric barriers

(at $y = 0.5$ mm and 5.5 mm) derived from the LAS measurement results and the applied-voltage

waveform. Vertical orange (2.6 μs) and green (19.0 μs) dashed lines indicate the measure-

ment timings of the spatial He^m-density distribution in the positive- and negative-main pulses

(Fig. 2.10). The He^m density near the powered and grounded electrodes increased when the

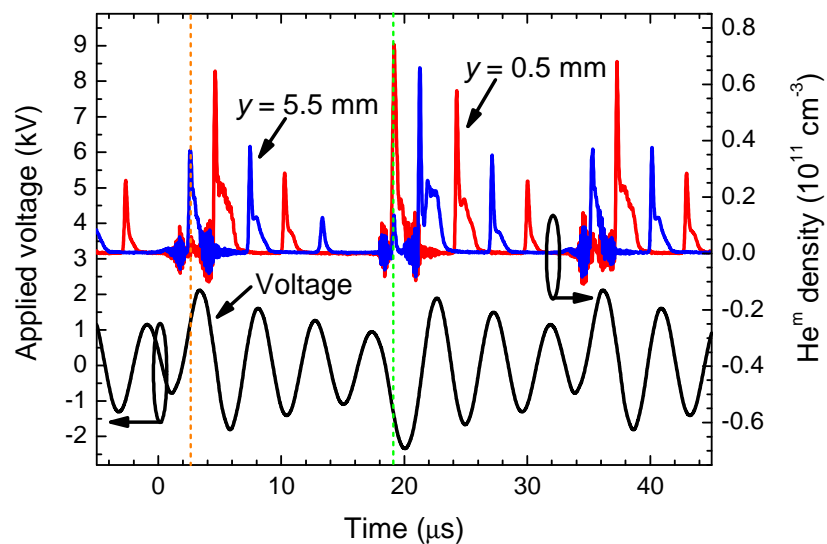electrodes became a temporal cathode and peaked alternatively in accordance with the applied-

Figure 2.9 Temporal evolutions of He^m density measured by LAS method in vicinity of
dielectric barriers ($y = 0.5$ mm and 5.5 mm) with applied-voltage waveform. N_2 impurity
ratio is 0.50%. Vertical orange (2.6 μs) and green (19.0 μs) dashed lines indicate measure-
ment timings of temporal-peak He^m density at positive- and negative-main pulses (Fig. 2.10),
respectively.

voltage polarity.

In order to observe the spatial distribution of He^m density when the powered electrode works as a temporal cathode and anode, its spatial distributions in each gas composition at the timings of the positive- and negative-main pulses are plotted in Fig. 2.10. The measurement timings were 2.6 μs (positive-main pulse, Fig. 2.10(a)) and 19.2 μs (negative-main pulse, Fig. 2.10(b)) in the time axis of Fig. 2.9. The He^m density was localized near the electrode working as the temporal cathode, and the peak value of He^m density decreases with the increase of the N$_2$ impurity ratio. A local minimum of He^m density could be observed at 1.5 mm from the dielectric barrier, and there was a plateau near the middle of the discharge gap in each gas composition. This result can be explained by the formation of a typical structure of a glow-like discharge that is composed of a negative glow region, a Faraday dark space, and a positive column.

From the LAS measurement results, it was difficult to distinguish the cathode fall region near the temporal cathode. Because of the spatial resolution of this measurement at 0.5 mm, the cathode fall region should be localized below 0.5 mm on the surface of the temporal cathode. This interpretation has good agreement with the measurement results of the electric field distributions in the He DBD reported by Obaradovic and Ivkovic *et al.* [2.24, 25] Their measurement results of electric field distribution at a pressure of 80 kPa using a line ratio method of He emission suggested that the length of the cathode fall region was around 1.2 mm at the ignition timing of the discharge and decreased toward 0.6 mm at 300 ns after ignition. Considering the pressure difference between their and our experimental conditions, the length of the cathode fall region in our experiments probably fell below 0.5 mm after the ignition.

Figure 2.11 shows the temporal evolutions of normalized He^m density measured in the negative-main pulse at $y = 0.5$ mm in each gas composition. The fluctuation of the signal
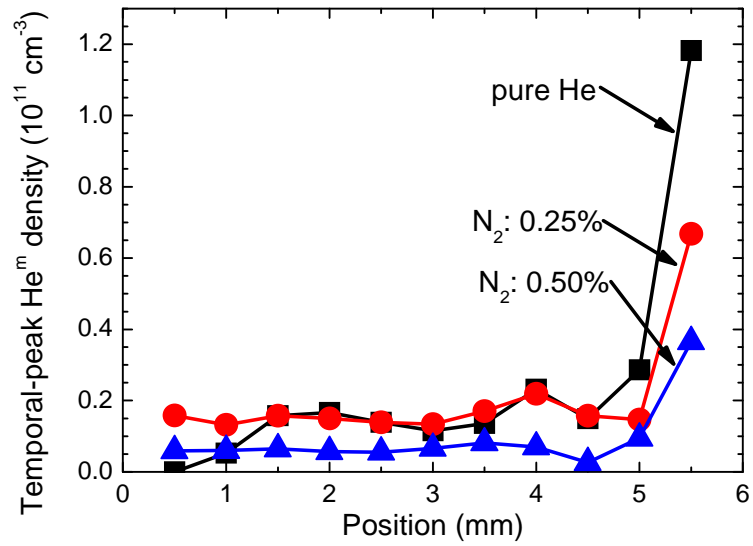
(a)
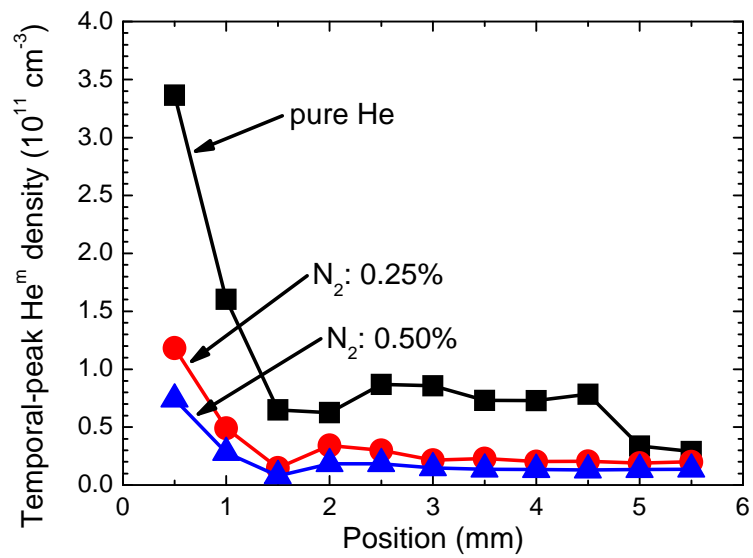
(b)

Figure 2.10   Spatial distributions of He^m density measured by LAS method in each gas composition at timings: (a) positive- (2.6 μs in time axis in Fig. 2.9) and (b) negative-main (19.0 μs) pulses.
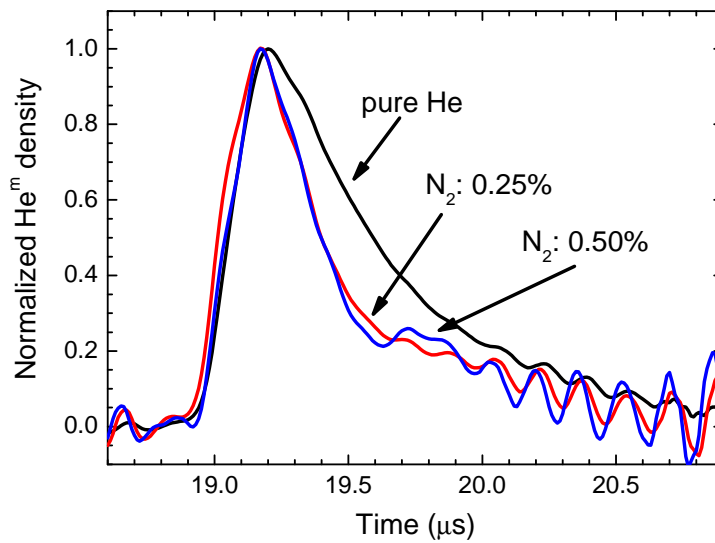
Figure 2.11   Temporal evolutions of normalized He^m density measured by LAS method in each gas composition at $y = 0.5$ mm. Horizontal time axis is identical to that in Fig. 2.9.

measured in the 0.25% and 0.50% conditions of the N_2 impurity ratio is the oscillation of the measurement system enlarged by the normalization to have the same peak value as the signal measured at 0% (pure He). Comparing the results in pure He and at 0.25%, the decay time constant at 0.25% is smaller than that in pure He. This result indicates that putting N_2 impurity in the He gas accelerates the quench speed of He^m atoms by Penning ionization between the He^m atoms and the N_2 neutral molecules.

2.4.4   Optical emission spectrum

Both the temporally- and spatially-averaged emission spectra of the APGD in each gas composition are shown in Fig. 2.12. The peak emission intensity of He I (3^3S-2^3P) at 707 nm gradually decreased, and strong emissions of the N_2 second positive system ($C^3\Pi_u$-$B^3\Pi_g$) and
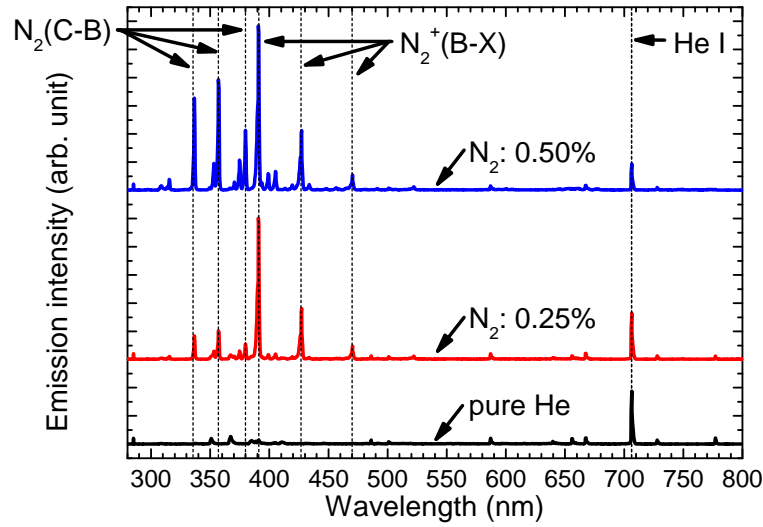
Figure 2.12   Temporally- and spatially-averaged emission spectra of APGD measured by OES method in each gas composition.

the N_2^+ first negative system ($B^2\Sigma_u^+$-$X^2\Sigma_g^+$) bands were observed when N_2 impurity was added. Comparing the spectra between the 0.25% and 0.50% conditions of the N_2 impurity ratio, the ratio of N_2^+ (B-X) emission intensity to N_2 (C-B) is much larger at 0.25% than at 0.50%. This larger emission-intensity ratio of the N_2 (C-B) to N_2^+ (B-X) suggests lower reduced electric field in the 0.50% condition of N_2 impurity ratio than that in 0.25% when we assume only electron impact ionization processes in the APGD. However, in high-pressure discharge using the He and N_2 gas mixture, note that the Penning ionization processes by the collision between He^m atoms and N_2 neutral molecules also affect the emission-intensity ratio of N_2 (C-B) to N_2^+ (B-X).

2.5 Comprehensive Discussion on Spatiotemporal Distribution of Electron Density

From the measurement results of the CO_2-LHI and mm-wave transmission methods in each gas composition, the spatial distribution of the temporal-peak electron density inside the APGD (Fig. 2.13) was calculated by dividing the temporally-averaged electron density (Fig. 2.7) by the duty ratio of plasma (table 2.1). The peak density near the dielectric barriers was approximately 5×10^{12} cm^{-3} on the side of the powered electrode and 2×10^{12} cm^{-3} on the grounded electrode. The peak electron density near the middle of discharge gap, which was only observed in the 0.25% condition of the N_2 impurity ratio (measured between 0.5 and 1.5 mm from the dielectric barrier), was around 1×10^{12} cm^{-3}. The reason that the electron density can only be detected in
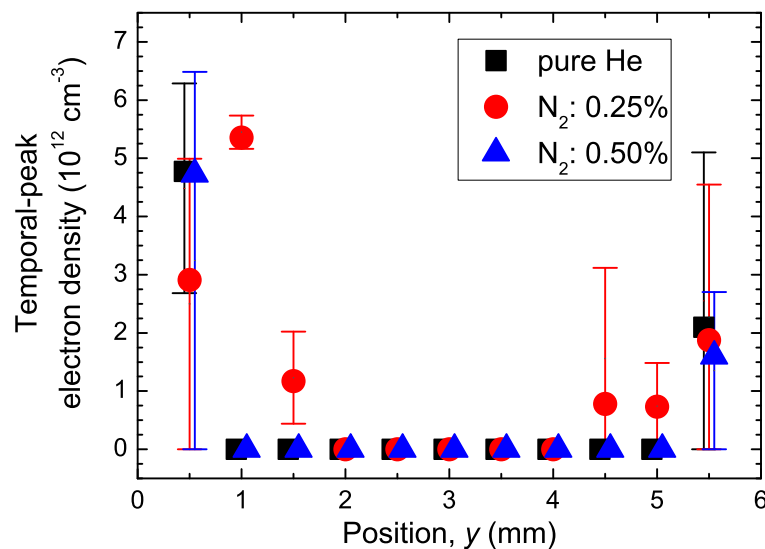

Figure 2.13 Spatial distribution of temporal-peak electron density calculated from temporally-averaged electron-density distribution and duty ratio of plasma in each gas composition.

the 0.25% condition will be discussed in the following subsection.

Considering the spatiotemporal structures of the He^m density measured by the LAS method, the excited-species density, including the electrons inside the APGD, was localized by the formation of a negative glow region near the temporal cathode. Therefore, the electron-density distribution (Fig. 2.13) still cannot depict the real instantaneous images of electron-density distribution, and the peak-density region is altered between the two dielectric barriers in accordance with the applied-voltage polarity. This difference of electron-density distribution from the real structure is due to using the spatial distribution of the temporally-averaged electron density for the calculation of the temporal-peak density and indicates the effectiveness of using additional spatiotemporally resolved measurements of excited species such as the LAS method or ICCD camera observation.
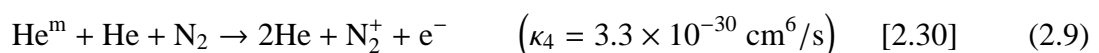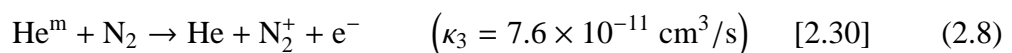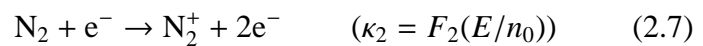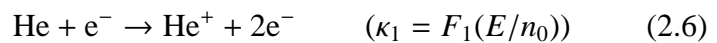
The measurement results of the spatial distribution of the temporal-peak electron density are compared with the simulated results reported by Massines *et al.* [2.26, 27] and Martens *et al.* [2.28] These simulations were calculated under a condition at a 5.0-mm length of discharge gap that resembles our experimental condition at 6.0 mm. The spatial distribution in the measurement results of the electron and He^m densities, which included a peak density at 0.5 mm from the dielectric barrier and the presence of a Faraday dark space from 1.0 to 2.0 mm, have good agreements with the calculated results reported by Massines *et al.* [2.26, 27] Martens *et al.* [2.28] They showed the temporal evolutions of electron-density distribution and suggested that the typical structure of the glow discharge was built after a Townsend discharge regime and that the structure in the transient glow discharge regime was not changed significantly in its increase phase. This result supports the assumption in the calculation of the temporal-peak electron density that the spatial distributions of electron density in each discharge pulse are not

changed from ignition to extinguishment.

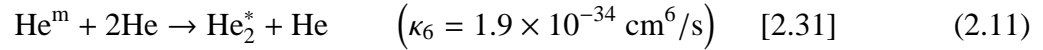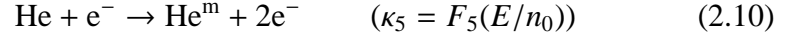## 2.6   Analysis on Influence of N_2 Impurity on Ionization Process

The experimental results of the mm-wave transmission and LAS measurements suggested that the Penning ionization between the He^m atoms and the N_2 neutral molecules has maximum influence on the discharge phenomena in the 0.25% condition of the N_2 impurity ratio. This interpretation is also supported by the OES measurement result, since the Penning ionization tends to make a N_2^+ (B) state ion [2.29] and relatively strong N_2 (C-B) emission was observed in the electron impact ionization. [2.20] However, discussing the ionization processes inside the APGD and analyzing the effect of N_2 impurity are difficult using only the experimental results.

For more detailed investigation of the effect of N_2 impurity on the ionization processes, a simple zero-dimensional model was built for the calculation of ionization frequencies in each gas composition. In this calculation, we assumed that the ionization processes in the APGD were dominated by the four reactions listed below

$$He + e^- \rightarrow He^+ + 2e^- \qquad (\kappa_1 = F_1(E/n_0)) \qquad (2.6)$$

$$N_2 + e^- \rightarrow N_2^+ + 2e^- \qquad (\kappa_2 = F_2(E/n_0)) \qquad (2.7)$$

$$He^m + N_2 \rightarrow He + N_2^+ + e^- \qquad \left(\kappa_3 = 7.6 \times 10^{-11} \text{ cm}^3/\text{s}\right) \quad [2.30] \qquad (2.8)$$

$$He^m + He + N_2 \rightarrow 2He + N_2^+ + e^- \qquad \left(\kappa_4 = 3.3 \times 10^{-30} \text{ cm}^6/\text{s}\right) \quad [2.30] \qquad (2.9)$$

where κ is the rate coefficient for the two- and three-body collision processes, the subscript numbers represent each reaction, $F(E/n_0)$ is the function of the reduced electric field. To derive

the ionization frequency of Penning ionization (Eq. (2.8)) and bimolecular Penning ionization (Eq. (2.9)), the generation and destruction processes for He^m atoms are included

$$He + e^- \rightarrow He^m + 2e^- \qquad (\kappa_5 = F_5(E/n_0)) \qquad (2.10)$$

$$He^m + 2He \rightarrow He_2^* + He \qquad \left(\kappa_6 = 1.9 \times 10^{-34} \text{ cm}^6/\text{s}\right) \quad [2.31] \qquad (2.11)$$

and a rate equation for He^m atoms was made

$$\frac{dn_{He^m}}{dt} = \kappa_5[He][e^-] - \left(\kappa_3[He^m][N_2] + \kappa_4[He^m][He][N_2] + \kappa_6[He^m][He]^2\right) \qquad (2.12)$$

where the brackets denote the number densities. In the static state of Eq. (2.12), $\dfrac{dn_{He^m}}{dt}$ becomes 0, and the source term of the electron by the Penning ionization processes can be written as $\kappa_5[He][e^-] \times \dfrac{\kappa_3[N_2] + \kappa_4[He][N_2]}{\kappa_3[N_2] + \kappa_4[He][N_2] + \kappa_6[He]^2}$. From this source term, the ionization frequency of the two Penning ionization processes $f_{Penning}$ was calculated by subtracting the electron density as in the following equation

$$f_{Penning} = \kappa_5[He] \times \frac{\kappa_3[N_2] + \kappa_4[He][N_2]}{\kappa_3[N_2] + \kappa_4[He][N_2] + \kappa_6[He]^2} \qquad (2.13)$$

Then total ionization frequency f_{total} was finally derived

$$f_{total} = \kappa_1[He] + \kappa_2[N_2] + f_{Penning}. \qquad (2.14)$$

In this calculation, the rate coefficients of the electron impact ionization and excitation processes (Eqs. (2.6), (2.7), and (2.10)) were calculated using a Boltzmann equation solver

(Bolsig+ [2.32]) as a function of the reduced electric field considering each gas composition. The rate coefficient of He^m-atom generation κ_5 was derived by adding all the rate coefficients of the excitation processes of He atoms, with an assumption that all the excited He atoms became the triplet metastable state after radiation and collision processes.

Figure 2.14 shows the calculation results of total ionization frequency f_{total} in Eq. (2.14) as a function of the reduced electric field. In the pure He condition, f_{total} was calculated considering only the electron impact ionization in Eq. (2.6). The ionization frequency was maximized in the 0.25% condition of the N_2 impurity ratio, and the frequency difference in each gas composition increased with decreasing the reduced electric field. In experimental conditions of this study (peak voltage: 2.0 kV, gap distance: 6.0 mm, and at atmospheric pressure), the peak reduced electric field was calculated at 12×10^{-17} V cm^2, without considering the formation of a glow-like discharge structure. In the practical condition, the reduced electric field near the middle
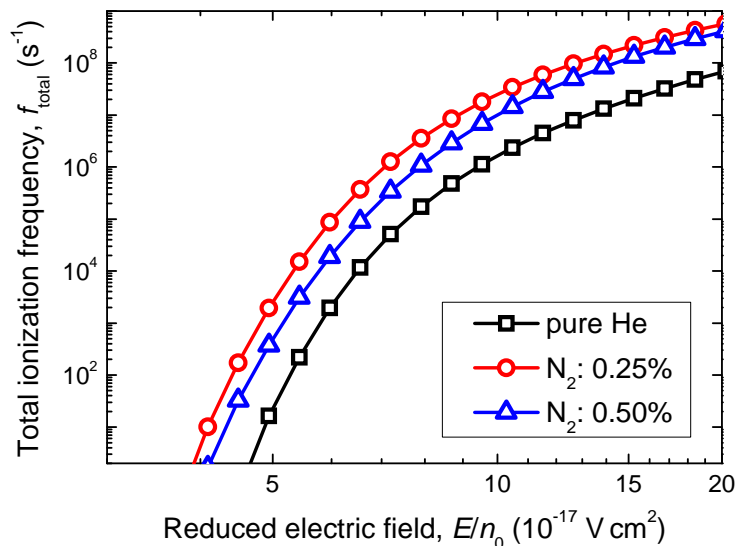

Figure 2.14   Calculation results of total ionization frequency f_{total} as a function of reduced electric field E/n_0 in each gas composition.

of the discharge gap is lower than the calculated value because of the high electric field in the cathode fall and negative glow region that formed near the temporal cathode. These results explain the largest peak electron density and the broad distribution measured only at the 0.25% condition of the N_2 impurity ratio.

In this calculation model, the influence of plasma-wall interaction which becomes an important factor for low-pressure plasmas was not considered, because the Penning ionization processes become dominant in the 0.25% condition of the N_2 impurity ratio as shown in Fig. 2.15. This figure shows the ionization frequencies associated with the electron impact ionizations and Penning ionizations. The He^m atoms cannot be moved by the electric field and the diffusion of He^m is negligible in the Faraday dark space and the positive column in the high-pressure discharge. Therefore, the plasma-wall interaction in the calculation model was not included only
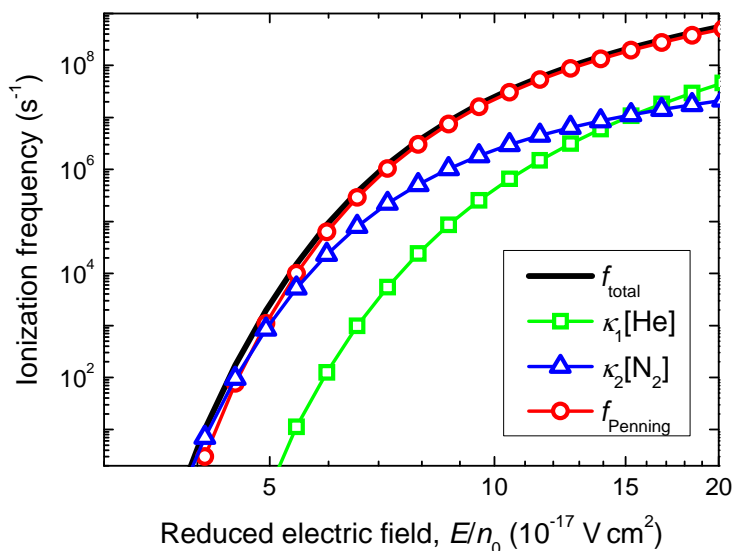

Figure 2.15 Calculation results of total ionization frequency f_{total} and ionization frequencies associated with electron impact ionizations of He atoms ($\kappa_1[He]$) and N_2 molecules ($\kappa_2[N_2]$) and two- and three-body Penning ionizations between He^m atoms and N_2 molecules ($f_{Penning}$) as a function of reduced electric field E/n_0 in 0.25% condition of N_2 impurity ratio.

for the discussion of the electron-density difference that is not in the vicinity of the temporal cathode. Of course, for the investigation of the negative glow and cathode fall regions in more detail using the numerical calculations, the plasma-wall interaction, the electronic-field structure near the cathode, and the drift and diffusion lengths of the electrons and the He^m atoms must be precisely evaluated.

2.7   Summary

In this chapter, the spatiotemporal structures of electron density inside the APGD using He gas with small N_2 impurity are introduced. The spatial distribution of electron density was measured by the CO_2-LHI method, which could not have temporal resolution below ms order. The temporal evolution of the spatially-averaged electron density was measured by the mm-wave transmission method. The spatial distribution of the temporal-peak electron density was derived using the combination measurement results. The temporal-peak electron density near the dielectric barrier approached the 5×10^{12} cm^{-3}, and the density 1.5 mm from the barrier, which was observed only in the 0.25% condition of the N_2 impurity ratio, was around 1×10^{12} cm^{-3}. LAS and OES measurements were also performed to support the electron-density measurements from the view point of the spatiotemporal structure of the excited species. The LAS measurement results indicated that the localization of the electron density was due to the formation of a negative glow region near the temporal cathode. Also, enhanced ionization in the 0.25% condition of the N_2 impurity ratio was confirmed from the numerical calculation of total ionization frequency using the zero-dimensional ionization model.

References

[2.1] F. Leipold, R. H. Stark, A. El-Habachi, and K. H. Schoenbach: J. Phys. D **33** (2000) 2268.

[2.2] J.-Y. Choi, N. Takano, K. Urabe, and K. Tachibana: Plasma Sources Sci. Technol. **18** (2009) 035023.

[2.3] I. H. Hutchinson: *Principles of Plasma Diagnostics* (Cambridge University Press, New York, 2002) 2nd ed.

[2.4] C. O. Laux, T. G. Spence, C. H. Kruger, and R. N. Zare: Plasma Sources Sci. Technol. **12** (2003) 125.

[2.5] A. Kono and K. Iwamoto: Jpn. J. Appl. Phys. **43** (2004) L1010.

[2.6] K. Tachibana, Y. Kishimoto, S. Kawai, T. Sakaguchi, and O. Sakai: Plasma Phys. Control. Fusion **47** (2005) A167.

[2.7] O. Sakai, T. Sakaguchi, Y. Ito, and K. Tachibana: Plasma Phys. Control. Fusion **47** (2005) B617.

[2.8] K. Tachibana, Y. Kishimoto, and O. Sakai: J. Appl. Phys. **97** (2005) 123301.

[2.9] Y. Ito, O. Sakai, and K. Tachibana: Plasma Sources Sci. Technol. **19** (2010) 025006.

[2.10] X. Lu, F. Leipold, and M. Laroussi: J. Phys. D **36** (2003) 2662.

[2.11] B. N. Ganguly, W. R. Lempert, K. Akhtar, J. E. Scharer, F. Leipold, C. O. Laux, R. N. Zare, and A. P. Yalin: in *Non-equilibrium air plasmas at atmospheric pressure*, eds. K. H. Becker, U. Kogelschats, K. H. Schoenbach, and R. J. Barker (IoP Publishing, Bristol, 2005).

[2.12] S. Kanazawa, M. Kogoma, T. Moriwaki, and S. Okazaki: J. Phys. D **21** (1988) 838.

[2.13] T. Somekawa, T. Shirafuji, O. Sakai, K. Tachibana, and K. Matsunaga: J. Phys. D **38** (2005) 1910.

[2.14] C. W. Allen: *Astrophysical Quantities* (The Athlone Press, London, 1973) 3rd ed.

[2.15] A. Yariv: *Optical Electronics in Modern Communications* (Oxford University Press, New York, 1997) 5th ed.

[2.16] D. M. Pozar: *Microwave Engineering* (Wiley, New York, 2005).

[2.17] M. P. Bachynski and K. A. Graf: RCA Rev. **25** (1964) 3.

[2.18] S. C. Brown: *Basic Data of Plasma Physics* (Wiley, New York, 1959).

[2.19] X. Lu and M. Laroussi: Appl. Phys. Lett. **92** (2008) 051501.

[2.20] K. Urabe, T. Morita, K. Tachibana, and B. N. Ganguly: J. Phys. D **43** (2010) 095201.

[2.21] P. Zhang and U. Kortshagen: J. Phys. D **39** (2006) 153.

[2.22] T. Martens, A. Bogaerts, W. J. M. Brok, and J. van Dijk: Appl. Phys. Lett. **92** (2008) 041504.

[2.23] T. Martens, A. Bogaerts, W. J. M. Brok, and J. van Dejk: Appl. Phys. Lett. **96** (2010) 091501.

[2.24] B. M. Obradovic, S. S. Ivkovic, and M. M. Kuraica: Appl. Phys. Lett. **92** (2008) 191501.

[2.25] S. S. Ivkovic, B. M. Obradovic, N. Cvetanovic, M. M. Kuraica, and J. Puric: J. Phys. D **42** (2009) 225206.

[2.26] F. Massines, A. Rabehi, P. Decomps, R. B. Gadri, P. Segur, and C. Mayoux: J. Appl. Phys. **83** (1998) 2950.

[2.27] F. Massines, P. Segur, N. Gherardi, C. Khamphan, and A. Ricard: Surf. Coating. Technol. **174-175** (2003) 8.

[2.28] T. Martens, W. J. M. Brok, J. van Dijk, and A. Bogaerts: J. Phys. D **42** (2009) 122002.

[2.29] I. Tokue, T. Kawai, and K. Yamasaki: Chem. Phys. Lett. **270** (1997) 587.

[2.30] J. M. Pouvesle, A. Bouchhoule, and J. Stevefelt: J. Chem. Phys. **77** (1982) 817.

[2.31] C. B. Collins and F. W. Lee: J. Chem. Phys. **70** (1979) 1275.

[2.32] G. J. M. Hagelaar and L. C. Pitchford: Plasma Sources Sci. Technol. **14** (2005) 722.

Chapter 3

Coaxial Dielectric Barrier Discharge Jet[†]

3.1 Introduction

Ignition mechanisms and plasma parameters in a plasma plume of the coaxial dielectric barrier discharge (DBD) jet are discussed in this chapter based on experimental results of spectroscopic measurements. Some recent studies have suggested from indirect estimations using their ICCD-camera observation results that the main discharge mechanisms in the coaxial DBD jet include an ionization-front propagation like a positive corona discharge in the plume in addition to the coaxial DBD inside the tube. [3.1, 2] However, there is no report on specific diagnostics of excited-species behaviors and plasma parameters in this coaxial DBD jet confirming these suggested mechanisms as yet because of the difficulty to measure those quantities in the plume, whose formation is a very spatiotemporally localized phenomenon.

For the purpose of confirming formation mechanisms of the plasma plume, relationships between two discharge phenomena in the coaxial DBD jet, which are the coaxial DBD inside the tube and the plume formation in open space, are investigated in this chapter. As a first step,

---

†This Chapter is altered form of two published papers: K. Urabe, Y. Ito, K. Tachibana, and B. N. Ganguly, "*Behavior of N_2^+ Ions in He Microplasma Jet at Atmospheric Pressure Measured by Laser Induced Fluorescence Spectroscopy*", Applied Physics Express, **1** (2008) 066004 and K. Urabe, Y. Ito, O. Sakai, and K. Tachibana, "*Interaction between Dielectric Barrier Discharge and Positive Streamer in Helium Plasma Jet at Atmospheric Pressure*", Japanese Journal of Applied Physics, **49** (2010) 106001.

plume-length dependence on electrode length was measured, and three types of novel electrode configurations composed of insulated electric wires, which could increase the plume length without increasing power consumption to the coaxial DBD, were demonstrated. The plume length, discharge currents in the coaxial DBD inside the tube, and line-integrated densities of helium metastable 2^3S_1 (He^m) atoms in the plume were measured to determine the discharge characteristics in each electrode configuration. The measurement results indicated that surface charges accumulated on inner surface of the tube owing to the coaxial DBD played an important role in the plume formation. In addition to these experimental studies, spatiotemporal structures of electrical potential was calculated by a two-dimensional (2D) axisymmetrical finite element method, including practical conditions of the applied voltage and the surface-charge density, to discuss the difference in plume length following the change of the electrode configuration.

Also, the discharge characteristics in the plasma plume are discussed from another view point of spatiotemporal behavior of nitrogen ions (N_2^+) in the ground state in the plasma plume. Since our preliminary experimental results showed a ns-order rapid decrease of the He^m density in the plume due to a Penning ionization process with N_2 molecules contaminating from ambient air, [3.3] the N_2^+ ions are expected to be the major ionic species in the plume. High resolution rotational spectra of the (0-0) band of first negative system ($B^2\Sigma_u^+$-$X^2\Sigma_g^+$) of N_2^+ ions in the plume could be obtained by a laser induced fluorescence spectroscopy (LIF) method.

3.2   Coaxial DBD Jet in He Gas Flown to Open Air

The experimental setup of the coaxial DBD jet is shown in Fig. 3.1, together with a schematic diagram of the laser absorption spectroscopy (LAS) measurement using similar procedure explained in section 2.3.3. [3.4] Experimental conditions used except for the LIF measurement
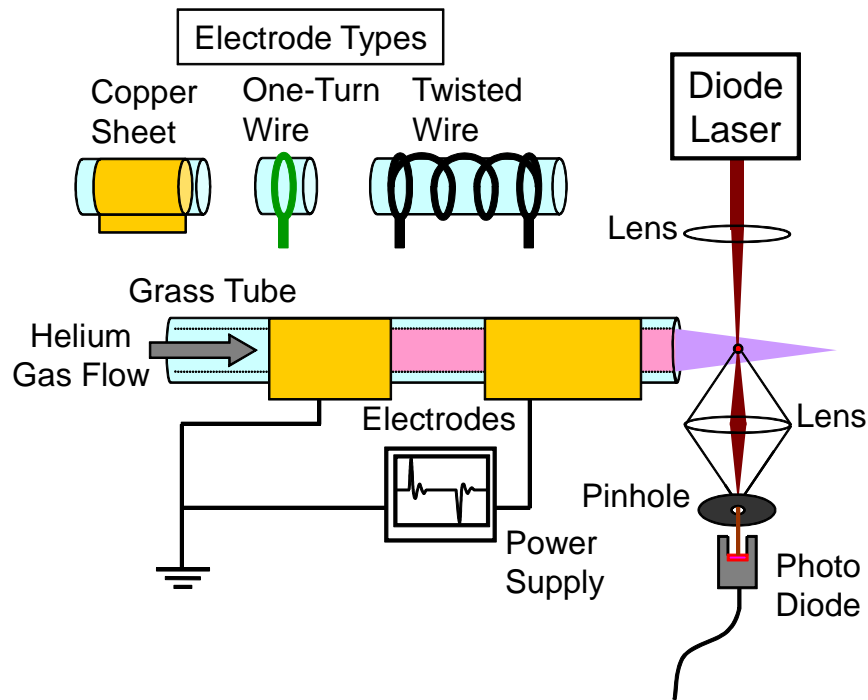
Figure 3.1   Schematic diagram of coaxial DBD jet and laser absorption spectroscopy (LAS) measurement, together with three types of electrode structure used in this chapter.

were a glass tube with a 4-mm bore and 2.8-L/min flow rate of He gas flow (corresponding flow speed was 3.7 m/s). Also, a bipolar impulse voltage [3.5] was applied at 5 kHz to ignite the plasma in the coaxial DBD jet, and the peak voltage was 8.0 kV. As front-side powered and back-side grounded electrodes, copper sheets and/or insulated electric wires were twisted around the glass tube with no spatial gap. The outer diameter of insulated wires was 0.56 mm and its dielectric was fluorocarbon polymer with a 0.15-mm thickness. Variation of the electrode configurations enables us to control discharge characteristics of the coaxial DBD inside the tube without any difference in the gas flow and the initial potential distribution in the plume region. A high-voltage probe and a Rogowski coil connected to a digital oscilloscope recorded the temporal evolutions of the applied voltage and the discharge current.

3.3   Laser Induced Fluorescence Spectroscopy (LIF) Measurement

The experimental setup for the LIF measurement, including the electrode configuration of the coaxial DBD jet, is shown in Fig. 3.2. Different from all other experiments, the glass tube had a 2-mm bore equipped with two copper ring electrodes of a 6-mm length at the grounded side and 20 mm at the powered side separated from each other by a distance of 30 mm, and a unipolar pulse voltage was applied at a frequency of 10 kHz with a peak voltage of 6.5 kV and its pulse width of 8 μs. The He gas was flown at 1.4 L/min to open space, which generated a laminar flow at a velocity of 7.4 m/s. The LIF method for the N_2^+ ions has been applied to
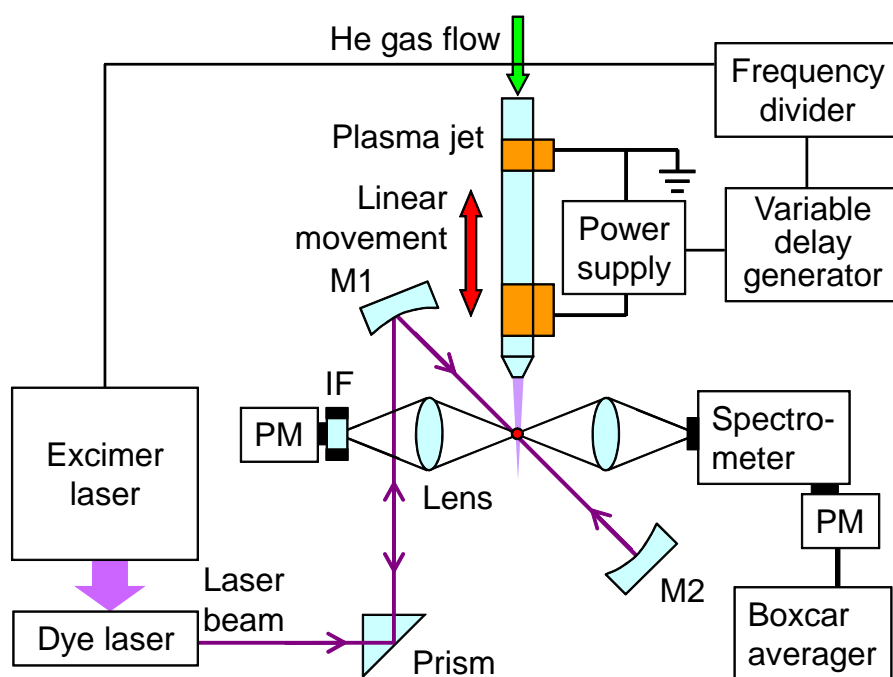
Figure 3.2   Schematic diagram of laser induced fluorescence (LIF) measurement. IF is interference bandpass filter transmitting around 430-nm light, and PM is photomultiplier tube detecting light intensity.

diagnose rotational temperatures [3.6] and absolute ion densities [3.7] in low-pressure plasmas. In this study, to achieve the temporally-resolved measurement for the high-speed discharge behaviors, a variable delay generator was connected to the power supply, and its output signal was downscaled to 10 Hz by a frequency divider and triggered the excimer laser synchronously with the applied voltage. For the purpose of Doppler spectroscopy, the output beam from a dye laser was aligned to cross the plasma plume two times (back and forth) at the focusing point in the jet with an angle of 45° using two concave mirrors (M1 and M2). The wavelength of the dye laser was scanned through the (0-0) vibrational band of N_2 first negative system around 391.4 nm and the fluorescence signal was measured by a photomultiplier tube (PM) at the Stokes shifted (0-1) band at 427.8 nm through a spectrometer with a band width of approximately 3 nm. Another PM equipped with an interference filter (IF) was also used to monitor both the spontaneous emission from the plume and the scattered dye laser light for obtaining the timing signal.

3.4 Characteristic Features of Coaxial DBD Jet

3.4.1 Dependence of plasma plume length on electrode structure

To analyze the electrode length-dependent characteristics and the optimum conditions for the applications of the coaxial DBD jet, the plume lengths were measured changing the lengths of powered and grounded electrodes. Figure 3.3 shows variations of the plume length which was the distance between the plume tip and the tube exit, as functions of the lengths of powered and grounded electrodes composed of the copper sheets. The length of the electrode with a fixed length was set at 13 mm and the distance between the two electrodes was 17 mm in this
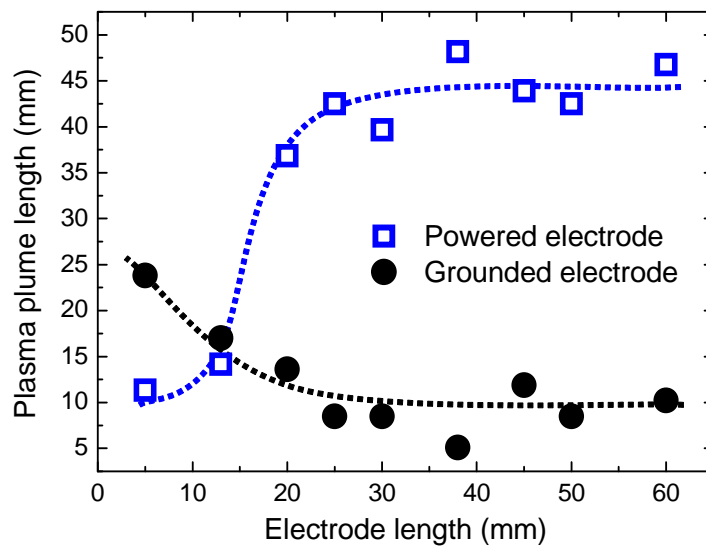
Figure 3.3   Variation of plasma plume length as a function of electrode length (powered and grounded electrodes made of copper sheets). Distance between two electrodes and length of unchanged electrode are 17 mm and 13 mm, respectively.

experiment.

As the length of powered electrode increased from 10 to 20 mm, the plume length increased markedly. The plume length became constant around 45 mm, as the length of the powered electrode increased further. Moreover, the plume length increased gradually as the length of grounded electrode decreased. From these results, the variation of electrode length enables us to control the plume length without changing any other condition. Hereafter, the typical electrode configuration, where the length of both the powered and grounded electrodes was 13 mm, is called as a "Copper sheets" configuration.

From the plume-length dependence on the electrode length, it is revealed that the longer powered and shorter grounded electrodes are better for elongating the plume. On the basis of this finding, three types of novel electrode configurations using insulated electric wires were

developed to clarify the underlying physics and maximize plume length, comparing their characteristics with those of the typical "Copper sheets" configuration. The insulated wire twisted around the tube only in one turn was used as the grounded electrode in all three types, because the plume became longer when the grounded electrode became shorter. To use as the powered electrode, a copper sheet and a spiral twisted wire, where the length of both electrodes was 30 mm, and two one-turn twisted wires separated by 30 mm were used. These novel electrode configurations are named as "Wire and sheet", "Spiral type", and "Parallel type", respectively. The distance between the grounded wire electrode and the upstream edge of the powered electrode was 10 mm in each type of novel electrode configuration. Their overviews are shown in Fig. 3.4, and the discharge emission is shown in Fig. 3.5, including the "Copper sheets" configuration.

In the "Wire and Sheet" configuration, the plume length reached nearly 50 mm and a long emission was also observed in upstream side of the tube. Using the "Spiral type" configuration, the plume became slightly shorter than that using the "Wire and sheet", and a spiral emission, which cloned the shape of spiral-wire electrode outside the tube, was observed. This cloning of discharge emission on the powered electrode has the potential to be applied to displays and lightings, when the discharge region is changed from the tube to the plane. A clear separation of emission between the coaxial DBD inside the tube and the plume was observed in the "Parallel type" configuration. This discharge separation will be analyzed in more detail with measurement results of the discharge currents in the next subsection.
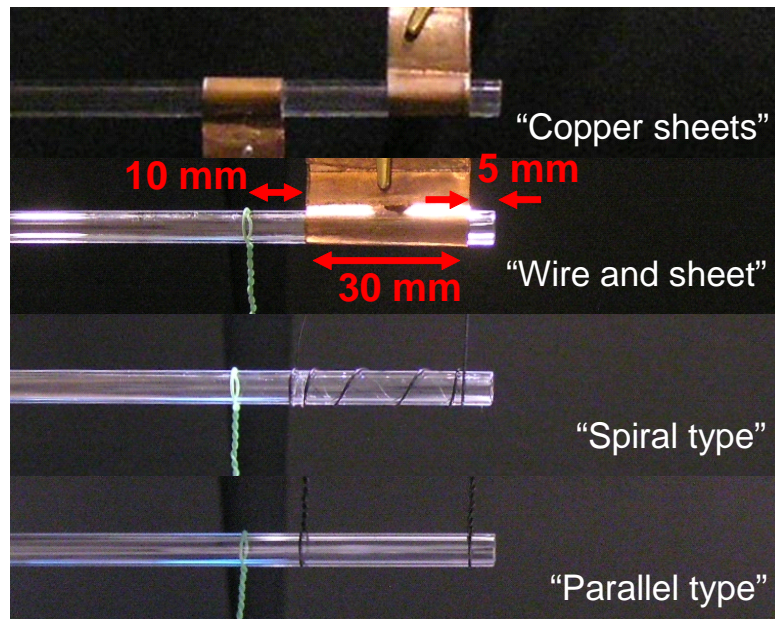
Figure 3.4 Photographs of electrode configurations in coaxial DBD jet using copper sheets and insulated wires.
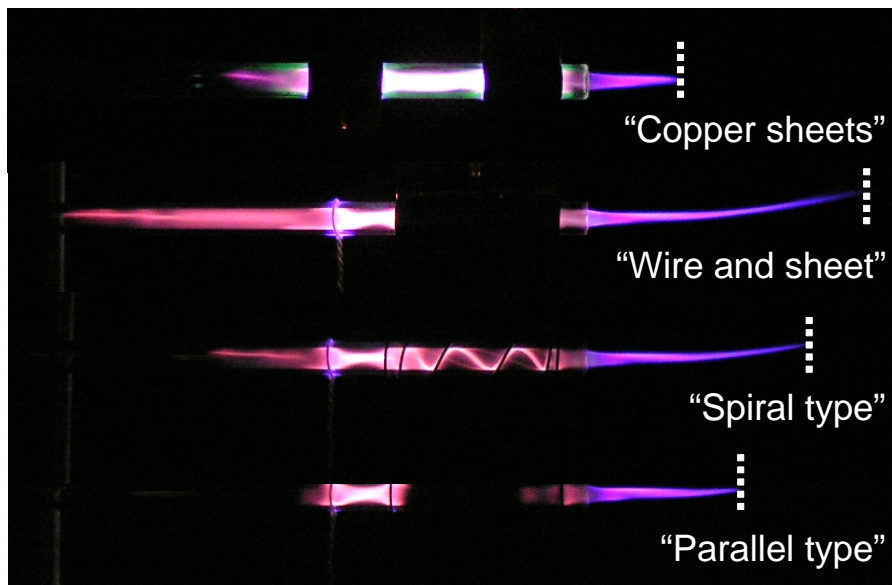

Figure 3.5 Photographs of discharge emission in coaxial DBD jet using four types of electrode configurations shown in Fig. 3.4. Shutter speed of digital camera is at 1.0 s, and white dotted lines indicate positions of plume tip in each electrode configuration.

3.4.2   Discharge current flowing both inside and outside of tube

The discharge currents flowing into the grounded electrode (see Fig. 3.1) in each electrode

configuration are shown in Fig. 3.6. The time origin was set at the rise timing of applied voltage.

The discharge currents was derived by subtracting the displacement currents measured without

the He gas flow from the originally detected currents. The peak current decreased in the order of

the "Copper sheets", "Wire and sheet", "Spiral type", and "Parallel type" configurations. From

the results shown in Fig. 3.5, it was confirmed that the plume length became longer without the

increase in discharge current, as well as input power to the coaxial DBD inside the tube.

   Owing to the exchange of grounded electrode to the insulated wire from the copper sheet, the

smaller electrode area leads to the reduction of capacitive components in the electrodes. This
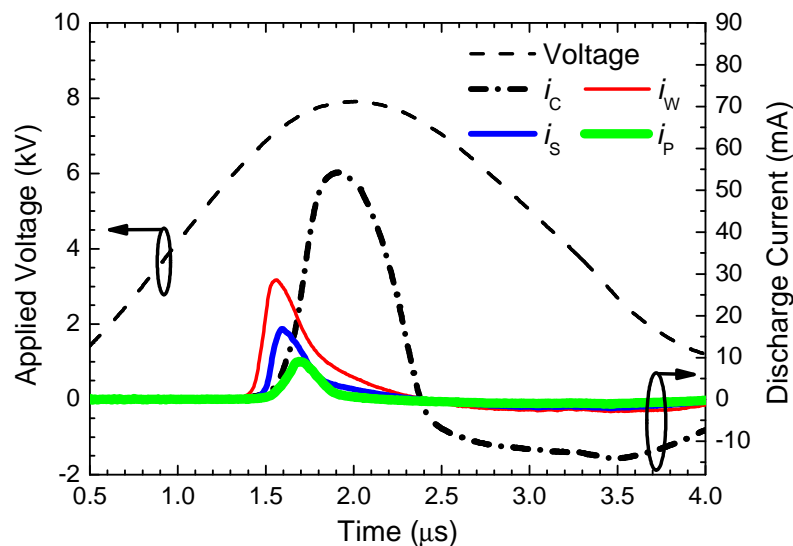

Figure 3.6   Temporal evolutions of applied voltage and discharge current flowing into grounded electrode in each electrode configuration. Electrode configurations in measurement of i_C, i_W, i_S, and i_P are "Copper sheets", "Wire and sheet", "Spiral type", and "Parallel type" electrode configurations, as shown in Fig. 3.4, respectively.

result suggests that the amount of charges accumulated on the inner tube surface, which stops the discharge by making a reverse electric field, becomes smaller as decreasing the electrode area. This mechanism can explain the current decrease in the coaxial DBD inside the tube, and be applied to the area of the powered electrode. The charge accumulation areas inside the powered electrodes are 1.63 cm^2 in the "Copper sheets", 3.77 cm^2 in the "Wire and sheet", 2.11 cm^2 in the "Spiral type", and 0.25 cm^2 in the "Parallel type" configurations. The width of charge accumulating area occupied by the insulated wire was assumed as 2 mm in the above estimation.

The discharge currents flowing in each electrode in the "Parallel type" configuration were also measured in order to confirm the electrical separation of two discharges. From the temporal evolutions, shown in Fig. 3.7, the two discharge currents flowing into the coaxial DBD inside
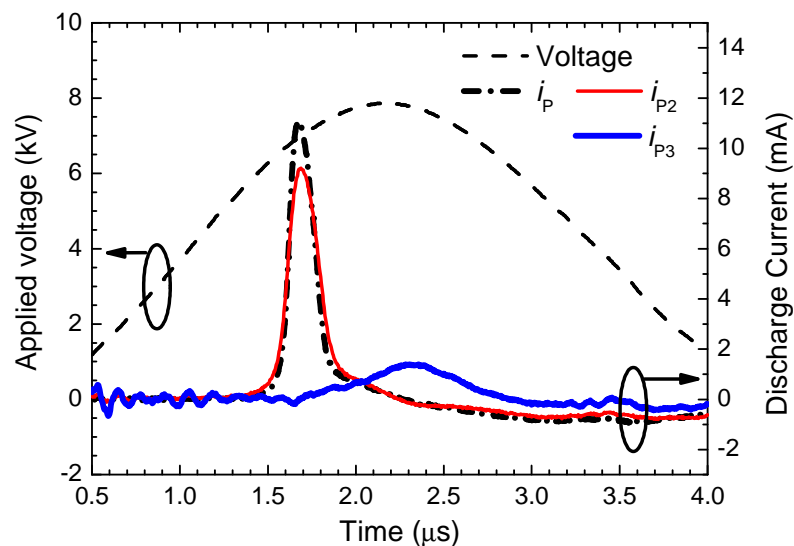

Figure 3.7   Temporal evolutions of applied voltage and discharge current in "Parallel type" electrode configuration. i_P and i_{P2} are currents flowing into grounded electrode and upstream powered electrode; i_{P3} is current flowing out from downstream powered electrode.

the tube, i_P and i_{P2}, showed the similar shapes with respect to time. On the other hand, the current for the plume generation flowing out from the downstream powered electrode, i_{P3}, was independent of that in the coaxial DBD. This result indicates that there is almost no relationship between the two discharges in this electrode configuration, and this "Parallel type" configuration is the most suitable for the independent observation of the two discharge phenomena in the four electrode configurations, although it is difficult to apply this configuration to material processes because of its short plume length, low excited-species density, and wasted power to the coaxial DBD inside the tube.

3.4.3   Line-integrated He$^{\mathrm{m}}$ density in plasma plume

Figure 3.8 shows the temporal evolutions of line-integrated He$^{\mathrm{m}}$ density measured at 10 mm from the tube exit in each electrode configuration. The laser beam was focused at 10 mm from the tube exit, and the radius of beam spot was smaller than 0.1 mm around the plume. The reduction of peak density was in the same order as that in the discharge current of the coaxial DBD inside the tube. This result indicates clearly that the plume length does not represent the excited-species density inside the plume. In the novel electrode configurations using the insulated wires, the rise timing of He$^{\mathrm{m}}$ density shifted earlier with the increase of peak density. It suggests that the propagation speed of the high-density region increases with the increase of the He$^{\mathrm{m}}$ density inside it. This interpretation is in agreement with the theory of ionization-front propagation in the positive corona discharge; the velocity of ionization front increases as the electric field, which is determined by the ion density inside the front, becomes stronger. The experimental results in each electrode configuration indicate that the decay times of He$^{\mathrm{m}}$ density range from 0.2 to 0.3 μs, and the reaction processes in the plume are not markedly
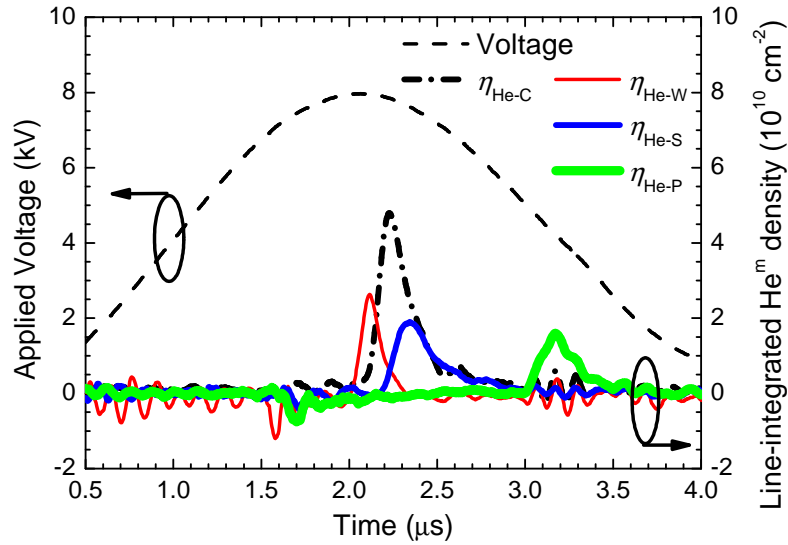
Figure 3.8 Temporal evolutions of applied voltage and line-integrated He[m] density in plasma plume measured 10 mm from tube exit, in each electrode configuration. Electrode configurations in measurements of $\eta_{\text{He-C}}$, $\eta_{\text{He-W}}$, $\eta_{\text{He-S}}$, and $\eta_{\text{He-P}}$ are "Copper sheets", "Wire and sheet", "Spiral type", and "Parallel type" electrode configurations, respectively.

different among the electrode configuration. Therefore, it can be confirmed that the plume length measured from the images obtained using the digital camera represents the length of the region where excited species exist very similarly in each electrode configuration.

3.4.4   Spatiotemporal distribution of N_2^+ density in plasma plume

The measurement result of LIF excitation spectra observed at 3 mm from the tube exit is shown in Fig.3.9. The narrow bandwidth of dye laser (0.007 nm) enabled us to distinguish each peak of the rotational components (P and R branches) of the N_2^+ first negative (0-0) band except at very near the band head.

Temporal evolutions of the LIF signal intensity representing the relative N_2^+ density were measured at several distances from the tube exit. The results at 1, 3, and 5 mm distances are
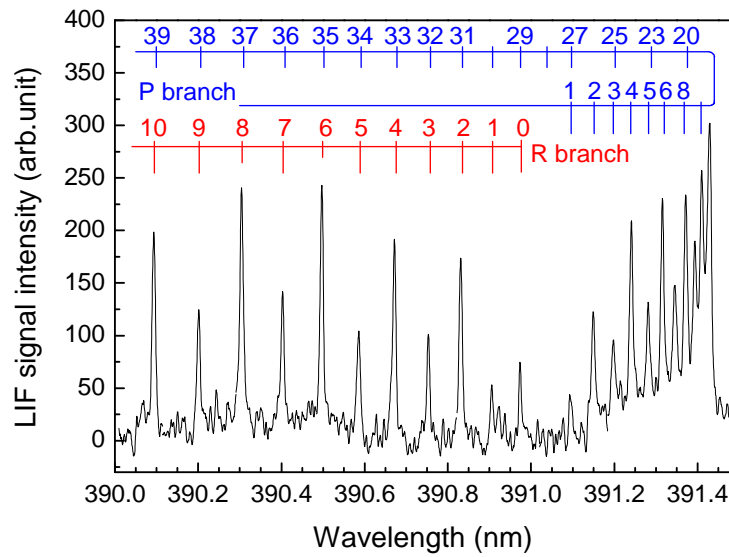
Figure 3.9 Rotational structure of LIF excitation spectra of N_2^+ first negative (0-0) band. Labeling number J is rotational quantum number of lower energy state in electronic transition.
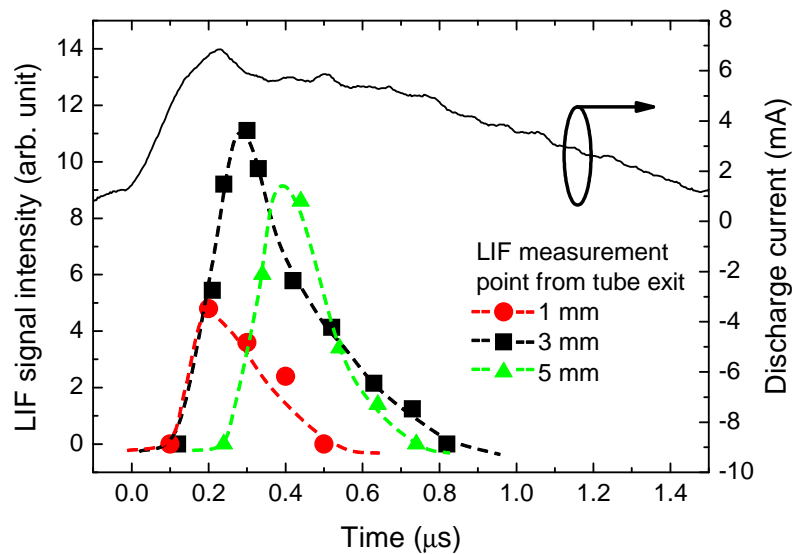

Figure 3.10 Temporal behavior of LIF intensity of N_2^+ first negative (0-0) band measured at several points from the nozzle exit together with the discharge current waveform measured at the grounded electrode.

shown in Fig. 3.10 with the waveform of discharge current. The time origin is set at the rise

timing of the current in this figure, while the applied voltage preceded to the current is kept

almost constant at the high level in this figure. It is seen that the N_2^+ density increases with

the distance and it peaks at 3 mm and decreases afterwards. This behavior is due to increasing

air contaminating by diffusion into the He gas flow and decreasing excited species of the He

atoms. The temporal shift of the peaks with distance gives an apparent propagation velocity of

approximately 20 km/s. This velocity is consistent with previously reported values measured

by ICCD-camera observations. [3.8, 9]

3.5   Formation Mechanisms of Plasma Plume

3.5.1   Behavior of N_2^+ ions in plasma plume

As the first step of discussions about formation mechanisms of the plasma plume in the coaxial

DBD jet, the suggested mechanisms of ionization-front propagation is verified through com-

paring the N_2^+ ions' velocities of thermal motions and drift by the external electric field. When

the rotational population density is in thermal equilibrium at the defined temperature T_{rot}, the

LIF signal intensity $I_{LIF}(J_{rot})$ normalized by the degeneracy of lower rotational level with the

quantum number J_{rot} should follow the relation [3.10]

$$\ln\left(\frac{I_{LIF}(J_{rot})}{2J_{rot}+1}\right) \propto \frac{B_v hc}{K_B T_{rot}} J_{rot}(J_{rot}+1) \tag{3.1}$$

where B_v (1.92 cm^{-1} for the lowest vibrational level, $v = 0$) is the rotational constant of ground

N_2^+ ions, [3.11] h is the Planck constant, K_B is the Boltzmann constant, and c is the velocity of
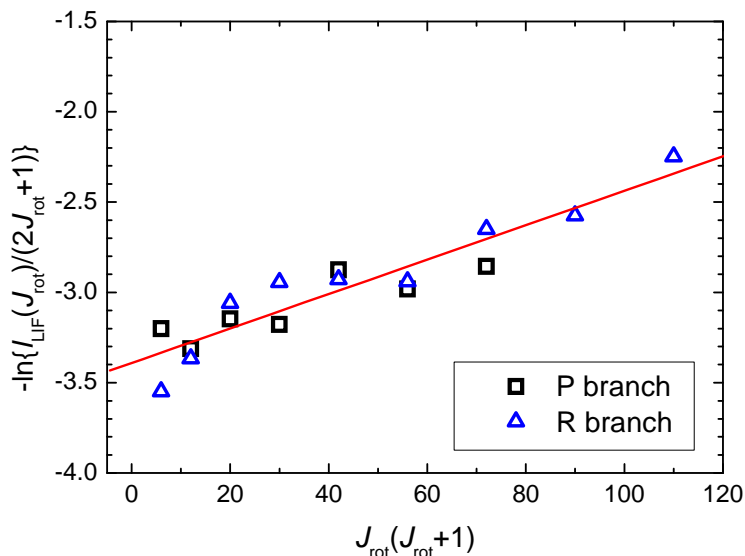
Figure 3.11 Plot of $-\ln[I_{\text{LIF}}(J_{\text{rot}})/(2J_{\text{rot}}+1)]$ as a function of $J_{\text{rot}}(J_{\text{rot}}+1)$ (data points) and least-square fitted straight line, where $I_{\text{LIF}}(J_{\text{rot}})$ is LIF signal intensity of $P(J_{\text{rot}})$ or $R(J_{\text{rot}})$ component with rotational quantum number J_{rot} as in Fig. 3.9.

light. The analyzed peak intensities $-\ln[I_{\text{LIF}}(J_{\text{rot}})/(2J_{\text{rot}}+1)]$ vs $J(J+1)$ are plotted in Fig. 3.11 with the least-square fitted line. In this plot, the values of $I_{\text{LIF}}(J_{\text{rot}})$ with odd J_{rot} numbers have been doubled according to the intensity alternation rule, [3.10] and those with larger J_{rot} numbers (18) have been assumed to be negligibly small as can be verified from the unnoticeable intensity of the isolated P(26) component. From the gradient of straight line in Fig. 3.11, T_{rot} was determined as 292±20 K. Except at very low pressures, it can be assumed that the rotational temperature is in equilibrium with the translational temperature of ground N_2^+ ions and also the ambient gas temperature T_{g}. [3.12] Therefore, this result indicates that T_{g} in the plume is kept near room temperature.

Figure 3.12 shows the enlarged line profile of the LIF spectrum of the R(8) rotational component, which is well isolated from other components (see Fig. 3.9). First, if it is supposed that the plasma bunch is traveling with the apparent velocity described above, the observed spectra is
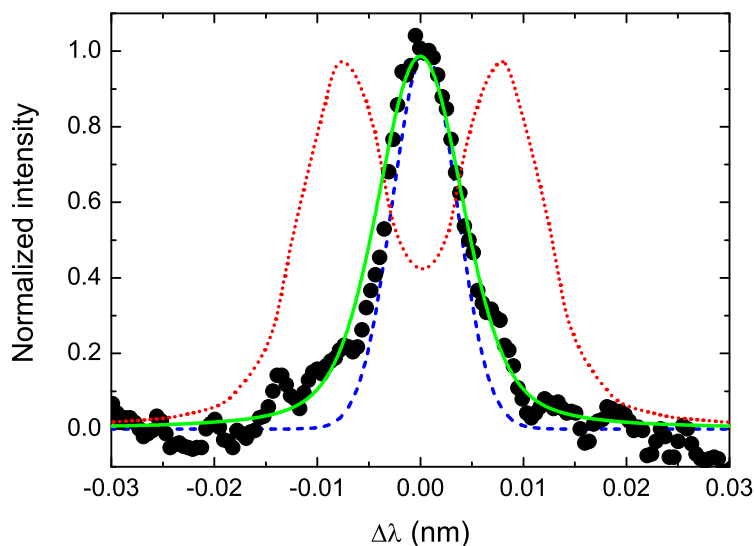
Figure 3.12   Measured line profile of R(8) rotational component (data points) and fitted curve with Voigt profiles (solid line) as compared with profile measured in low-pressure hollow cathode discharge (dashed line) and synthesized profile with hypothetical Doppler shift with ion velocity of 10 km/s (dotted line).

expected to be split into double-peaks due to the Doppler effects in our 45° tilted configuration. A hypothetical line profile synthesized from the measured one with a translational velocity of 10 km/s is drawn in the figure (dotted line). However, there is no evidence seen in the observed profile for such a splitting. For a further inspection of the profile, the same line profile measured in a low-pressure hollow cathode discharge is plotted as a reference. The result shows that the profile can be fitted with a single Gaussian profile whose half width is much larger than the reported spin splitting approximately 0.002 nm, [3.13] and thus it represents equivalently the instrumental profile including the finite spectral width of the dye laser. It is noticed that the profile measured in the plasma plume has a little bit larger width than that of the reference profile. Fitting result of the LIF spectrum measured in the plume with a Voigt profile is shown in the figure with a solid line. The Lorentzian component of $\Delta\lambda_L = 0.0035$ nm additional to the given

Doppler component yields a value of the collision broadening coefficient of about 0.92×10^{20} cm^2. This value is consistent, at least in the order, with the reported data for the foreign gas broadening coefficients of argon and neon lines in He gas. [3.14] This result shows that there is no noticeable drift velocity that can be assigned for the translational motion of N$_2^+$ ions which compose the major ionic species in the plume under the present situation.

These investigation results of the N$_2^+$ ions' behaviors have good agreements with the discharge mechanisms of ionization-front propagation. This is because that localization of high electric-field region just in front of the ionization front leads to small electron avalanches without enough time to transfer electrons' energy to gas particles and weak electric field behind the front which cannot move charged particles in the plume.

3.5.2 Relationship between excited species in plasma plume and accumulated charges on inner tube surface

In discussion of the relationships between the plasma plume and the coaxial DBD inside the tube, it is important to consider surface-charge densities accumulated on the inner tube surface owing to the coaxial DBD. Calculated results of the surface-charge density and the measured results of the peak line-integrated He^m density in the plume for each electrode configuration are shown together with the plume lengths in Table 3.1. The surface-charge density on the inner tube surface was calculated by dividing the surface charge, which was one-half of convergent value of the integrated discharge current, by the inner surface area of the tube wrapped by the powered electrode. In the "Parallel type" electrode configuration, the discharge current flowing out from the downstream-powered electrode was used to calculate the surface-charge

Table 3.1 Plasma plume length (shown in Fig. 3.5), surface-charge density accumulated owing to coaxial DBD inside tube (calculated from discharge current shown in Figs. 3.6 and 3.7), and peak line-integrated He^m density (shown in Fig. 3.8) in each electrode configuration shown in Fig. 3.4.

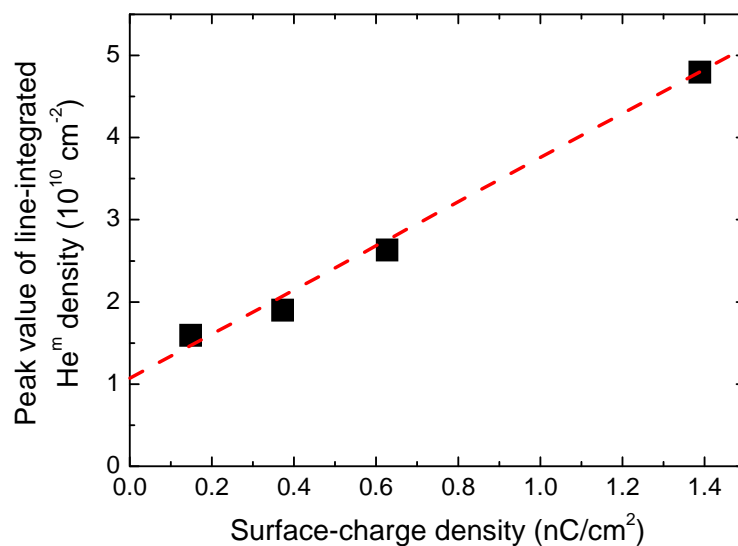| Electrode configuration	Plasma plume length (mm)	Surface-charge density (nC/cm^2)	Peak line-integrated He^m density (10^{10} cm^{-2})
Copper sheets	15	1.39	4.80
Wire and sheet	48	0.63	2.63
Spiral type	37	0.37	1.90
Parallel type	25	0.15.	1.59

Figure 3.13 Relationship between surface-charge density accumulated owing to coaxial DBD inside tube and peak line-integrated He^m density in plasma plume, measured 10 mm from tube exit. Red dotted line shows linear fit of these four experimental results.

density because of the discharge separation between the coaxial DBD and the plume. There was a proportional relationship between the surface-charge density and the peak line-integrated He^m density, as shown in Fig. 3.13. This relationship indicates that the strength of electric field generated by the surface charge is one of the most important factors for controlling the plasma properties in the plasma plume. This also reveals the position of localized breakdown that triggers the ionization-front propagation, which should be on the inner tube surface at the downstream edge of powered electrode.

In addition to the discussion on the surface-charge density, generation efficiencies of excited species in the plasma plume were calculated considering the electric-power consumption to the coaxial DBD jet in each electrode configuration. The efficiency was defined as the quotient of peak line-integrated He^m density in the plume, shown in Table 3.1, and the peak electric power, which is the product of peak discharge current and instantaneous applied voltage when the current peaks, as shown in Fig. 3.6. The calculated efficiencies were 1.12×10^8 cm^2/W in the "Copper Sheets", 1.29×10^8 cm^2/W in the "Wire and sheet", 1.56×10^8 cm^2/W in the "Spiral type", and 2.33×10^8 cm^2/W in the "Parallel type" configurations. The generation efficiency of excited species in the plume increased with the decrease in electrode area, although the peak density decreased. This result suggests that integrating of the coaxial DBD jets having a small electrode area is a more effective way to increase the excited-species density than increasing the electrode area.

3.5.3   Localized breakdown on inner surface of glass tube

To investigate the ignition of the ionization front in more detail, spatial distributions of electrical potential and electric-field magnitude were calculated by the 2D axisymmetric finite el-

ement method. [3.15] From a previous report, the ionization-front propagation starts when the instantaneous applied voltage reaches at 4.6 kV. [3.16] Therefore, the applied voltage and the surface-charge density used in this calculation were measured at the timing of 1.1 μs, as shown in the abscissa time axis of Fig. 3.14, which shows the temporal evolutions of applied voltage and surface-charge density in the electrode configurations of "Copper sheets" and "Wire and sheet". In this calculation, the spatial distribution of surface-charge density was uniform on the inner tube surface, because the surface charge has been accumulated by the coaxial DBD in the negative voltage phase (approximately 100 μs before the ignition). From the 2D distribution of electric-field magnitude in the "Copper sheet" configuration shown in Fig. 3.15, there were two localized high-field regions at the downstream edge of powered electrode and surface charge. The r and z axes are defined as the radial and central axes of the glass tube as shown in Fig.
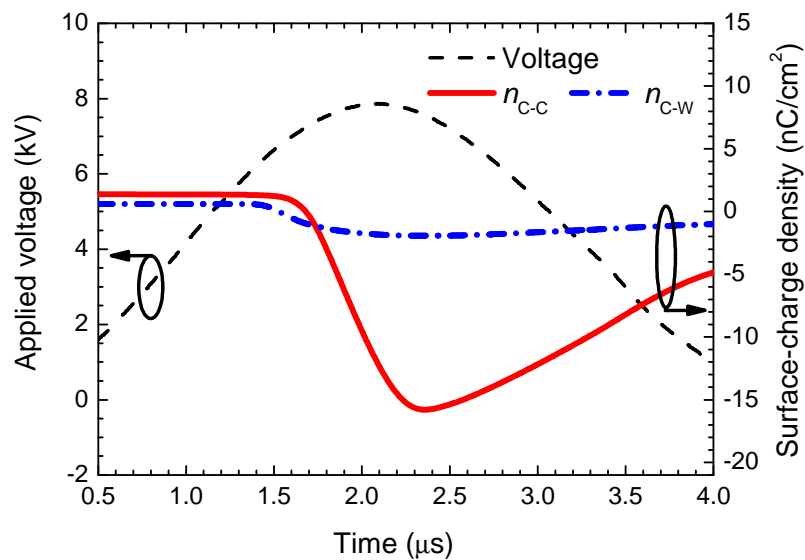

Figure 3.14 Temporal evolutions of applied voltage and surface-charge density accumulated by coaxial DBD inside tube. n_{C-C} and n_{C-W} are surface-charge densities in electrode configurations of "Copper sheets" and "Wire and sheet", respectively.
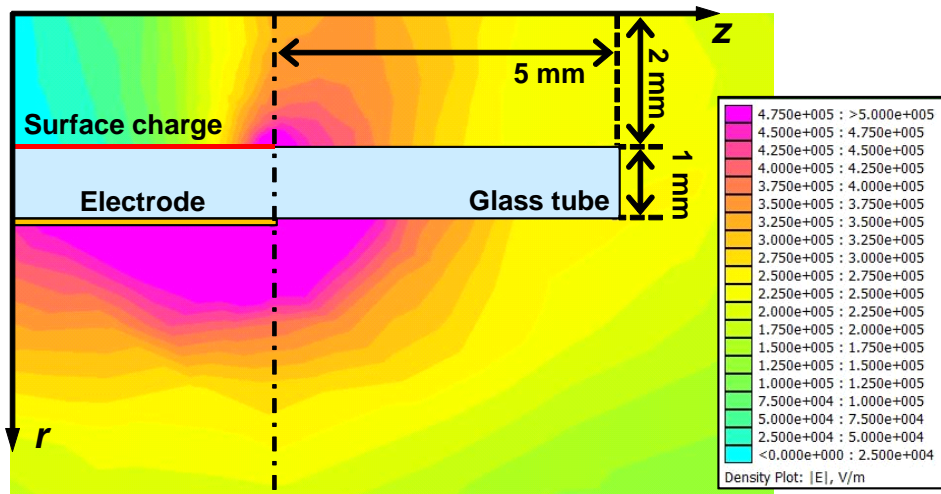
Figure 3.15 Axisymmetric 2D distribution of electric-field magnitude near tube exit calculated by finite element method in "Copper sheets" configuration. Applied voltage and surface-charge density used in this calculation were measured at 1.1 μs, as shown in Fig. 3.14. r and z axes are respectively radial and central axes of glass tube, and origin of these axes is set at center of tube exit.
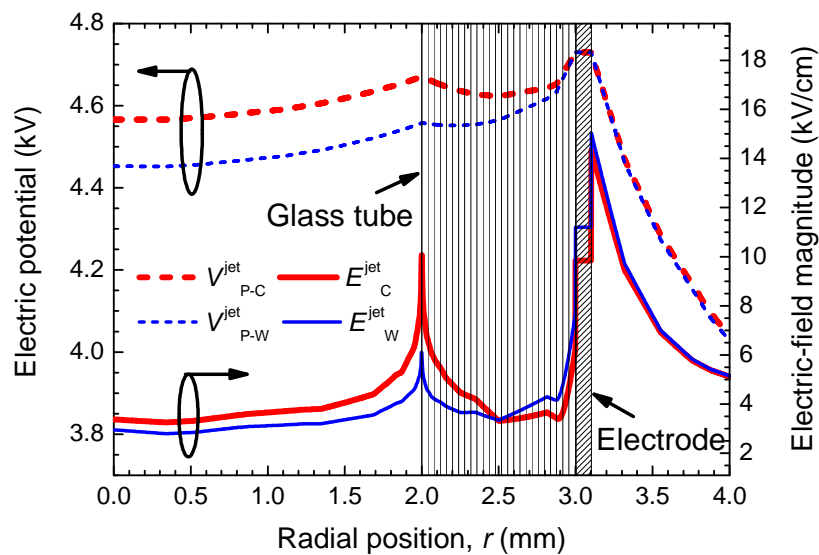

Figure 3.16 Radial distributions of electric potential $V_{\mathrm{P}}^{\mathrm{jet}}$ and electric-field magnitude E^{jet} within 5 mm from tube exit (along dashed-dotted line in Fig. 3.15, $z = -5.0$ mm). Distribution is calculated by finite element method in electrode configurations of "Copper sheets" and "Wire and sheet" (putting subscripts of "-C" and "-W", respectively) at timing of 1.1 μs, as shown in Fig. 3.14.

3.15, and the origin of *rz* plane was set at the center of tube exit.

To compare the localized field magnitudes in the electrode configurations of "Copper Sheets" and "Wire and Sheet", 1D distributions of the electrical potential and the field magnitude along the dashed-dotted line ($z = -5.0$ mm) in Fig. 3.15 are plotted in Fig. 3.16. From this figure, the field magnitudes were larger at the edge of electrode than that of surface charge. However, air plasma cannot be ignited at this magnitude, and the localized breakdown can occur at the edge of surface charge because the field magnitude there is larger than 4.0 kV/cm, which is a corona breakdown field magnitude in atmospheric-pressure He gas. [3.17]

3.5.4   Decision mechanism of plasma plume length

For discussion on the plasma plume length, which is independent from the excited-species density inside the plume, as revealed by the results shown in subsection 3.3.3, the temporal evolutions of electrical potential at the starting point of ionization-front propagation ($r = 2.0$ mm and $z = -5.0$ mm in Fig. 3.15) were calculated assuming a uniform surface-charge distribution in all time steps, as shown in Fig. 3.17. This calculation was performed with a time step of 0.1 μs using the instantaneous values of the applied voltage and the surface-charge density shown in Fig. 3.14. Owing to the accumulation of larger negative charges in the "Copper sheets" electrode configuration, the decay of electrical potential was faster than that in the "Wire and sheet" after the start of the current flow of the coaxial DBD. This potential decay stops the propagation of the ionization front and affects the plume length.

From these results, it is revealed that the important factor for the control of plume length is the temporal evolution of surface-charge density, which is affected by the electrode area in the coaxial DBD inside the tube. Therefore, the dependence of the plume length on the grounded-
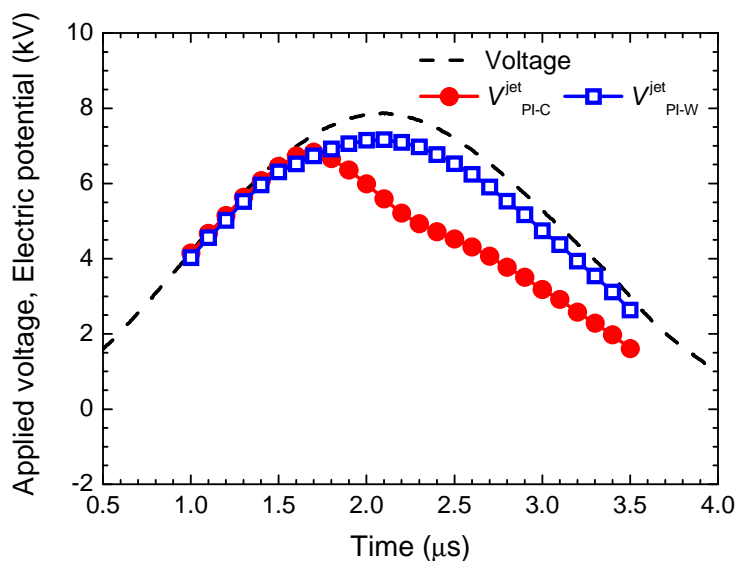
Figure 3.17   Temporal evolutions of applied voltage and electric potential on inner tube surface at downstream edge of powered electrode ($z = -5.0$ mm and $r = 2.0$ mm) calculated by finite element method. $V^{\text{jet}}_{\text{PI-C}}$ and $V^{\text{jet}}_{\text{PI-W}}$ are electric potentials in electrode configurations of "Copper sheets" and "Wire and sheet", respectively.

electrode length, as shown in Fig. 3.3, can be explained by the change in the temporal evolution of surface-charge density similar to the powered-electrode shape. Moreover, considering the dependence of He^{m} density on surface-charge density, as discussed in subsection 3.4.2, it is possible to control the plume length and the excited-species density independently by changing the temporal evolution of surface-charge density and instantaneous density at the starting time of ionization-front propagation.

3.6   Summary

In summary, the characteristics of the plasma plume in the coaxial DBD jet are investigated from view points of spatiotemporal behaviors of excited species measured by LAS and LIF methods and relationships between the coaxial DBD inside the tube and the plasma plume.

Applying the LIF method to diagnose the coaxial DBD jet, behaviors of the N_2^+ ions in the plasma plume were successfully analyzed. From the obtained results, it was confirmed that the high-speed emissive region effused into ambient air is similar to that of the ionization-front propagation in the positive corona discharge, but in the present case the ground is at an infinite distance. In that situation, the initial electrons in the plasma plume outside of the tube are collected to the powered electrode and then the remaining ions attract ambient electrons through the He gas channel in which a higher electron drift velocity favorably works for the acceleration forming the ionization front. This mechanism of ion behavior in the plume is different from that in the coaxial DBD occurring inside of the tube.

Also, from experimental results using novel electrode configurations with the insulated wires, a decrease in electrode area led to reduction of the input power to the coaxial DBD inside the tube and increased the plume length at the same time. From the line-integrated He^m density inside the plume in each electrode configuration, the excited-species density inside the plume is proportional to the surface-charge density on the inner tube surface at the powered electrode. These experimental results suggest that changing the electrode configuration enables us to control the plume length and the excited-species density independently, and the relationship between the coaxial DBD inside the tube and the plasma-plume formation is associated with the charge transfer that generates the localized electric field at the downstream edge of powered electrode inside the tube, where the ionization-front propagation takes place. Moreover, the calculated results of electrical potential distribution indicate that the potential decrease at the starting point of the ionization front is changed by the electrode configuration, and this decay difference causes the difference in the time duration of the ionization-front propagation as well as the plume length.

References

[3.1] X. Lu and M. Laroussi: J. Appl. Phys. **100** (2006) 063302.

[3.2] B. L. Sands, B. N. Ganguly, and K. Tachibana: Appl. Phys. Lett. **92** (2008) 151503.

[3.3] K. Urabe, Y. Ito, M. Kubo, and K. Tachibana: Proc. EU-Japan Joint Symp. Plasma Processing, 2008, p. 82.

[3.4] K. Tachibana, Y. Kishimoto, and O. Sakai: J. Appl. Phys. **97** (2005) 123301.

[3.5] T. Somekawa, T. Shirafuji, O. Sakai, K. Tachibana, and K. Matsunaga: J. Phys. D **38** (2005) 1910.

[3.6] J. Allison, T. Kondow, and R. N. Zare: Chem. Phys. Lett. **64** (1979) 202.

[3.7] R. A. Gattscho, R. H. Burton, D. L. Flamm, V. M. Donnelly, and G. P. Davis: J. Appl. Phys. **55** (1984) 2707.

[3.8] M. Teschke, J. Kedzierski, E. G. Finantu-Dinu, D. Korzec, and J. Engemann: IEEE Trans. Plasma Sci. **33** (2005) 310.

[3.9] J. Kedzierski, J. Engemann, M. Teschke, and D. Korzec: Solid State Phenom. **107** (2005) 119.

[3.10] G. Hertzberg: *Molecular Spectra and Molecular Structure* I: *Spectra of Diatomic Molecules* (Van Nostrand Reinhold Company, New York, 1950).

[3.11] K. P. Huber and G. Hertzberg: *Molecular Spectra and Molecular Structure* IV: *Constants of Diatomic Molecules* (Van Nostrand Reinhold Company, New York, 1979).

[3.12] D. Staack, B. Farouk, A. F. Gutsol, and A. A. Fridman: Plasma Sources Sci. Technol. **15** (2006) 818.

[3.13] K. A. Dick, W. Benesch, H. M. Crusswhite, S. G. Tilford, R. A. Gottscho, and R. W.

Field: J. Mol. Spectrosc. **69** (1978) 95.

[3.14] G. H. Copley: J. Quant. Spectrosc. Radiat. Transfer **16** (1976) 377.

[3.15] D. C. Meeker: Finite Element Method Magnetics Ver. 4.2 (built in 2008) [http://femm.foster-miller.net].

[3.16] K. Urabe, T. Morita, K. Tachibana, and B. N. Ganguly: J. Phys. D **43** (2010) 095201.

[3.17] S. Otori, T. Sekiguchi, and T. Kono: *Denri Kitairon* (Theory of Ionized Gases) (Denki Gakkai, Tokyo, 1969) [in Japanese].

Chapter 4

Jet-Type Dielectric Barrier Discharge[†]

4.1 Introduction

In this chapter, discharge mechanisms a jet-type dielectric barrier discharge (DBD) operated in helium (He) gas flow ejected into ambient air are investigated from a view point of spatiotemporal distributions of excited-species density in the plasma plumes. At the outside of plume, the gas composition becomes a mixture of the He and ambient air (mostly nitrogen (N_2)), and Penning ionization takes place between He metastable atoms and neutral N_2 molecules, which may play an important role in the propagation of ionization front. [4.1, 2] In order to investigate the kinetic processes from spatiotemporally resolved measurements, a laser absorption spectroscopy (LAS) method for He metastable 2^3S_1 (He^m) atoms [4.3] and a laser-induced fluorescence (LIF) method for ionic N_2 molecules in the $X^2\Sigma_g^+$ ground-state ($N_2^+(X)$) [4.4] were used to measure their density distributions. The discharge behaviors in both rise and fall timings of applied voltage are compared from the measured radial distributions of excited species in the plume.

The electrode configuration named as the "jet-type DBD" is that in which the ionization front in the coaxial DBD jet is allowed to reach the grounded conductive substrate (the third

electrode). [4.5, 6] Although this discharge type is important for the practical application to material processes with a substrate placed at a finite distance, there is little research investigating the details of this jet-type DBD is available. In the jet-type DBD, the electric field becomes much stronger than in the discharge mode without the conductive substrate (the coaxial DBD jet tested in chapter 3), and the DBD's main currents take the paths not only between the pair electrodes inside the glass tube but also between the front electrode and the conductive substrate. The discharge mechanisms causing the change to the jet-type DBD are discussed based on the dominant ionization processes occurring near the substrate as observed by the LAS and LIF measurements combined with additional optical emission spectroscopy (OES) measurements.

4.2   Jet-Type DBD in He Gas Flow Surrounded by Atmospheric Air

A schematic diagram of our experimental setup for the jet-type DBD generation and the waveform of applied voltage are shown in Fig. 4.1, with *xyz* axes to explain laser beam paths in both the LAS and LIF measurements. Glass tubes (inner diameter, d_{tube}: 2, 3, and 4 mm) were equipped with two 13-mm wide copper-ring electrodes at a separation of 20 mm. A bipolar impulse power supply, with the voltage waveform as shown in Fig. 4.1, was used at a repetition frequency of 5 kHz, and the FWHM (full width at half maximum) of the voltage impulse was 2.38 μs. [4.7] Atmospheric-pressure He gas was fed at 2.80 L/min, which generated a laminar flow with velocities of 3.71, 6.60, and 14.85 m/s in the glass tubes having inner diameters of 2, 3, and 4 mm, respectively. In order to observe the characteristics of the jet-type DBD, a grounded copper plate was placed at a distance of 20 mm from the tube exit. The applied voltage and the discharge current flowing into the grounded electrode were measured using a
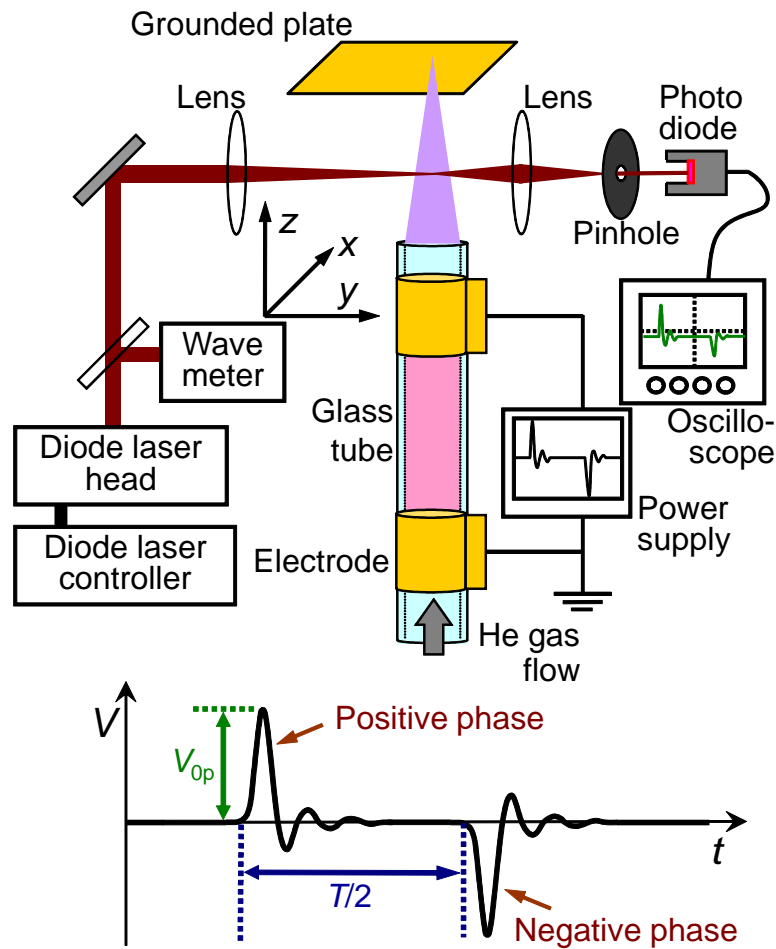
Figure 4.1 Schematic diagram of jet-type DBD generation and LAS measurement with applied voltage waveform (V_{0p}: peak value, T: repetition cycle).

high voltage probe and a Rogowski coil, respectively, and the data was stored in a digital oscilloscope. The examples of these measured waveforms are shown in Fig. 4.2. The discharge conduction current was estimated by subtracting the displacement current, which was measured from the no discharge condition without the He gas flow, from the original current waveform.

The radial distribution of gas composition outside the glass tube was numerically calculated by using a solver for computational fluid dynamics (PHOENICS version 3.5.1, Concentration Heat & Momentum Limited). [4.8] Figure 4.3 shows the calculated results of radial distributions of the He gas ratio to the ambient air from 100% to 0% in a contour diagram in three kinds of
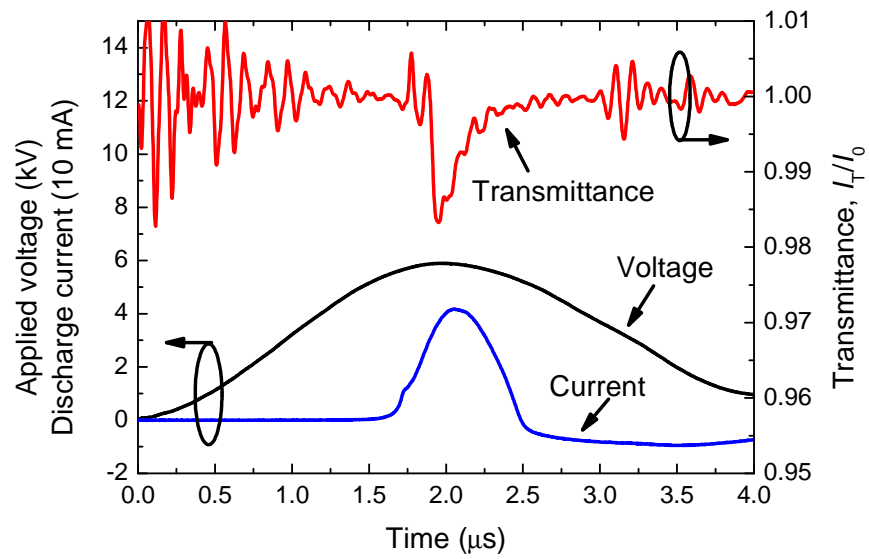
Figure 4.2 Waveform of LAS transmittance signal measured in positive voltage phase together with waveforms of applied voltage and discharge current flowing into grounded ring electrode.
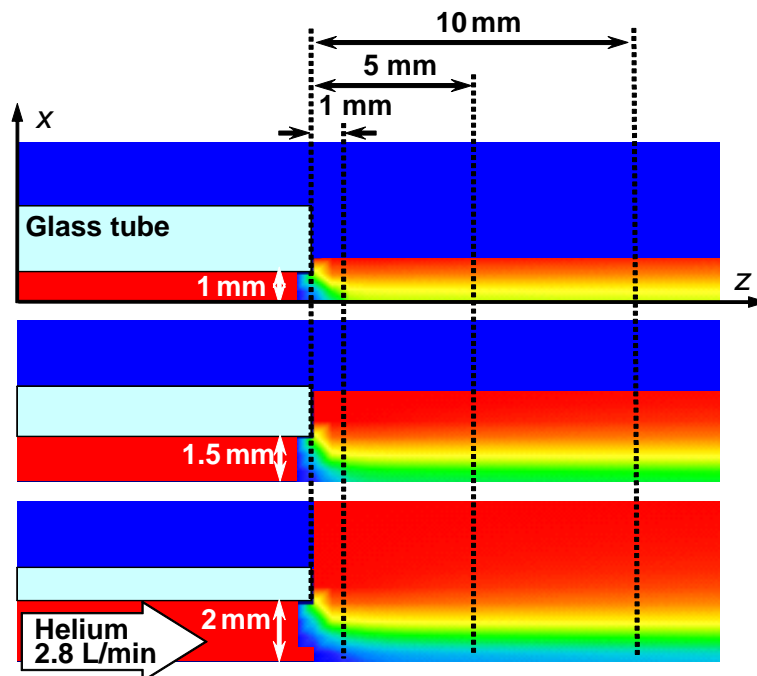

Figure 4.3 Radial distributions of gas composition in He gas flow ejected into ambient air (shown by color code from blue: 100% He, to red: 100% ambient air) calculated for 6-mm diameter glass tubes with three different inner diameters; d_{tube} = 2, 3, and 4 mm at flow rate of 2.80 L/min.

the glass tubes having inner diameters of 2, 3, and 4 mm with 2.8-L/min He gas flow.

4.3   Behavior of Excited Species in Operating Condition without Grounded Plate

4.3.1   Spatiotemporal structure of He^m density

Figure 4.4 shows spatiotemporal distributions of the He^m absorption in the positive voltage phase measured by the LAS method at V_{0p} = 6.0 kV. A larger bore (d_{tube} = 4 mm) glass tube was used and the laser beam position was scanned along the x and z axes with a step of 1 mm,
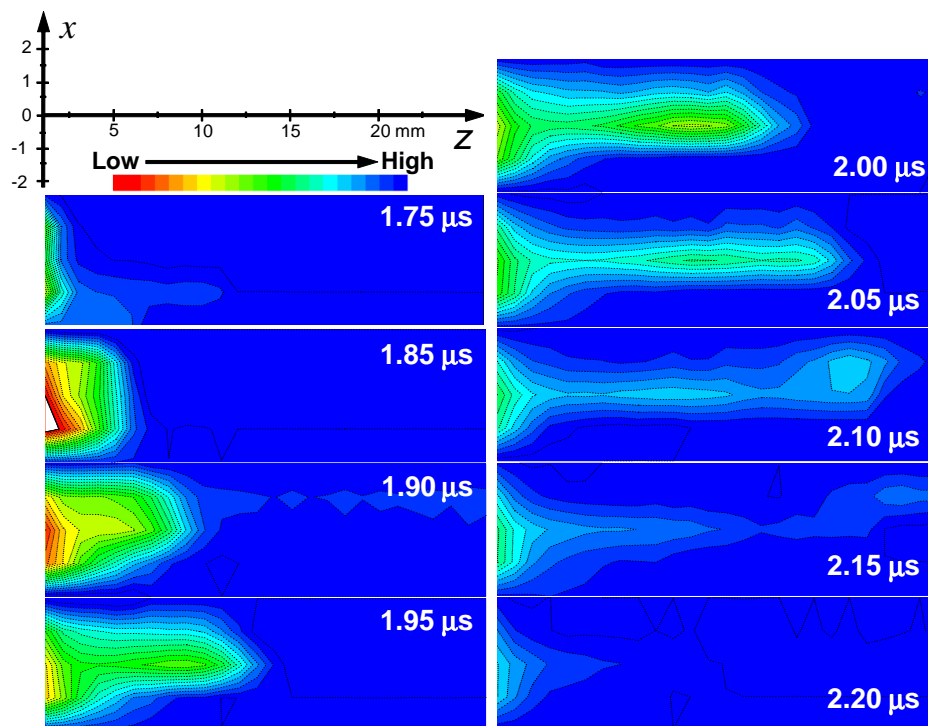

Figure 4.4   Spatiotemporal distributions of line-integrated He^m absorption in contour diagram (with color code) in the positive voltage phase without grounded plate with V_{0p} = 6.0 kV and d_{tube} = 4 mm (white region indicates the overflowed region with absorption more than 0.024). Time scale is matched with abscissa axis of Fig. 4.2.

covering the whole cross sectional area of the plasma plume.

For the situation where the gas composition is uniform and the absorption line profile does not change along the laser path, the absorption coefficient of the He^m atom a_{He^m} becomes proportional to the He^m density, so that this quantity can be directly related to the He^m density, n_{He^m}, as given by the last term of the following equation

$$- \ln(I_T/I_0) = \int_0^{l_{plasma}} a_{He^m}(y) dy \cong C_{LAS} \int_0^{l_{plasma}} n_{He^m}(y) dy \qquad (4.1)$$

where C_{LAS} is a constant value and l_{plasma} is the length of plasma along the laser path which is explained in the previous chapter. [4.9] This quantity $- \ln(I_T/I_0)$ is name as "He^m absorption" hereafter, and will be used to show the spatiotemporal behaviors of the He^m absorption.

However, from this figure it is difficult to estimate the absolute He^m density because of the non-uniformities of radial distribution in the absorption coefficient and the gas composition. Thus, this figure shows only the two-dimensionally projected distribution of the He^m absorption, which gives an image of the temporal evolution of the line-integrated He^m density in a time step of 50 ns. From this result, it was observed that the high-density region of He^m atoms elongates along the He gas flow, in which the tip velocity was approximately 50 km/s, which was consistent with the propagation velocity of bullet-like emission observed in the coaxial DBD jet with ICCD camera. [4.10–13] A longer tail than that of the bullet-like emission was observed in the He^m density distribution, because the lifetime of metastable atoms is longer than that of radiating atoms from upper excited states having allowed transitions.

4.3.2 Radial distribution of He^m and N_2^+ densities

Averaging the upper and lower parts of the spatial distribution in Fig. 4.4 with an assumption of cylindrically symmetric distribution, the radial distributions of absolute He^m densities were calculated by the procedure described in the appendix of reference [4.14] at distances of $z = 1$, 5, and 10 mm from the tube exit. The results measured in the positive voltage phase with the tube of 4-mm bore at $V_{0p} = 7.0$ kV are shown in Fig. 4.5. The data corresponds to the radial profile at the timing of peak density at each axial position; 1.66 μs (1 mm), 1.70 μs (5 mm), and 1.77 μs (10 mm). It was seen that the He^m density had a ring-like hollow shape in the center, as suggested by the temporal-resolved observation with the ICCD camera. [4.15] The ring radius and the peak density decreased gradually with the distance from the tube exit. The FWHM
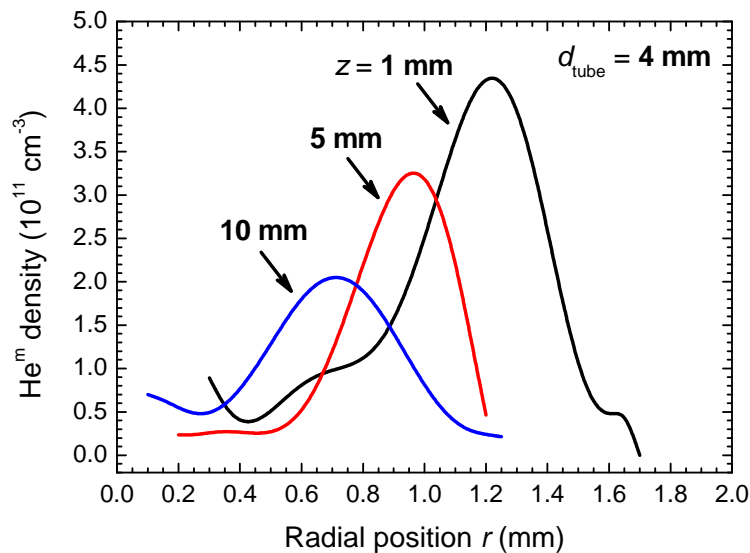

Figure 4.5 Radial distributions of absolute He^m density in positive voltage phase without grounded plate measured with 4-mm bore tube at $V_{0p} = 7.0$ kV. Measurement timings for radial profiles at three axial positions; $z = 1$, 5, and 10 mm are 1.66 μs (for $z = 1$ mm), 1.70 μs (5 mm), and 1.77 μs (10 mm) corresponding to abscissa axis of Fig. 4.2.

of the He^m density distribution (thickness of the ring) was approximately 0.4 mm at all three positions.

The radial distributions of He^m density in the positive voltage phase using the tubes with different inner diameters of 2, 3, and 4 mm were also measured at the same distance of $z = 5$ mm from the tube exit at the same V_{0p} of 7.0 kV. The data shown for each tube also correspond to the profile at the peak density timing; 2.12 μs (2 mm), 1.88 μs (3 mm), and 1.70 μs (4 mm). As seen in Fig. 4.6, the peak density in each tube was more or less the same in a range of $(3.5 \pm 0.5) \times 10^{11}$ cm^{-3}. It is noted that the thickness of the ring is again approximately 0.4 mm in all three cases with different bore sizes.

Figure 4.7 shows the radial distribution measured in the negative voltage phase with $V_{0p} = 7.0$ kV. The inner diameter of the tube was 4 mm and the LAS measurement was at a distance
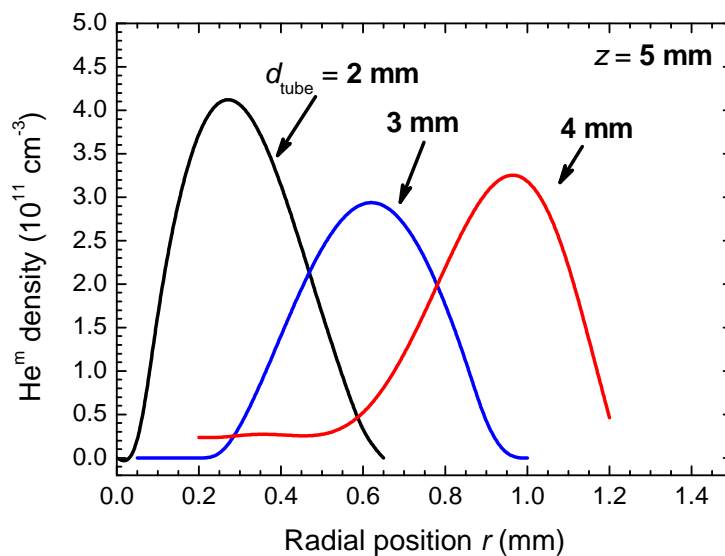

Figure 4.6   Radial distributions of absolute He^m density in positive voltage phase without grounded plate measured at $V_{0p} = 7.0$ kV and $z = 5$ mm with tubes of three different inner diameters; $d_{tube} = 2$, 3, and 4 mm. Measurement timings are 2.12 μs (for $d_{tube} = 2$ mm), 1.88 μs (3 mm), and 1.70 μs (4 mm) corresponding to abscissa axis of Fig. 4.2.
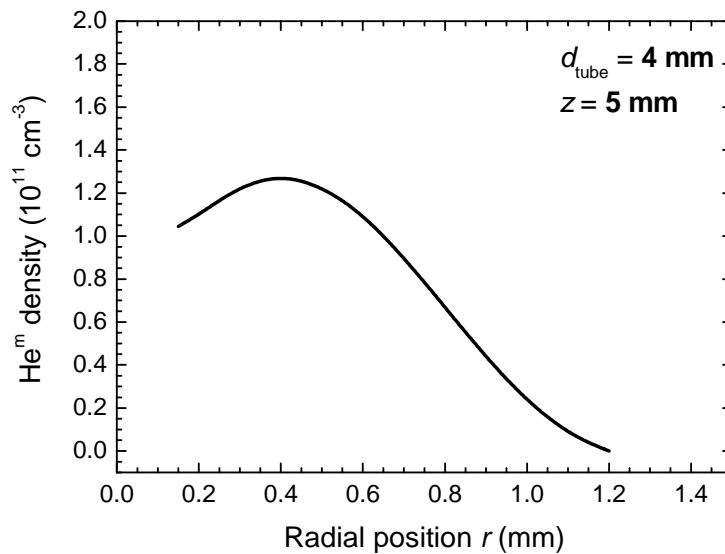
Figure 4.7   Radial distribution of absolute He^m density in negative voltage phase without grounded plate measured with 4-mm bore tube at V_{0p} = 7.0 kV and z = 5 mm at timing of 1.96 μs corresponding to abscissa axis of Fig. 4.9(b).

of z = 5 mm from the tube exit at the peak timing of 1.96 μs (see Fig. 9(b)). It is noted that, in this case, the radial distribution of He^m density has a high-density area near the center of the plasma plume in contrast to the distribution in the positive phase.

From the result of LIF measurement with the 4-mm bore tube at the same axial position using similar procedure to that explained in section 3.3, the radial distribution of relative $N_2^+(X)$ density at its peak timing was derived with the assumption of uniform gas composition from the spatial distribution fo the measured LIF signal intensity along the x axis. The result obtained in the positive voltage phase is shown in Fig. 4.8. The density peaked at the radial position of 0.9 mm similarly to the He^m distribution shown in Fig. 4.5. However, another smaller peak (or plateau) appeared in the distribution of $N_2^+(X)$ density near the center of the plasma plume.
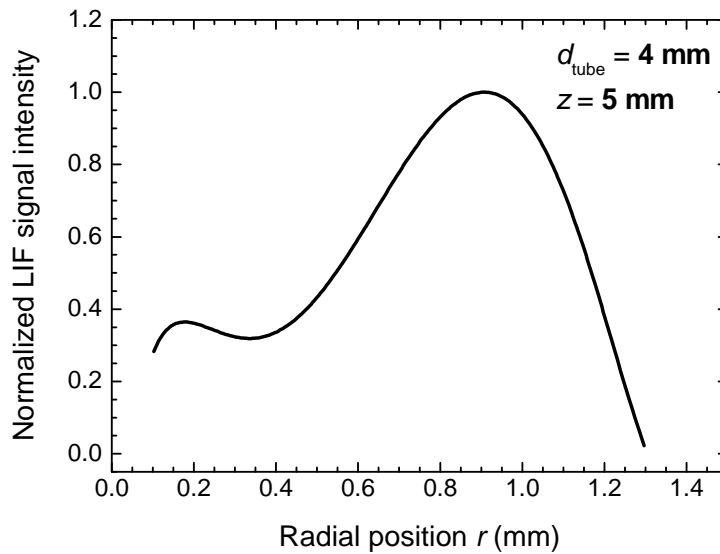
Figure 4.8   Radial distribution of normalized LIF signal intensity in positive voltage phase without grounded plate measured with 4-mm bore tube at $V_{0p} = 7.0$ kV and $z = 5$ mm at peak timing of $N_2^+(X)$ density.

4.3.3   Dependence of He^m density on applied voltage amplitude

Figure 4.9(a) shows temporal evolutions of the He^m absorption in the positive voltage phase measured at several values of V_{0p} with the 4-mm bore tube at a distance of $z = 5$ mm from the tube exit. The delay time of appearance of the absorption decreased with the increase of peak amplitude of the applied voltage, while the peak absorption changed little. On the other hand, in the negative phase shown in Fig. 4.9(b), it should be noted that there was a threshold of the peak value V_{0p} for the appearance of the plasma plume. When V_{0p} became larger than 6 kV, the plume appeared outside the nozzle, but the He^m absorption was strongly dependent on the peak applied voltage.

The temporal evolutions of He^m absorption with the same tube at distances of $z = 1, 3, 5,$
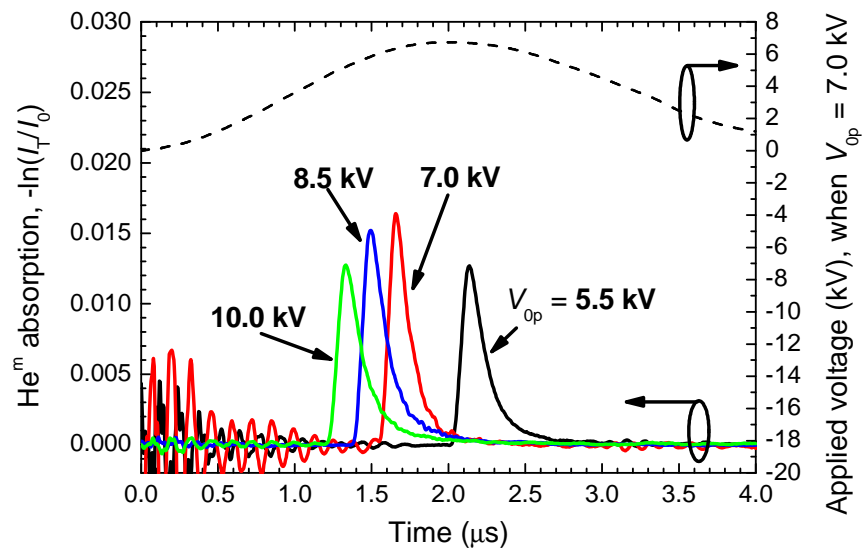
(a)
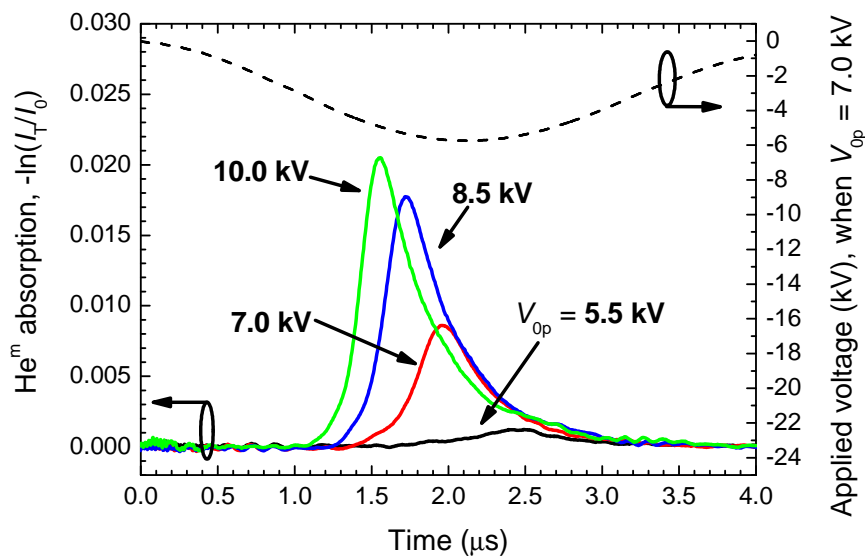
(b)

Figure 4.9   Temporal evolutions of He^m absorption in (a) positive voltage phase and (b) negative phase without grounded plate measured with 4-mm bore tube at z = 5 mm together with applied voltage waveform (V_{0p} are shown in figure).
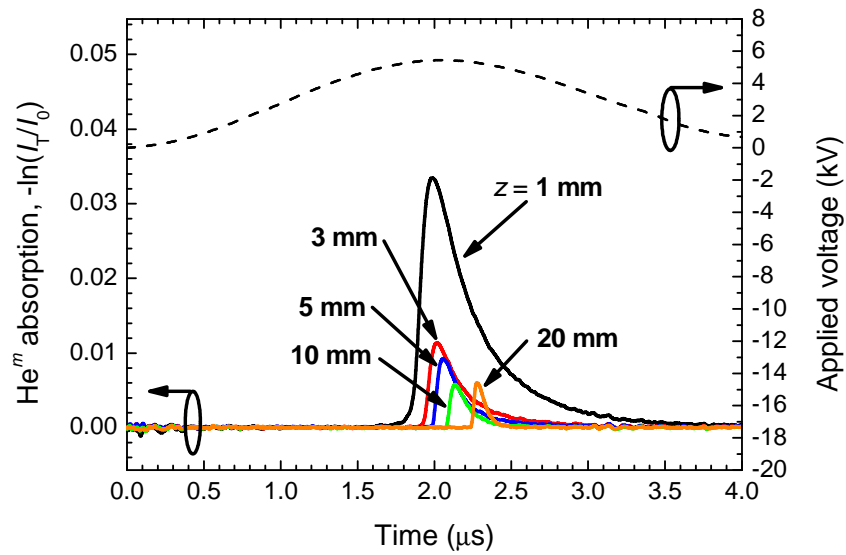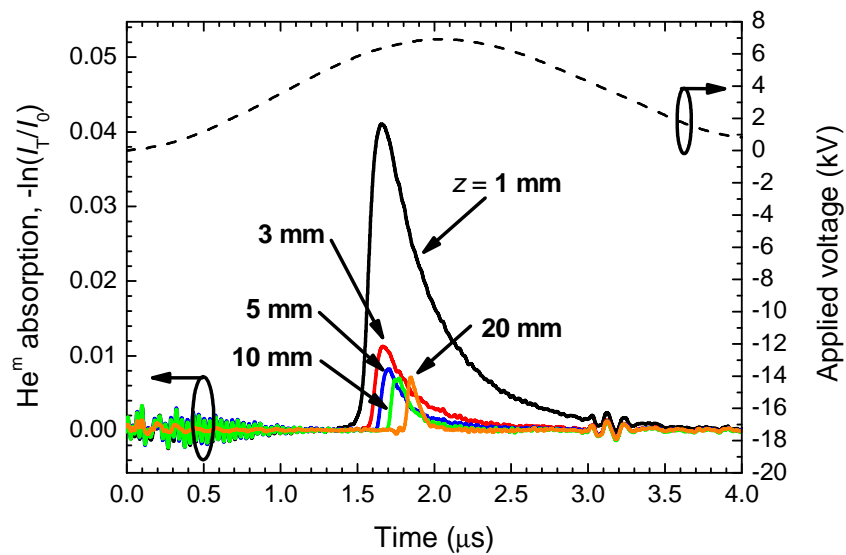
(a)

(b)

Figure 4.10   Temporal evolutions of He^m absorption in positive voltage phase without grounded plate measured with 4-mm bore tube at several axial positions; $z = 1, 3, 5, 10$, and 20 mm, at two values of peak applied voltage; (a) $V_{0p} = 5.5$ kV and (b) $V_{0p} = 7.0$ kV.

10, and 20 mm from the tube exit were also measured in the positive voltage phase. The measurement conditions of the applied voltage were two different peak voltages at $V_{0p} = 5.5$ and 7.0 kV, as shown in Fig. 4.10(a) and 4.10(b), respectively. In both cases the ionization front was ejected from the tube exit at a velocity of approximately 20 km/s and gradually accelerated to over 50 km/s in each voltage condition as calculated from the difference in the delay time of appearance of the He^m absorption at each measurement point. This result indicates that the difference in the delay time of the peak appearances in Fig. 4.9(a) must be caused by the change of ignition timing and not due to the difference in the propagation speed.

In the negative voltage phase, as shown in Fig. 4.11, the temporal behaviors of He^m absorption were measured with the same tube at different locations of $z = 5$, 10, and 15 mm from the tube exit. The temporal distributions had slower rising speeds than that in the positive phase
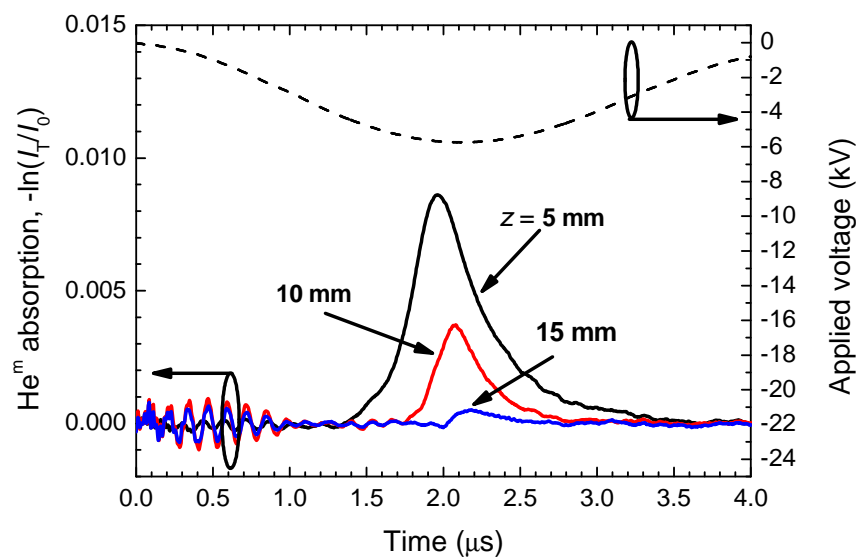

Figure 4.11 Temporal evolutions of He^m absorption in negative phase without grounded plate measured with 4-mm bore tube at $V_{0p} = 7.0$ kV at three axial positions; $z = 5$, 10, and 15 mm together with applied voltage waveform.

and overlapped with each other, so that the discharge was not propagating like a bullet as seen in the positive phase, although the plume front proceed at a speed of approximately 15 km/s. Thus, in the negative phase it was confirmed that a continuous plume of glow-like plasma was generated and the length depended also on the peak voltage (at 7.0 kV shown in Fig. 4.11, the plume decays drastically at z = 15 mm).

## 4.4   Influence of Grounded Plate on Discharge Behaviors

4.4.1   Spatiotemporal distribution of relative He^m density

Hereafter I will describe results in the situation where the grounded copper plate is placed at a distance of z = 20 mm from the tube exit to investigate the difference in both voltage phases. Figures 4.12(a) and 4.12(b) show the spatiotemporal evolutions of He^m absorption measured at V_{0p} = 6.0 kV. The grounded plate is located at the top of figure (20 mm) and the tube exit is at the bottom (0 mm). The measurement was done with the 2-mm bore glass tube by scanning the laser beam (directed through the y axis) with a step of 1 mm along the z axis between 1 and 19 mm from the tube exit.

  From the results in the positive voltage phase, shown in Fig. 4.12(a), a He^m peak region initially propagated with a very high velocity of approximately 120 km/s. After the primary ionization front reaches the grounded plate, secondary discharge with a considerably higher density than that in the primary front was observed from the tube exit up to a distance of 14 mm propagating at a velocity of approximately 30 km/s. This discharge phenomenon is similar to a transient-glow discharge [4.16] observed in a single filamentary DBD. [4.17] Moreover, the high-density state of He^m atoms lasted longer as the measurement point approached toward the
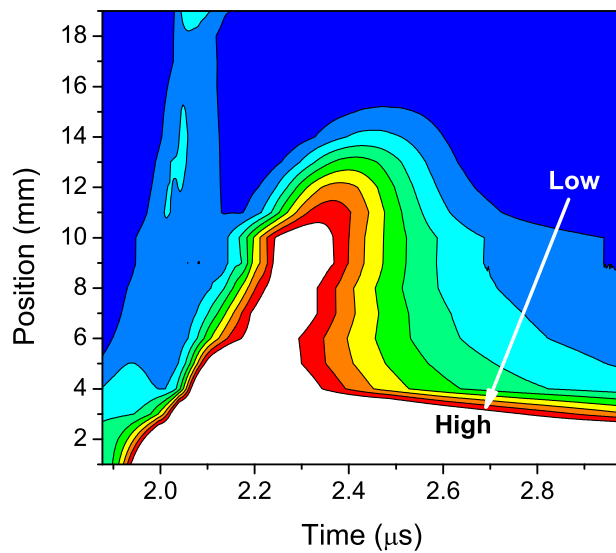
(a)
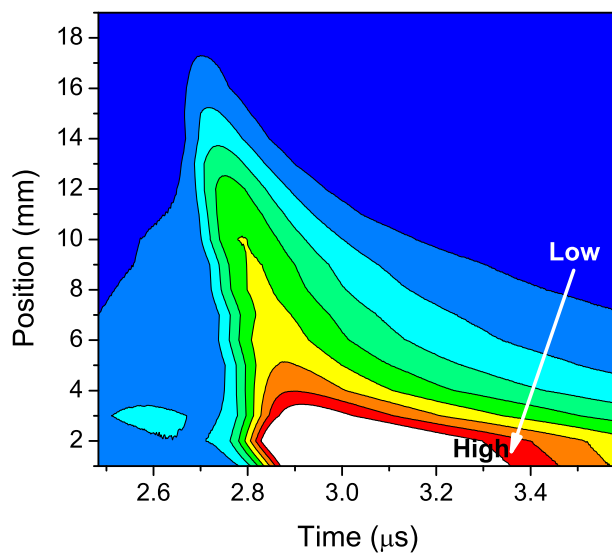
(b)

Figure 4.12   Spatiotemporal distributions of He^m absorption in contour diagram (with color code) in (a) positive voltage phase and (b) negative phase with grounded plate measured with V_{0p} = 6.0 kV and d_{tube} = 2 mm over axial area from z = 1 mm to 19 mm. Note difference in scale that in (a) white region indicates overflowed region with absorption more than 0.1, while in (b) it indicates more than 0.3.

tube exit. This may be due to the lower contaminating fraction of ambient air into the He gas flow decreasing the quenching effect of He^m atoms.

In the negative voltage phase shown in Fig. 4.12(b), however, the primary ionization front could not be noticed, although a broad distribution of He^m density was seen before 2.7 μs. It may be due to the lower value of V_{0p}. In this measurement V_{0p} = 6.0 kV, which is near the threshold of plume appearance in the negative phase measured without the grounded plate. After 2.7 μs the front of the high-density region propagates from the grounded copper plate toward the tube exit at a speed of approximately 100 km/s, which is much faster than the secondary ionization front at the positive phase. It looks like that the distribution of He^m density fills the inter-electrode gap in a short time, and then shrinks from the copper-plate side according to the formation of glow-like discharge.

4.4.2   Spatiotemporal distribution of relative N_2^+ density

Figures 4.13(a) and 4.13(b) show the spatiotemporal distributions of LIF fluorescence signal intensity measured by the LIF method in both positive and negative voltage phases. The signal is approximately proportional to the relative $N_2^+(X)$ density distribution as in the case of He^m absorption shown in Figs. 4.12(a) and 4.12(b). The 2-mm bore glass tube was used, and the LIF measurement was at distances of z = 1, 5, 10, 15, and 19 mm from the tube exit (5 axial positions) with V_{0p} = 6.0 kV.

From the results in the positive voltage phase shown in Fig. 4.13(a), the primary and secondary propagation of high-density region of the $N_2^+(X)$ ions could be observed similar to the He^m absorption. However, there was no noticeable presence of the $N_2^+(X)$ ions within a distance from z = 1 to 5 mm. This is because that in this region the He laminar flow is not contaminated
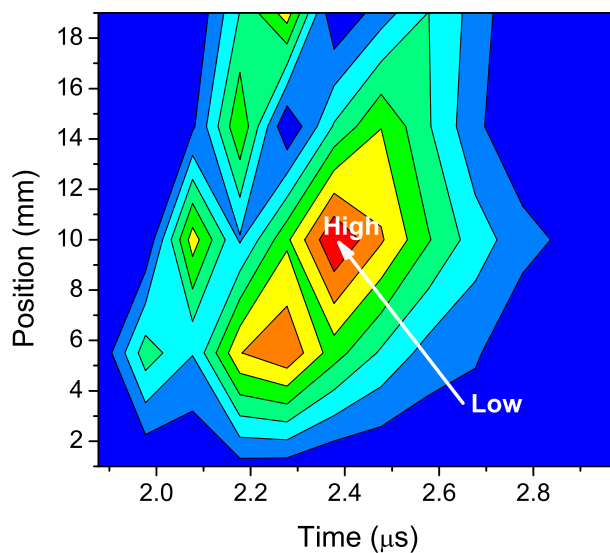
(a)
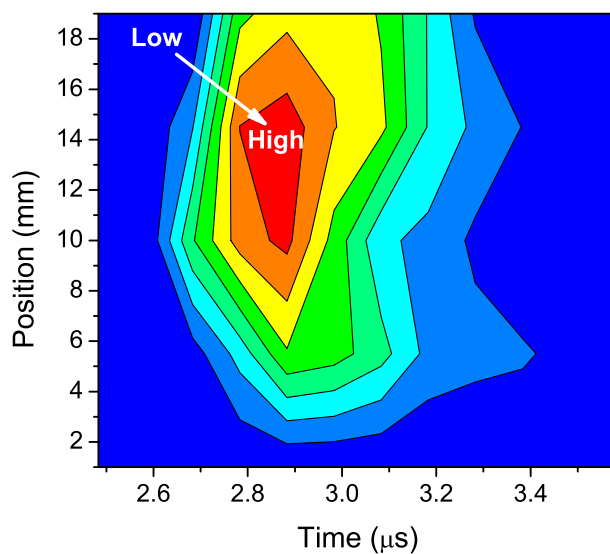
(b)

Figure 4.13   Spatiotemporal distributions of relative LIF signal intensity in contour diagram (with color code) in (a) positive voltage phase and (b) negative phase with grounded plate measured with V_{0p} = 6.0 kV and d_{tube} = 2 mm over axial area from z = 1 mm to 19 mm (actual measurement was done at five axial points; z = 1, 5, 10, 15, and 19 mm).

by the N_2 molecules in ambient air. The high-density region of $N_2^+(X)$ ions in the secondary propagation shifted toward the grounded plate in comparison with the measurement results of He^m density shown in Fig. 4.12(a).

In the negative voltage phase shown in Fig. 4.13(b), there was no propagation of the high-density region of $N_2^+(X)$ ions from the grounded plate in contrast to the LAS measurement. A more uniform and larger distribution of $N_2^+(X)$ ions were observed than that in the positive phase over the measurement points from $z = 10$ to 19 mm. It is noted here that the solid angle of measured LIF signal at the measurement point of $z = 19$ mm becomes smaller, because the grounded plate partially blocked the fluorescence light. Taking into account of this solid angle effect in the collection optics, the LIF signal intensity at 19 mm should be considerably greater, indicating that a large amount of the $N_2^+(X)$ ions exists in front of the grounded plate.

4.4.3 Temporal evolution of N_2 emission intensities near Cu plate

For the investigation of ionization mechanisms in the vicinity of the grounded copper plate, the temporal evolutions of emission intensities was measured with below 30-ns temporal resolution at a distance of $z = 19$ mm from the tube exit, using the 2-mm bore glass tube. The signals of N_2 (C-B) (0-0) band and N_2^+ (B-X) (0-0) band measured in both positive and negative voltage phases with $V_{0p} = 6.0$ kV are shown in Figs. 4.14(a) and 4.14(b), respectively. The first emission peak of N_2 (C-B) in the positive phase was taken as the reference (unity intensity) and other emission intensities were shown in the relative scale for comparison. In the positive phase, both primary emission peaks had the same temporal behavior, while a large secondary peak was observed only for the N_2 (C-B) emission. In the negative phase, the primary and secondary peaks appeared with a smaller time difference, compared to the positive phase, overlapping with
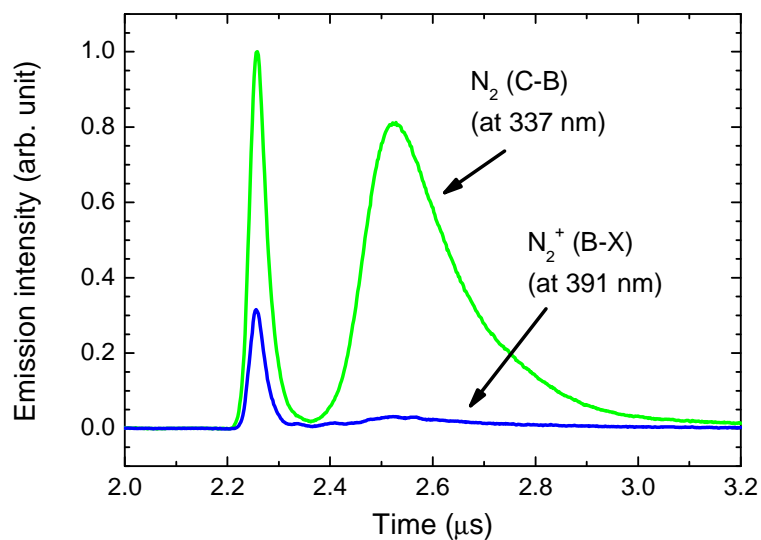
(a)
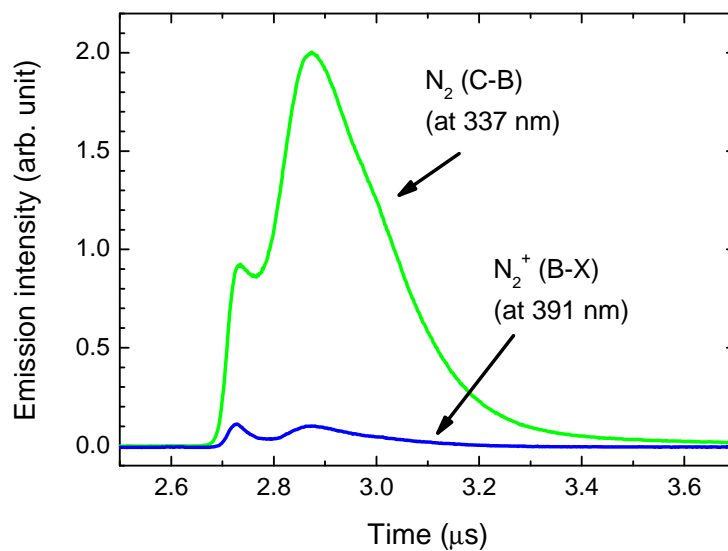
(b)

Figure 4.14 Temporal evolutions of emission intensities of N_2 (C-B) (0-0) band (337 nm) and N_2^+ (B-X) (0-0) band (391 nm) in (a) positive voltage phase and (b) negative phase with grounded plate measured with 2-mm bore tube at $V_{0p} = 6.0$ kV and $z = 19$ mm.

each other. The second peak of the N$_2$ (C-B) emission became even larger than the first peak
and the N$_2^+$ (B-X) emission intensity was much smaller than the N$_2$ (C-B) intensity.

4.4.4   Radial distribution of absolute He^m density

Figure 4.15 shows the radial distributions of absolute He^m density measured in both voltage
phases with V_{0p} = 6.0 kV using the 4-mm bore glass tube and at a distance of z = 5 mm from
the tube exit. Those data correspond to the peak He^m density, at 1.87 μs (positive phase) and
2.08 μs (negative phase) after the rise timing of applied voltage. In the positive phase, the
distribution represents the situation of transient-glow discharge in the secondary discharge after
the primary ionization-front propagation. The radial shape in this phase had a hollow profile
similar to that measured without the grounded plate. On the contrary, in the negative phase, it
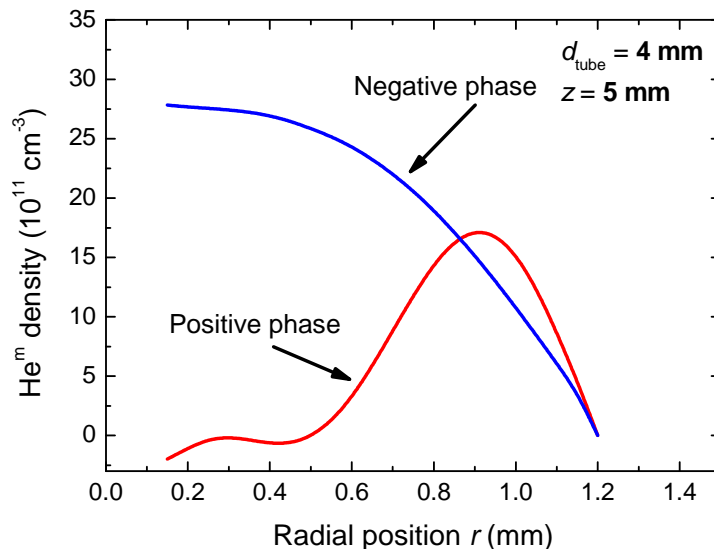
Figure 4.15   Radial distributions of absolute He^m density in both voltage phases with
grounded plate measured with 4-mm bore tube at V_{0p} = 6.0 kV and z = 5 mm at respective
timing of 1.87 μs (positive phase) and 2.08 μs (negative phase) after rise timing of applied
voltage.

had a center-peaked profile which was even higher than that in the positive phase.

4.5 Discussions on Discharge Mechanisms in Jet-Type DBD

4.5.1 Operated without grounded plate

In the operation mode without the grounded copper plate, there was a large difference in the radial distributions of He^m density measured between positive and negative voltage phases as shown in Figs. 4.5 and 4.7. For the ease of comparison, the radial distributions measured at a distance of $z = 5$ mm are re-plotted in Fig. 4.16, together with the relative $N_2^+(X)$ density given in Fig. 4.8. Both the distributions of He^m and $N_2^+(X)$ in the positive phase had ring shapes, except for the appearance of a smaller peak in the $N_2^+(X)$ distribution near the center

Figure 4.16   Radial distributions of He^m absorption in both voltage phases and LIF signal intensity of N_2^+ in positive voltage phase without grounded plate ($V_{0p} = 7.0$ kV, $d_{tube} = 4$ mm, and $z = 5$ mm) redrawn from results shown in Figs. 4.5, 4.7, and 4.8.

(this reason will be explained in the following paragraph). The reason for the formation of these ring-shaped distributi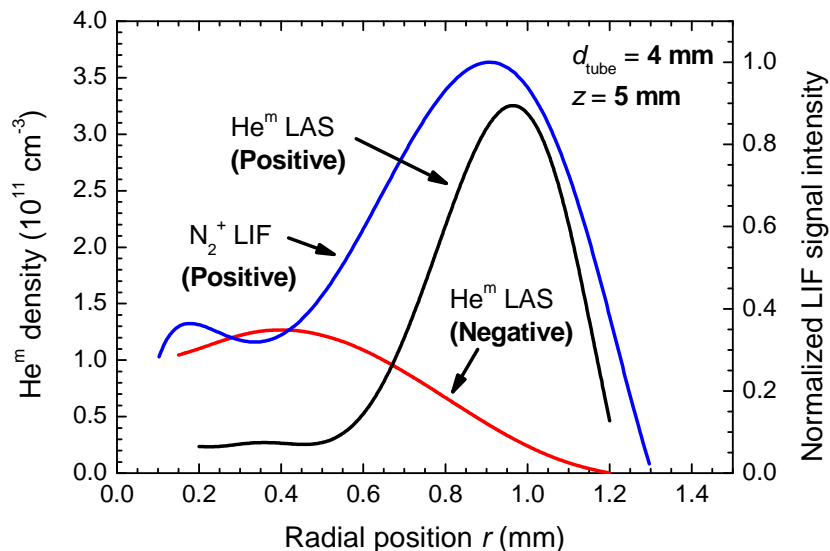ons in the plasma plume can be attributed to the breakdown mechanism of the coaxial DBD jet discussed in the previous chapter 3. In this phase, the breakdown is caused by the localized high electric field on the inner surface of the tube at the downstream edge of front-side powered electrode, where the high field is formed by the superposition of external voltage and positive space charge accumulated on the surface in the preceding half-cycle of applied voltage.

Comparing the radial distribution of relative $N_2^+(X)$ density with the He^m distribution in the positive voltage phase, the ring thickness of the $N_2^+(X)$ density is a little broader, and an additional small peak (or plateau) appears near the center of the plume. This is because that the $N_2^+(X)$ ions tend to diffuse toward the center of He gas flow where the quenching of $N_2^+(X)$ ions is less effective, while at the outer edge of the plume $N_2^+(X)$ ions are quenched by collisions with N_2 and O_2 molecules resulting in the production of N_4^+ and O_2^+ ions. [4.18, 19]

On the other hand, the radial distribution of He^m density in the negative voltage phase as shown in Fig. 4.16, the peak density became smaller than that in the positive phase by a factor of one-third, and the peak position was located closer to the central axis of the plume. Also from the result shown in Fig. 4.11, glow-like continuous plasma region was observed, starting from the tube exit and elongating up to the plume front along the gas flow. This glow-like discharge is just like a negative glow region observed in a negative corona discharge. [4.20] In this phase ambient electrons are directly accelerated toward the negatively biased electrode, and during the electron transport the glow-like plasma is generated along the He gas flow. The reason for the He^m distribution taking the center-peaked shape is probably attributed to the hollow-shaped temporal cathode, in which the negative glow region concentrates along the center of the bore.

4.5.2   Operated with grounded plate

It was noted in the jet-type DBD with the grounded plate that the propagation speed of primary ionization front in the positive voltage phase became higher due to the increase of electric field strength with the actual cathode placed at a finite distance. Comparing the results in both positive and negative voltage phases, the observed discharge behaviors were very different with each other, especially in the earlier time. In the positive phase, the secondary transient-glow discharge was observed after the primary front propagation, as shown in Figs. 4.12(a) and 4.13(a). However, in the negative phase, there appeared a single peak in the He^m absorption and the LIF signal intensity as seen in Figs. 4.12(b) and 4.13(b) at a lower applied voltage (V_{0p} = 6.0 kV), and the transient-glow rapidly expanded between the negatively biased electrode and the grounded metallic plate. In contrast to the case without the grounded plate, the peak density of He^m atoms in the negative phase became larger by approximately three times than that in the positive phase for the case with the grounded plate (see the caption of Fig. 4.12). This indicates the formation of a negative glow-region near the negatively biased ring-electrode the formation of which was experimentally confirmed in the parallel-plate DBD as explained in chapter 2.

The radial distributions of He^m density measured in both positive and negative voltage phases, shown in Fig. 4.15, had the peak values on the order of 10^{12} cm^{-3}. These values were much larger than that measured without the grounded plate, shown in Fig. 4.16. This is because of the presence of transient-glow discharge between the electrodes after the initial ionization-front propagation. The reason for the different radial distributions can be explained in the same manner as in the coaxial DBD jet. In the positive phase, the secondary discharge follows the same pathway as the primary ionization front, taking the ring-shaped distribution near the tube
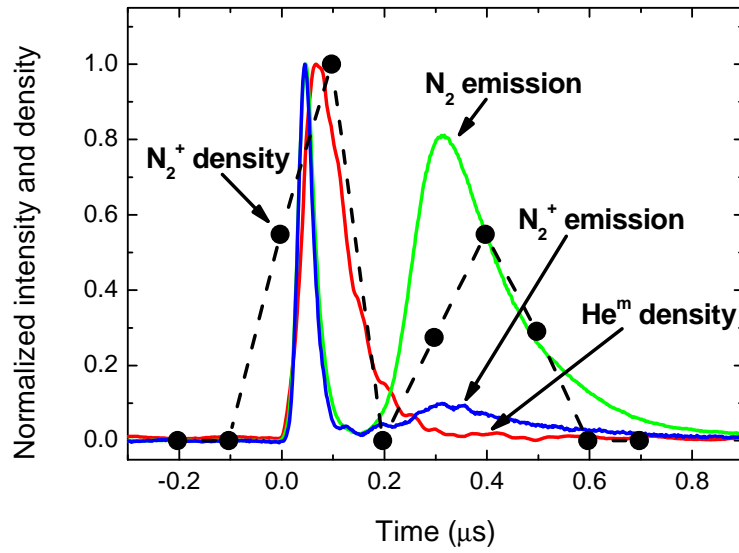
(a)
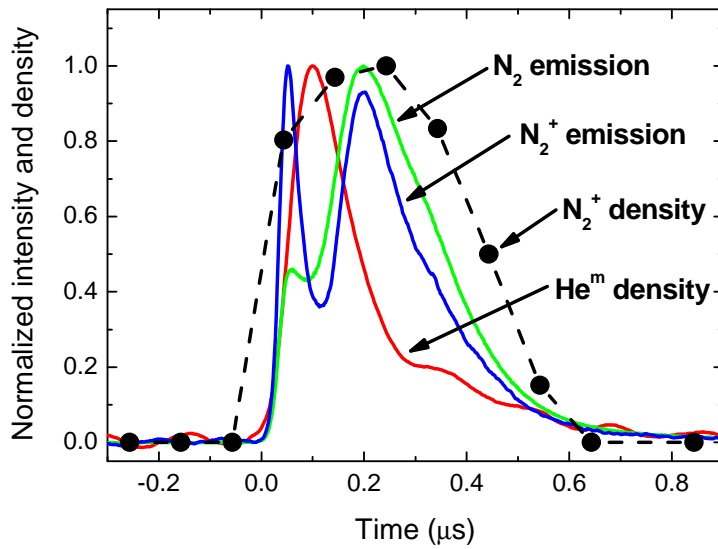
(b)

Figure 4.17   Temporal evolutions of normalized densities of He^m atoms and $N_2^+(X)$ ions and emission intensities of N_2 (C-B) and N_2^+ (B-X) in (a) positive voltage phase and (b) negative phase with grounded plate measured with 2-mm bore tube at $V_{0p} = 6.0$ kV and $z = 19$ mm.

exit, while in the negative phase the glow-like discharge occurs between the electrodes where the negatively biased electrode is working as the hollow ring cathode to make the discharge concentrated along the central axis.

It is often observed in the actual material processing condition that the emission intensity in the jet-type DBD is enhanced near the conductive substrate. Therefore, focused investigation on the discharge mechanisms near the grounded copper plate is done from the results of LIF and OES measurements. Figs. 4.17(a) and 4.17(b) summarize the temporal evolutions of He^m absorption (from Fig. 4.12), relative $N_2^+(X)$ density (from Fig. 4.13) together with the N_2 (C-B) and N_2^+ (B-X) emission intensities (from Fig. 4.14) measured at a distance of 1 mm from the grounded plate (z = 19 mm). In these figures, the time origin is set at the rise timing of all data to compare the temporal evolutions eliminating the slight differences of discharge conditions in each measurement except for the N_2^+ LIF data in which the temporal resolution is poorer due to the finite measurement points. All data were normalized by their peak values. In the positive phase, as shown in Fig. 4.17(a), all data had the larger values in the first peak due to the primary ionization-front propagation towards the copper plate, while the secondary discharge does not completely reach the plate as already explained in Figs. 4.12(a) and 4.13(a). The second peaks in the N_2 (C-B) emission and the N_2^+ density signals are larger than those of the He^m absorption and the N_2^+ emission signals. This suggest that the ionization and excitation in the transient-glow discharge are occurring near the copper plate with less energetic electrons than that having enough energy to excite He atoms in the primary ionization-front propagation.

In the negative phase data shown in Fig. 4.17(b), there appeared two peaks in the temporal evolutions of N_2 (C-B) and N_2^+ (B-X) emission intensities as in the case in the positive phase, but the interval time duration decreased and the ratio of second peak amplitude to the first peak

increased. Two peaks were also noticed in the He^m absorption, but the second peak was much smaller than the first peak. In the N_2^+ density the two peaks merged together and its peak timing coincided with the secondary peaks of the N_2 (C-B) and N_2^+ (B-X) emissions. A comparison between these emission signals with Fig. 4.14(b), showed that the relative emission intensity of N_2 (C-B) was much larger than N_2^+ (B-X). These results indicate that a strong ionization occurs near the grounded copper plate working as the temporal anode in the negative phase, and a large amount of N_2^+ ions are produced not by the Penning process but by the direct electron-impact ionization process. The intensity ratio of N_2 (C-B) to N_2^+ (B-X) emissions also suggests lower reduced electric field in this discharge condition.

4.6   Summary

In summary, discharge mechanisms in the jet-type DBD in two different operation modes with and without conductive substrate at a finite distance, were investigated mainly by the LAS and LIF measurements.

From the results of the LAS measurement without the grounded plate, it was revealed that, in the positive voltage phase, the radial distribution of He^m density was ring shaped, and its peak density was nearly constant even when the peak value of the applied voltage was changed. On the other hand, in the negative phase, the He^m density was observed only at higher applied voltage with a threshold around 6 kV, and the radial distribution tended to take a center-peaked shape. The discharge mechanisms in the condition without the gruonded plate in the positive phase could be explained by the propagation of ionization front having a good agreement with conclusions of the previous chapter 3. In the negative phase, the discharge also proceeded forward from the negatively biased electrode but a continuous plume was seen similar to the

transient-streamer in negative corona discharge.

In the jet-type DBD operated with the grounded plate, transient-glow discharges after the primary discharge-channel formation were observed in both voltage phases and the peak densities of excited species became much larger than those without the plate. The ionization mechanisms near the grounded copper plate placed at 20-mm distance from the tube exit were also investigated simulating the situation of actual material processes. The density of $N_2^+(X)$ ions became considerably larger in the negative phase near the grounded plate, while the He^m density was almost absent. Thus, it was concluded that the ionization mechanism of N_2 molecules in the negative phase was not dominated by the Penning ionization process but by the direct electron-impact ionization process. These results are significantly different from the results obtained in the coaxial DBD jet operated without a substrate.

References

[4.1] F. Massines, P. Segur, N. Gherardi, C. Khamphan, and A. Ricard: Surf. Coating Technol. **174-175** (2003) 8.

[4.2] O. Sakai, T. Sakaguchi, Y. Ito, and K. Tachibana: Plasma Phys. Control. Fusion **47** (2005) B617.

[4.3] Y. Ito, K. Urabe, M. Kubo, and K. Tachibana: Proc. 18th Int. Symp. Plasma Chemistry, 2007, p. 173.

[4.4] K. Urabe, Y. Ito, K. Tachibana, and B. N. Ganguly: Appl. Phys. Express **1** (2008) 066004.

[4.5] J. L. Walsh, J. J. Shi, and M. G. Kong: Appl. Phys. Lett. **88** (2006) 171501.

[4.6] Q. Nie, C. Ren, D. Wang, S. Li, and J. Zhang: Appl. Phys. Lett. **90** (2007) 221504.

[4.7] T. Somekawa, T. Shirafuji, O. Sakai, K. Tachibana, and K. Matsunaga: J. Phys. D **97** (2005) 123301.

[4.8] S. V. Patankar and D. B. Spalding: Int. J. Heat Mass Transfer **15** (1972) 1787.

[4.9] K. Tachibana, Y. Kishimoto, and O. Sakai: J. Appl. Phys. **97** (2005) 123301.

[4.10] X. Lu and M. Laroussi: J. Appl. Phys. **100** (2006) 063302.

[4.11] K. Kitano and M. Hamaguchi: Proc. 18th Int. Symp. Plasma Chemistry, 2007, p. 211.

[4.12] J. Kedzierski, J. Engemann, M. Teschke, and D. Kerzec: Solid State Phenom. **107** (2005) 119.

[4.13] B. L. Sands, B. N. Ganguly, and K. Tachibana: IEEE Trans. Plasma Sci. **36** (2008) 956.

[4.14] K. Urabe, T. Morita, K. Tachibana, and B. N. Ganguly: J. Phys. D **43** (2010) 095201.

[4.15] N. Mericam-Bourdet, M. Laroussi, and E. Karakas: J. Phys. D **42** (2009) 055207.

[4.16] E. Marode: J. Appl. Phys. **46** (1975) 2005.

[4.17] K. V. Kozlov, H.-E. Wagner, R. Brandenburg, and P. Michel: J. Phys. D **34** (2001) 3164.

[4.18] K Becker, M Schmidt, A. A. Viggiano, R. Dressler, and S. Williams: in *Non-Equilibrium Air Plasma at Atmospheric Pressure*, eds. K. H. Becker, U. Kogelshatz, K. H. Schoenbach, and R. J. Barker (IoP Publishing, Philadelphia, 2005).

[4.19] A. Kossyi, A. Y. Kostinsky, A. A. Matveyev, and V. P. Silakov: Plasma Souces Sci. Technol. **1** (1992) 207.

[4.20] D. Wang, M. Jikuya, S. Yoshida, T. Namihira, S. Katsuki, and H. Akiyama: IEEE Trans. Plasma Sci. **35** (2007) 1098.

Chapter 5

Glow-Like Dielectric Barrier Discharges in Ar Gas Flow[†]

5.1 Introduction

Among various types of dielectric barrier discharge (DBD), their discharge schemes are typically classified in glow-like or filamentary modes. [5.1, 2] The glow-like discharge mode has been observed in helium (He) gas, [5.3, 4] and several studies have been performed on argon (Ar) plasmas stabilized by addition of organic or inorganic molecules. [5.5, 6] On the other hand, the filamentary mode appears in atmospheric air, pure Ar gas, and so forth. [5.2, 7] For the application of the DBDs to material processes, the glow-like DBDs using dilute He gas have been widely developed to satisfy the requirement of temporally stable and spatially homogeneous plasmas.

In this chapter, a transition-like phenomenon in the DBD using Ar gas with a small fraction of molecules is introduced. The discharge-mode transition was observed in a jet-type DBD, which was discussed in the previous chapter 4, and in a coaxial DBD inside a glass tube. Acetone (CH_3COCH_3: C_3H_6O) and ammonia (NH_3) molecules were chosen as the additive molecules following previous reports which suggested the glow-like discharge generation in a

---

[†]Contents about discharges in Ar/acetone mixed flow in this Chapter are altered form of a published paper: K. Urabe, K. Yamada, and O. Sakai, "*Discharge-Mode Transition in Jet-Type Dielectric Barrier Discharge Using Argon/Acetone Gas Flow Ignited by Small Helium Plasma Jet*", Japanese Journal of Applied Physics, **50** (2011) 116002.

parallel-plate DBD. [5.5, 6] In order to clarify the stabilization mechanisms, several simultane-ous discontinuous changes in discharge parameters were analyzed mainly by an optical emission spectroscopy (OES) method, when the added molecular fractions were changed gradually. The discharge-mode transition showed strong nonlinear dependence on the molecular fraction, and this nonlinear transition is one of the particular phenomena in the high-pressure plasmas, since their characteristic lengths in the reaction space and/or the diffusion length are comparable to or much smaller than the discharge region owing to the frequent collision at the elevated pressure.

   In addition to the basic study of the glow-like DBDs focusing at the discharge region, poten-tials of those plasma sources to be applied to novel material processes are investigated through trial experiments. In the jet-type DBD operated in the Ar/acetone mixed flow, deposited films of carbon-based materials on the conductive plate were observed, and their microscopic surface morphologies varied significantly around the discharge-mode transition. Also, using the coaxial DBD in the Ar/NH$_3$ mixed flow, potentials of the plasma source to be applied to reduction and nitrization processes are confirmed by detection of hydrazine (H$_2$NNH$_2$: N$_2$H$_4$), NH, and NO molecules.

5.2   Jet-Type DBD in Ar/Acetone Mixed Flow

5.2.1   Experimental procedure

Figure 5.1 shows a schematic diagram of the jet-type DBD in a crossed-flow configuration, with *xyz* axes included to explain the observation and measurement directions. A 45°-tilted pure He gas flow with a flow rate of 100 mL/min and a vertical Ar/acetone mixed flow with a flow rate from 5.60 to 5.70 L/min were fed into two glass tubes. The axes of these gas flows were both
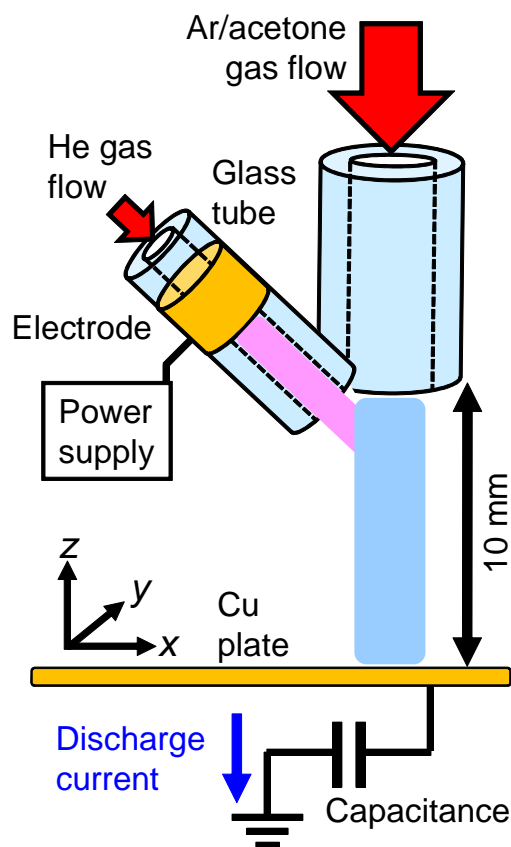
Figure 5.1   Schematic diagram of jet-type DBD using two crossed gas flows of pure He and Ar/acetone mixture, together with *xyz* axes to explain observation and measurement directions.

in the *xz* plane. The inner and outer diameters of the two glass tubes were 0.8 and 2.0 mm

for the tilted He flow, and 3.4 and 5.0 mm for the vertical Ar/acetone flow, respectively. The

tilted He flow was used as a small coaxial DBD jet with a copper-ring powered electrode, and

the coaxial DBD jet was sprayed in the vicinity of the vertical-tube exit to generate the plasma

in the Ar/acetone flow. A copper (Cu) plate, which was connected to the ground with a series

capacitance of 50 pF to limit the discharge current and improve the stability of the jet-type

DBD, [5.8] was placed 10 mm from the vertical-tube exit. The entire discharge setup was put

in a handmade box composed of transparent plastic and Bakelite plates, in order to avoid the

leakage of acetone molecules into the atmosphere.

A small amount of acetone vapor was added to the Ar gas flow by a bubbling method of liquid acetone. The Ar flow was divided into two paths, since the acetone-vapor ratio became too large to generate a stable discharge when all the Ar gas flow was passed through the liquid acetone. Using two mass flow controllers, the main Ar flow rate was fixed at 5.60 L/min and the bubbling Ar flow rate was changed from 0 to 100 mL/min to control the acetone-vapor ratio. To avoid fluctuation of the acetone-vapor ratio due to the change of vapor pressure, the temperature of liquid acetone was kept at 20.0 °C by a Peltier-device controller. The absolute value of acetone-vapor ratio in the Ar flow was monitored using a Fourier-transform infrared spectroscopy (FT-IR) method and a reported absorption coefficient of the acetone vapor at 1738 cm^{-1}. [5.9]

A bipolar impulse power supply was used to ignite the discharge between the powered electrode and the Cu plate, and the peak value and repetition rate of its output voltage were fixed at 6.0 kV and 5.0 kHz, respectively. [5.10, 11] Images of the electrode configuration and discharge emissions of the jet-type DBD were recorded along the *y* axis by a digital camera placed outside the plastic box. A high-voltage probe and a Rogowski coil connected to a digital oscilloscope were used to measure the temporal evolutions of the applied voltage and the discharge current flowing into the Cu plate.

5.2.2   Discharge transition from filamentary and glow-like modes

In order to distinguish the discharge modes of the jet-type DBD in the Ar/acetone flow, photographs of the discharge emission were taken using the digital camera placed along the *y* axis in Fig. 5.1 while increasing the bubbling Ar flow rate. Figure 5.2(a) shows the setup of the glass tubes and the Cu plate, and Figs. 5.2(b) and 5.2(c) show discharge images taken when the

bubbling Ar flow rates were 20 and 80 mL/min, respectively. The absolute acetone-vapor ratios corresponding to the conditions of Figs. 5.2(b) and 5.2(c) were 0.15 and 0.55%, respectively.

For the lower acetone-vapor ratio (Fig. 5.2(b)), the rapid movement of thin bright filaments was observed in the Ar/acetone flow, and their positions were localized on one side of the Ar/acetone flow near the crossing point of the two gas flows. This temporally unstable filamentary discharge mode observed at the lower acetone-vapor ratio is called a "filament mode" hereafter. In the image taken when the bubbling Ar flow rate was 80 mL/min (Fig. 5.2(c)), a glow-like homogeneous emission was observed without any filament. In this discharge mode, called a "glow mode" hereafter, the emission diffused to the whole region of the Ar/acetone flow near the Cu plate from the crossing point of the two flows. Emissive spots having a similar green color to that in the filament mode were observed in the vicinity of the Cu plate. The one-sided spread of the discharge was probably due to the short transport length of electrons and/or
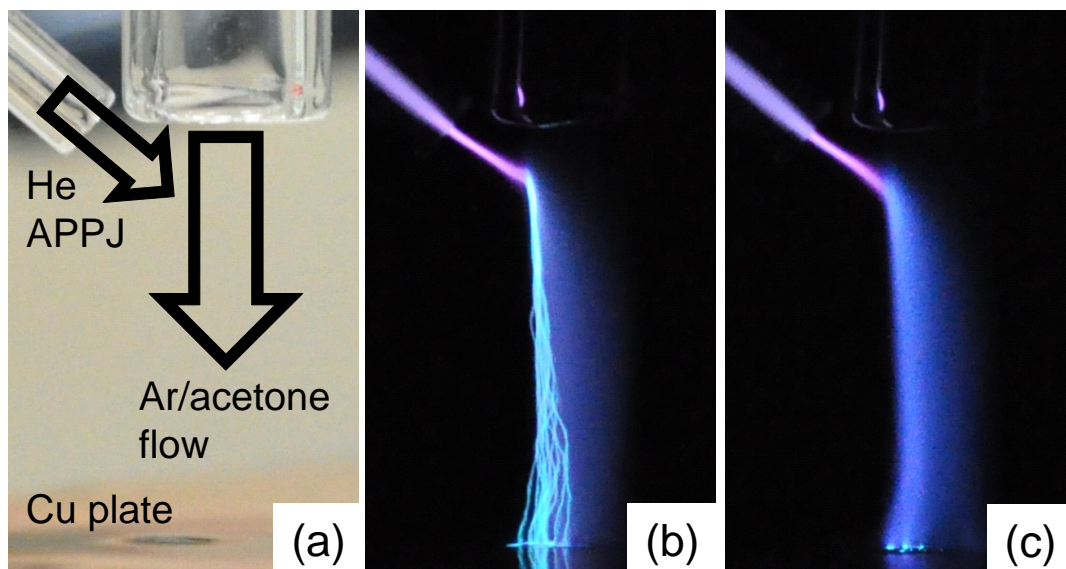

Figure 5.2 Photographs of discharge emission in jet-type DBD in Ar/acetone flow with small He coaxial DBD jet, together with (a) setup. Acetone-vapor ratios are (b) 0.15% (in filament mode) and (c) 0.55% (in glow mode). Shutter speed of digital camera is 1/160 s in (b) and (c).

Ar metastable atoms in such a high-pressure discharge, although electrons are reasonably movable compared with the other neutral particles since the drift term is dominant in their transport phenomena, which leads to the finding that electrons are more important in such a situation. Also, the non-uniform electric field distribution in the Ar/acetone flow formed by the electrode of the He coaxial DBD jet might have affected this gradual change in the visible emission.

The waveforms of the discharge current flowing into the Cu plate were measured in order to compare the stability and temporal behavior of the jet-type DBD in each discharge mode. Figure 5.3 shows the temporal evolutions of the discharge current with the applied voltage in the positive-voltage phase, measured five times without averaging under the same discharge conditions as Fig. 5.2(a) and (b). The time origin is set at the rise timing of the applied voltage.

Comparing the current waveforms in the filament mode (Fig. 5.3(a)), there are fluctuations of the rising speed and the peak value (from 80 to 110 mA) after the ignition at the same timing of approximately 1.30 μs. This result indicates that the discharge in the filament mode has temporally unstable characteristics similar to reported phenomena in a filamentary DBD [5.12] and that the additional He coaxial DBD jet contributes to discharge stability by maintaining a constant ignition timing. On the other hand, in the glow mode shown in Fig. 5.3(b), the peak current was approximately one-third smaller than that in the filament mode, the pulse duration was longer, and there was little difference in the current waveforms in the main current pulse starting around 1.2 μs. From these current waveforms, as well as the observation results, the discharge stability in the glow mode was much greater than that in the filament mode. There was also a current pulse at approximately 1.15 μs having a much smaller peak than the main pulse. This result suggests that the discharge phenomena in the glow mode are composed of propagating ionization front and a transient glow discharge, and the small peak indicates the
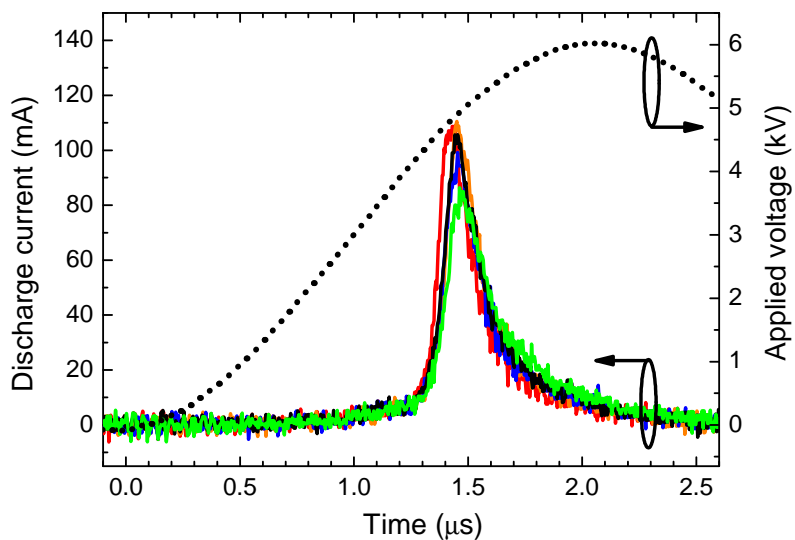
(a)
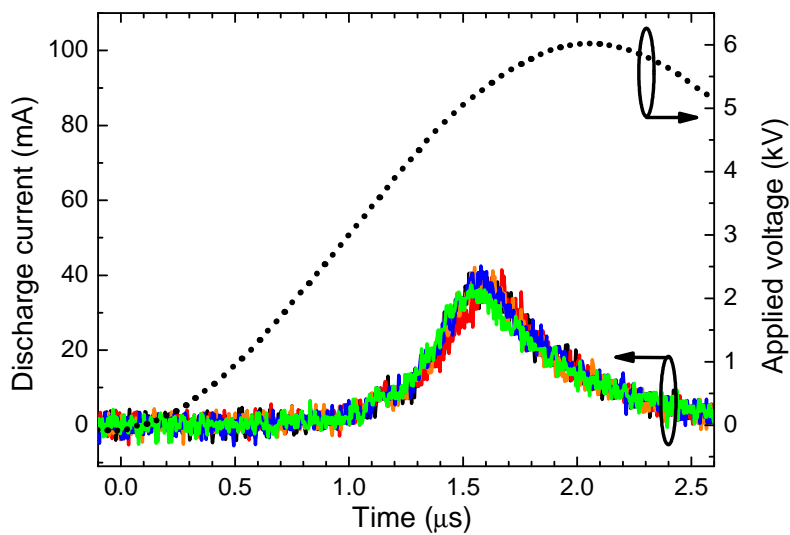
(b)

Figure 5.3   Temporal evolutions of discharge current flowing into Cu plate, measured five times without averaging under same condition. Acetone-vapor ratios are (a) 0.15% (in filament mode) and (b) 0.55% (in glow mode).

time when the ionization front reaches the Cu plate. These discharge mechanisms in the positive

phase of the applied voltage are similar to those for the jet-type DBD using only the He gas flow,

as previously discussed in chapter 4.

The temporally averaged emission spectra midway between the vertical-tube exit and the

Cu plate were measured by the OES method varying the bubbling Ar flow rate from 0 to 100

mL/min with a step of 5 mL/min. Figure 5.4 shows the optical emission spectra in the wave-

length range between 280 and 850 nm, measured under the same discharge conditions as shown
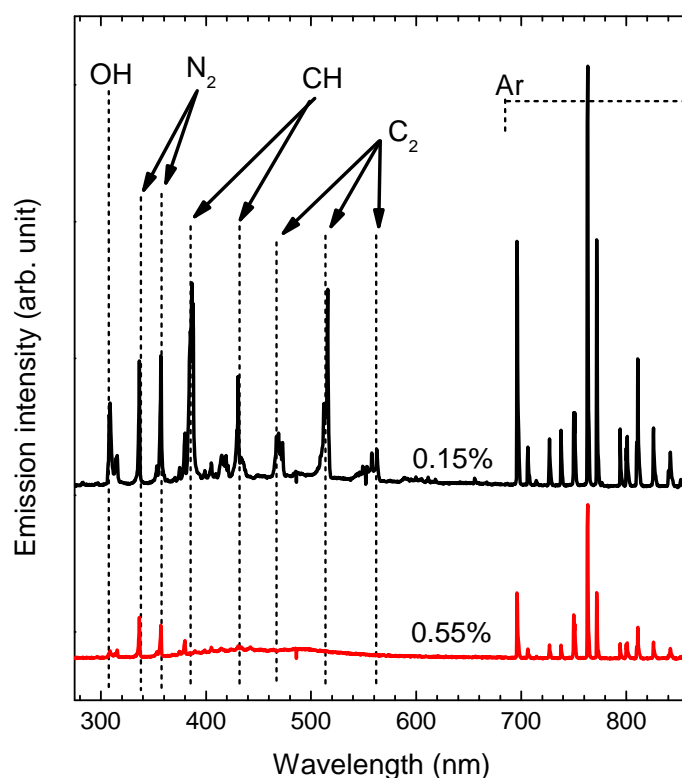

Figure 5.4   Optical emission spectra of jet-type DBD in wavelength range from 280 to 850
nm measured 5 mm from Cu plate. Acetone-vapor ratios are 0.15% (upper black line, in
filament mode) and 0.55% (lower red line, in glow mode).

in Fig. 5.2(a) and (b). In these spectra, the main emission components were identified as the OH $A^2\Sigma^+$-$X^2\Pi$ (0-0) band (at 309 nm), the N_2 $C^3\Pi_u$-$B^3\Pi_g$ (0-0) band (at 337 nm), the C_2 $A^3\Pi_g$-$X^3\Pi_u$ (0-0) band (at 515 nm), and Ar I atomic lines (over 690 nm). [5.13, 14] Also, there were emission peaks at 390 and 430 nm, and it was difficult to identify them as either N_2^+ or CH emissions only from this spectrum. These emission peaks were respectively identified as the CH $B^2\Sigma$-$X^2\Pi$ (0-0) band and the CH $A^2\Delta$-$X^2\Pi$ (0-0) band by comparison of the peak shapes with those of the parallel-plate DBD operated in He/N_2 mixed gas shown in Fig. 2.12 in chapter 2. Comparing the spectra in each discharge mode, it was clearly seen that the intensities of OH A-X, N_2 C-B, and Ar I emission lines decreased with the change from the filament to glow modes, and the C_2 A-X, the CH B-X, and the CH A-X emission components could not be observed in the glow mode.

To analyze the characteristics and the critical acetone-vapor ratio of the discharge-mode transition, the peak emission intensities of the OH A-X (at 309 nm), N_2 C-B (at 337 nm), C_2 A-X (at 515 nm), and Ar I $2p_6$-$1s_5$ (at 763 nm, in Paschen's notation) transitions were plotted as a function of the acetone-vapor ratio in Fig. 5.5. From the results, the OH A-X emission intensity monotonically decreased with increasing the acetone-vapor ratio. The Ar I emission had a plateau between 0.18 and 0.30% then decreased in intensity. The N_2 C-B emission intensity peaked at 0.04% and decreased with further increasing the acetone-vapor ratio. It seems that the decrease speed of the N_2 C-B emission intensity became slow between 0.18 and 0.30%, in a similar range to the plateau observed in the Ar I emission. The C_2 A-X emission intensity increased at an increasing rate up to 0.22%, suddenly decreased from 0.26 to 0.32%, and could not be observed above 0.40%. This dependence of the C_2 emission on the acetone-vapor ratio clearly indicates that the change between the filament and glow discharge modes was in the
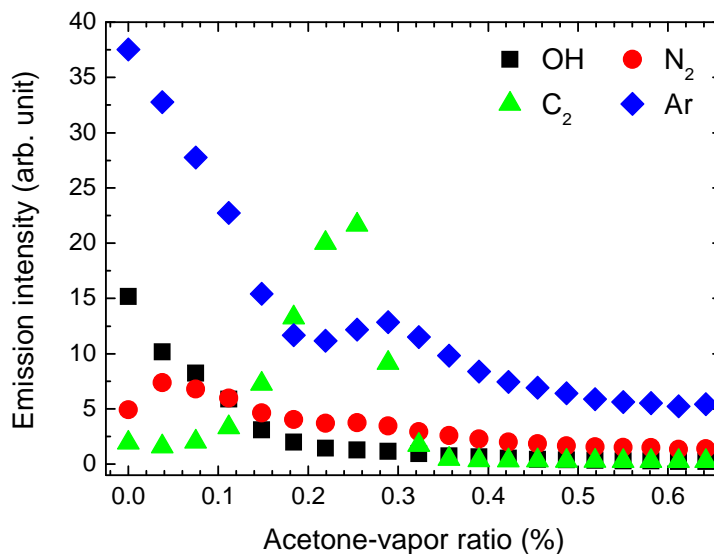
Figure 5.5   Optical emission intensity as a function of acetone-vapor ratio measured 5 mm from Cu plate. Electronic transitions corresponding to measured wavelengths are OH A-X (0-0) band (at 309 nm), N_2 C-B (0-0) band (at 337 nm), C_2 A-X (0-0) band (at 515 nm), and Ar I $2p_6$-$1s_5$ (at 763 nm, in Paschen notation).

range between 0.26 and 0.32%. From these results, especially those for the Ar and C_2 emission intensities, the reaction kinetics including the excitation of Ar atoms and the decomposition of the acetone molecule have a far from linear dependence on the acetone-vapor ratio around the transition.

5.2.3   Deposited carbon-based materials on grounded plate

Figure 5.6 shows microscopic photographs of the deposited materials on the Cu plate prepared by 10 minutes discharge with acetone-vapor ratios of 0.15% (in the filament mode, Fig. 5.6(a)) and 0.55% (in the glow mode, Fig. 5.6(b)). The photographs were recorded using an optical microscope with LED illumination and digital camera modules. Comparing the deposited materials, the deposited area in the filament mode was smaller than that in the glow mode, and
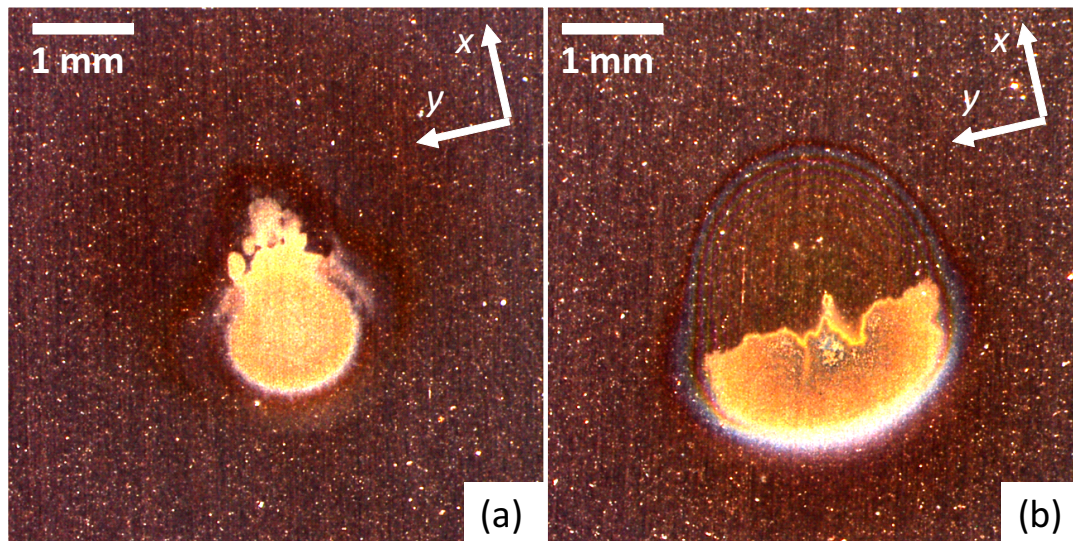
Figure 5.6   Microscopic photographs of deposited materials on Cu plate. Acetone-vapor ratios in 10 minutes discharge are (a) 0.15% (in filament mode) and (b) 0.55% (in glow mode). Peak value of applied voltage is 6.0 kV in each deposition.

an interference pattern can be observed only in the material deposited in the glow mode in the upper part of the image. This result indicates that the structure of the deposited material on the Cu plate strongly depends on the discharge mode of the jet-type DBD. In other words, when we consider deposition as a kind of "footprint" in the gaseous phase, this difference indicates the transition of internal reaction processes as well as that of the discharge structure.

The surface morphology of the deposited materials was observed in more detail using a scanning electron microscope (SEM). SEM images of the material deposited in the filament mode in Fig. 5.6(a) are shown in Fig. 5.7. Comparing the images taken on the bare Cu surface (without any deposited material, Fig. 5.7(b)) and near the center of the circular deposited material (Fig. 5.7(c)), the deposited material was rougher than the bare Cu surface, and there are small particles with a diameter of 1-3 μm on the surface. The density of deposited particles was larger in the bright upper area (Fig. 5.7(d)) than in the center. The overall streaky structure of the bare Cu surface was observed in the region with the deposited materials.

Figure 5.7   SEM images of deposited material on Cu plate with (a) overall photograph indicating SEM observation points. Acetone-vapor ratio in deposition is 0.15% (in filament mode). Magnification ratio of each SEM image is 3000 times.

In the material deposited in the glow mode (Fig. 5.6(b)), two types of deposited materials were clearly distinguished, one in the region with an interference pattern (Fig. 5.8(b)) and one in the half-moon discolored region (Fig. 5.8(c)), and there was an interface region between them (Fig. 5.8(d)). The image taken in the region with the interference pattern (Fig. 5.8(b)) suggests that the surface morphology in this region is very similar to that of the bare Cu surface (see Fig. 5.7(b)), and that a film like structure is deposited preserving the incident streaky structure. On the other hand, there were randomly aligned microstructures composed of nm-order particles in the image taken in the half-moon discolored region (Fig. 5.8(c)). The streaky structure of the bare Cu surface could be seen behind the accumulated particle structure, and the back
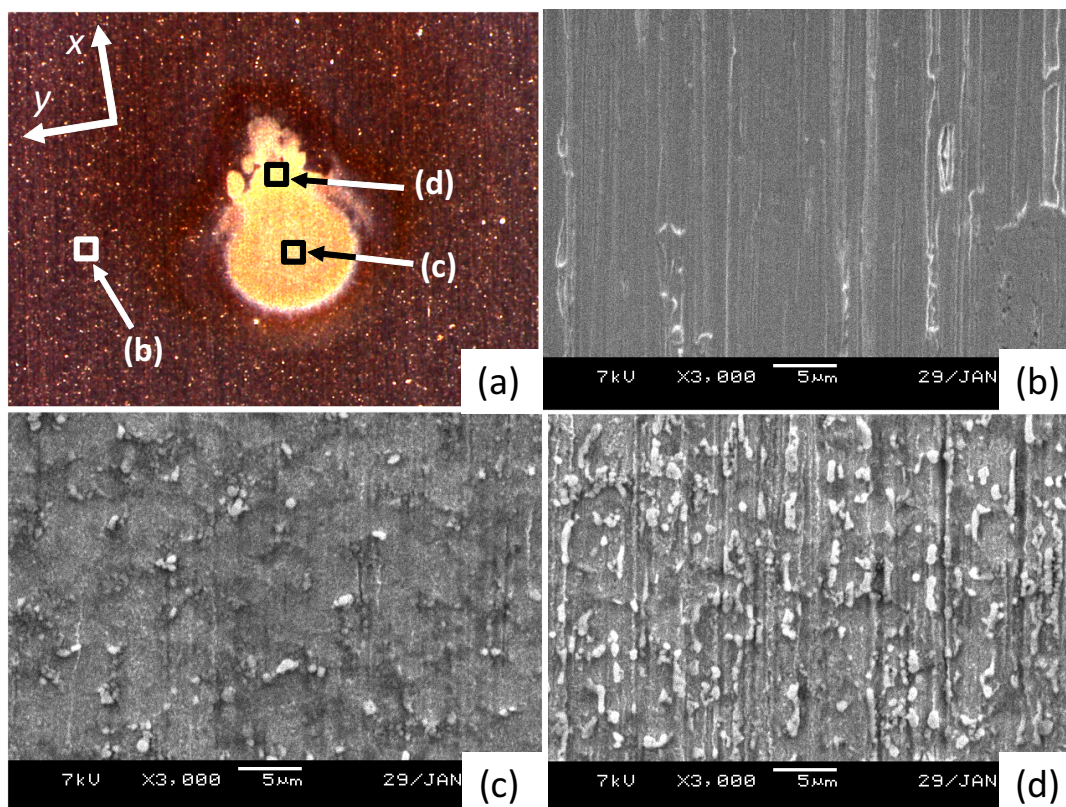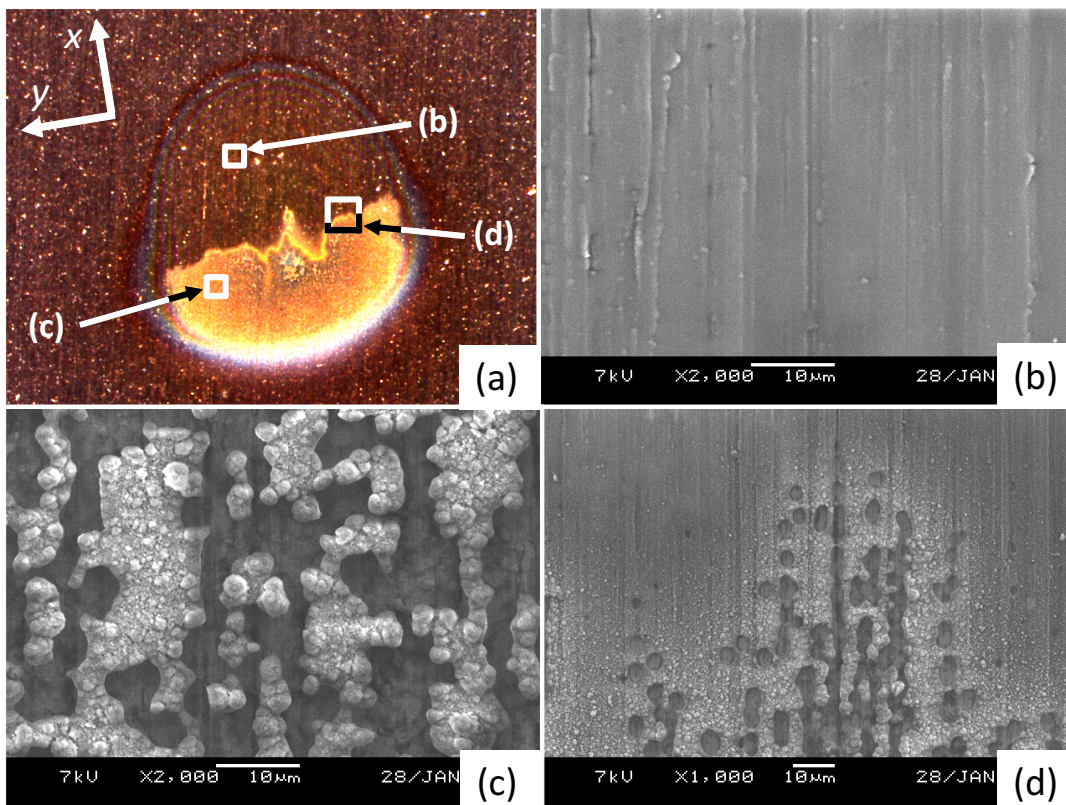
Figure 5.8   SEM images of deposited material on Cu plate with (a) overall photograph indicating SEM observation points. Acetone-vapor ratio in deposition is 0.55% (in glow mode). Magnification ratios of SEM images are (b) and (c) 2000 and (d) 1000 times.

surface was also different from the bare Cu surface, similarly to the material surface deposited in the filament mode. In their interface region (Fig. 5.8(d)), a gradual change from film like to accumulated particle structures was observed with a porous structure between them.

One-dimensional surface profiles of the deposited materials were measured using an atomic force microscope (AFM) as shown in Fig. 5.9. Comparing with the AFM profile of the bare Cu surface (corresponding to the SEM image shown in Fig. 5.7(b)), there were small roughness and particles with approximately 1 μm height in the deposited material in the filament mode (Fig. 5.7(c)). Also, it was confirmed from the profiles of the material deposited in the glow mode that the morphology of the deposited region with the interference pattern (Fig. 5.8(b)) was
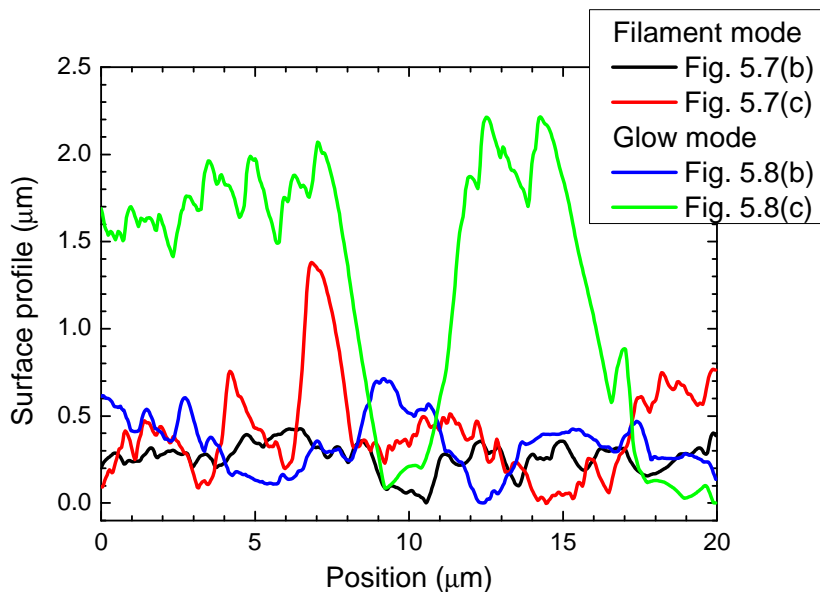
Figure 5.9   One-dimensional AFM profiles of materials deposited in filament and glow modes on Cu plate. Measurement for each material involved scanning in lateral direction of microscopic photograph (Fig. 5.6) and SEM images (Figs. 5.7 and 5.8). Measurement positions are identical to positions of SEM observation, and they are indicated by numbers shown in Figs. 5.7(a) and 5.8(a).

similar to that of the bare Cu surface and that the height of the accumulated particle structure (Fig. 5.8(c)) was approximately 2 μm. These results are in good agreement with the SEM observation results.

From the results of the microscopic observation, it was found that this jet-type DBD in the Ar/molecule mixed gas flow has potential to be applied to deposition processes not only thin films but also self-aligned microstructures. Since this study used the organic acetone molecules, the deposited materials were probably carbon-based polymer films and microparticles. In addition to these simple organic molecules, it is expected to realize well-controlled deposition of metals and metal oxides using the jet-type DBD with metal-organic precursors in the near future.

5.3   Coaxial DBD in Ar/NH$_3$ Mixed Flow

5.3.1   Experimental procedure

For generating plasmas in an atmospheric-pressure Ar/NH$_3$ mixed flow, a coaxial DBD configuration with a glass tube was built as shown in Fig. 5.10. The glass tube had inner and outer diameters at 2 and 6 mm, and its both ends were connected to stainless steel tube system preventing the leak of toxic NH$_3$ gas. Three copper-sheet electrodes with a 10-mm width were wrapped around the tube separated by 10 mm each other. The middle electrode was connected to a power supply, and others were connected to the ground. Around both ends of the glass tube, electrically floating copper rings on inner surface of the tube were inserted at 3 mm from the outer electrode's edge. The inner rings assisted the discharge ignition feeding seed elec-
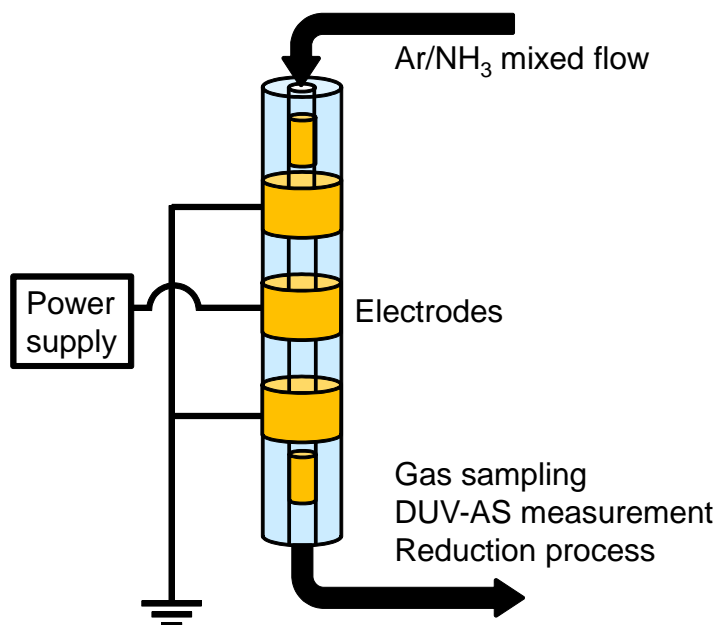

Figure 5.10   Schematic diagram of electrode configuration in coaxial DBD using Ar/NH$_3$ mixed flow.

trons and prevented the electric current flowing into the stainless steel tubes by terminating the plasma plume there.

Two cylinder cabinets were prepared for safely putting a NH_3 gas container and a gas cleaner cartridge, which eliminated NH_3 molecules from the exhausted gas, respectively, and the coaxial DBD system was placed to upper part in the cabinet for the cleaner cartridge. Between two cabinets, three mass flow controllers for setting Ar gas flow rate in a range from 0 to 3 L/min, NH_3 flow rate from 0 to 10 mL/min, and NH_3 flow rate from 10 to 100 mL/min were placed. A small fraction of NH_3 gas was merged to the Ar flow with controlling the NH_3 ratio to the Ar gas between the two cylinder cabinets. In addition to the coaxial DBD system, a gas sampling module and a long absorption gas cell were installed between the coaxial DBD system and the gas cleaner cartridge. The gas composition of the Ar/NH_3 flow after passing through the coaxial DBD was analyzed by a gas chromatography.

The absorption gas cell was utilized for a deep-ultraviolet absorption spectroscopy (DUV-AS) method, designed for hydrazine molecular fraction measurement in the Ar/NH_3 gas flow after the coaxial DBD. The length of the absorption cell between two quartz windows was 40 cm, and two optical fibers were equipped on both ends of the cell with collimators. A deuterium lamp for the DUV light source and the spectrometer used in the OES measurement were placed outside the cabinet and connected to the optical fibers. Absolute densities of hydrazine molecules in the post-discharge gas flow were derived using a Lambert-Beer's Law and a reported spectrum of absorption coefficients for hydrazine molecules in a wavelength range shorter than 250 nm. [5.15]

5.3.2   Glow-like discharge generation

Figure 5.11 shows spatial structures of the discharge emission in the coaxial DBD using the Ar/NH$_3$ mixed flow, observed by the digital camera as increasing the NH$_3$ flow rate. When the NH$_3$ flow rate was smaller than 2 mL/min, the temporal behavior of the coaxial DBD was a little unstable, and the upper-side discharge disappeared after a few minutes from cutting the NH$_3$ flow. The emission stably filled inside the glass tube approximately between 3 and 10 mL/min and gradually became unstable as further increasing. Random movement of a thin filament was observed when the NH$_3$ flow rate was over 12 mL/min. Different from the observation results of the Ar/acetone jet-type DBD, it was difficult to distinguish the discharge-color change in each NH$_3$ gas flow rate.
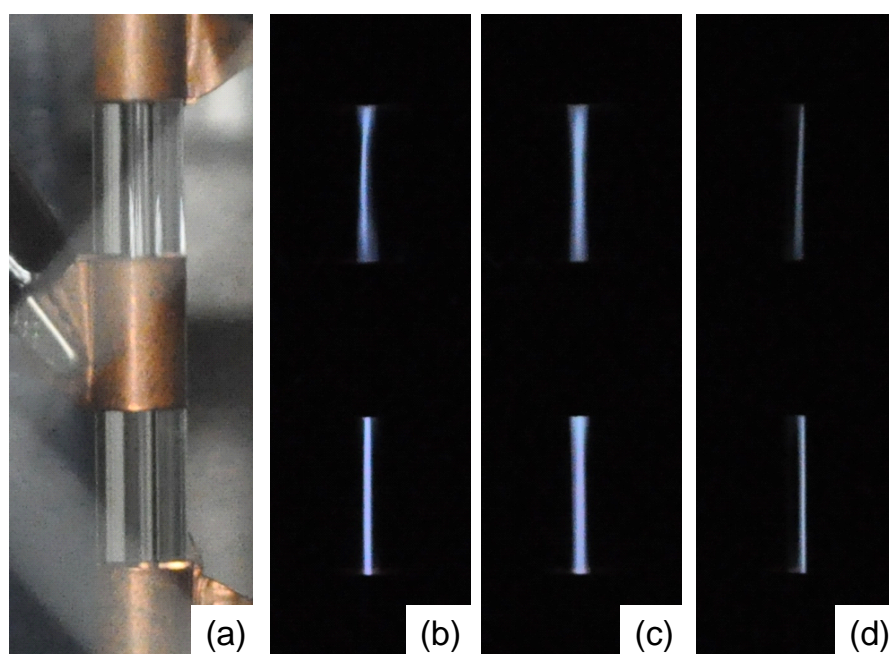

Figure 5.11   Photographs of discharge emission in coaxial DBD in Ar/NH$_3$ flow, together with (a) setup. NH$_3$ flow rates are (b) 1.3, (c) 8.9, and (d) 20.3 mL/min, respectively. Shutter speed of digital camera is 1/200 s from (b) to (d).
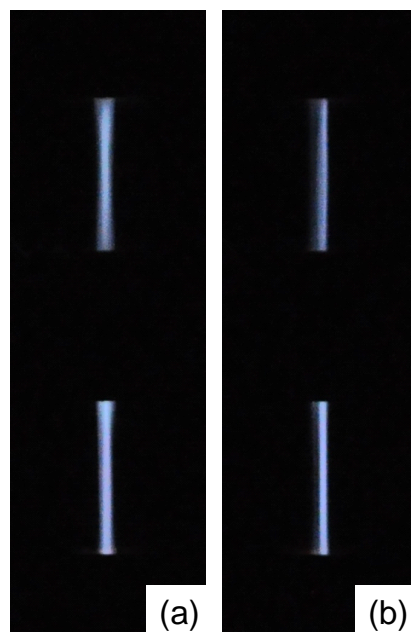
Figure 5.12 Photographs of discharge emission in coaxial DBD in Ar/NH$_3$ flow. NH$_3$ flow rates is 8.9 mL/min, and setting directions of flow rate are (a) increasing and (b) decreasing, respectively. Shutter speed of digital camera is 1/200 s.

In the observation of the discharge structure changing adjusting directions of the NH$_3$ flow rate, it was also found that the discharge structure was different when the NH$_3$ flow rate was set increasing or decreasing around 8 mL/min. As shown in Fig. 5.12, whereas the discharge emission observed increasing the NH$_3$ flow rate diffused inside the tube, the emission observed decreasing the NH$_3$ flow rate was thinner especially in the upper-side discharge. This result indicates that the discharge-mode transition in the DBD using Ar gas flow with small fraction of molecular impurity can be classified as a hysteresis phenomenon which has not been reported (nonlinear phenomenon) in the research area of high-pressure plasmas.

In order to explore potential applications of the coaxial DBD and investigate the hysteresis characteristics in the Ar/NH$_3$ mixed flow, optical emission spectra at the middle of the upper-side discharge were measured changing the NH$_3$ flow rate. From the measured emission spectrum shown in Fig. 5.13, Ar I and hydrogen (H$_\alpha$ and H$_\beta$) atomic lines and N$_2$ second positive

Figure 5.13 Example spectrum of optical emission measured in coaxial DBD in Ar/NH$_3$ flow at middle of discharge gap in upper part.

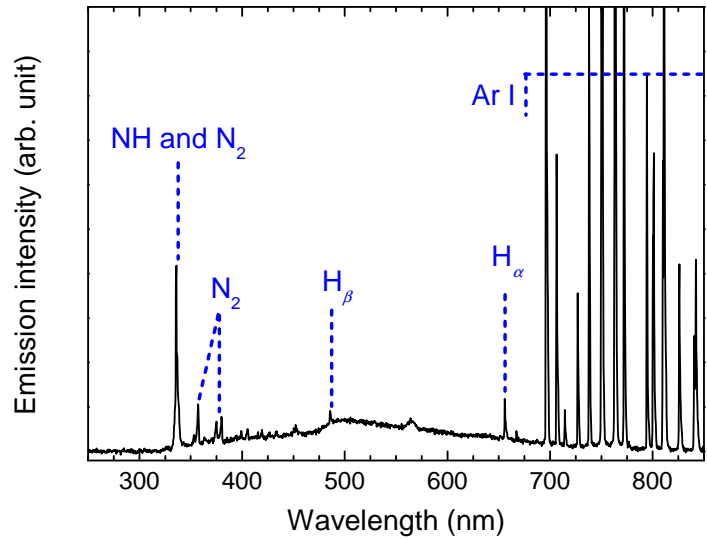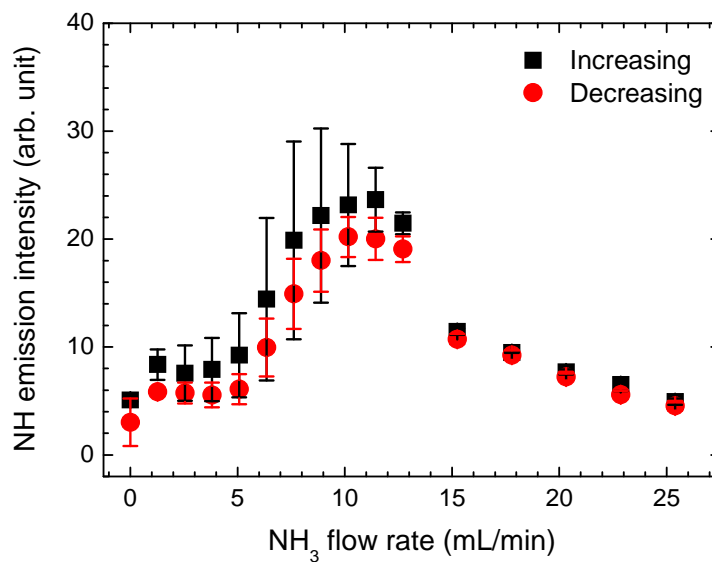Figure 5.14 Dependence of NH emission intensities on NH$_3$ flow rate measured in coaxial DBD in Ar/NH$_3$ flow setting NH$_3$ flow rates in increasing and decreasing directions. Measurement wavelength and corresponding electronic transition are at 336 nm and NH *A-X* (0-0) band.

C-B and NH 3360Å system $A^3\Pi$-$X^3\Sigma$ (0-0) molecular bands were distinguished. [5.13, 14] The detection of H atomic and N_2 molecular lines shows that some fraction of the NH_3 molecules were completely decomposed into atomic species inside the discharge region. These results suggest that there are the potential novel applications using this coaxial DBD by utilizing nitriding properties of N atoms and NH molecules. Although the hysteresis property was observed in the discharge structure, there was little difference in dependences of the NH emission intensity on the NH_3 flow rate measured both increasing and decreasing the flow rate, as shown in Fig. 5.14. From this result, the excitation and reaction kinetics in the coaxial DBD has little hysteresis property. Emission enhancement around 10 mL/min of the NH_3 flow rate is probably due to the Penning ionization process between Ar metastable atoms having a potential energy at 11.5 eV [5.14] and NH_3 neutral molecules having a ionization energy at 10.0 eV [5.16], similar to the relationships in He/N_2 mixed gases. The influence of the Penning ionization in the Ar/molecule DBD should be further investigated for better understanding of the discharge structure, comparing with the He/N_2 DBD discussed in chapter 2.

5.3.3   Reduction and nitrization processes

For the investigation of NH_3 decomposition in the coaxial DBD, the volume ratio of H_2 molecules in the Ar/NH_3 flow after the coaxial DBD was measured by the gas chromatography sampling 500-μL gas downstream of the discharge region. The measurement results of H_2 volumes and volume ratios to the added NH_3 molecules at four NH_3 flow rates and three frequencies of the applied voltage were listed in table 5.1. This result indicates that the NH_3 decomposition was promoted by the increase of the applied-voltage frequency due to the increase of the time duration of plasma generation. In addition to this, it is also effective to

Table 5.1   Volumes (volume ratios (vol%) to added NH_3 molecules) of H_2 molecules in Ar/NH_3 flow sampled after coaxial DBD measured by gas chromatography. Total volume of sampled gas is 500 μL.

Frequency of applied voltage	NH_3 flow rate (mL/min)			
	0	6	14	40
10 kHz	0 μL (0 vol%)	0.12 μL (7.4 vol%)	0.10 μL (3.0 vol%)	0.11 μL (1.2 vol%)
20 kHz	0 μL (0 vol%)	0.22 μL (14.0 vol%)	0.26 μL (8.2 vol%)	0.22 μL (2.3 vol%)
30 kHz	0 μL (0 vol%)	0.32 μL (19.6 vol%)	0.50 μL (15.6 vol%)	0.70 μL (7.2 vol%)

set smaller value of the NH_3 molecular fraction in the Ar/NH_3 flow to reduce residual NH_3 molecules not decomposed to the reactive species.

Figure 5.15 shows an example spectrum of absorbance, $-\ln(I_T/I_0)$, measured by the DUV-AS method, together with a reported spectrum of absorption coefficient of hydrazine molecule. The rising slope of the absorbance coincided to the reported spectrum of the absorption coefficient, and the absolute hydrazine density could be calculated using the absorbance at 225 nm shown by a vertical blue dashed line in Fig. 5.15. Because of the specification of the CCD detecting module in the spectrometer, a minimum wavelength of the measurement was approximately 215 nm in this experiment. Also, there was negative peaks of absorbance around 220 nm and these wavelength corresponded to NH_3 $\tilde{A}^1A_2''$-$\tilde{X}^1A_2$ absorption bands. [5.17] This negative peak of NH_3 absorption indicates that the NH_3 molecular fraction in the Ar/NH_3 flow is decreased by the decomposition in the coaxial DBD.

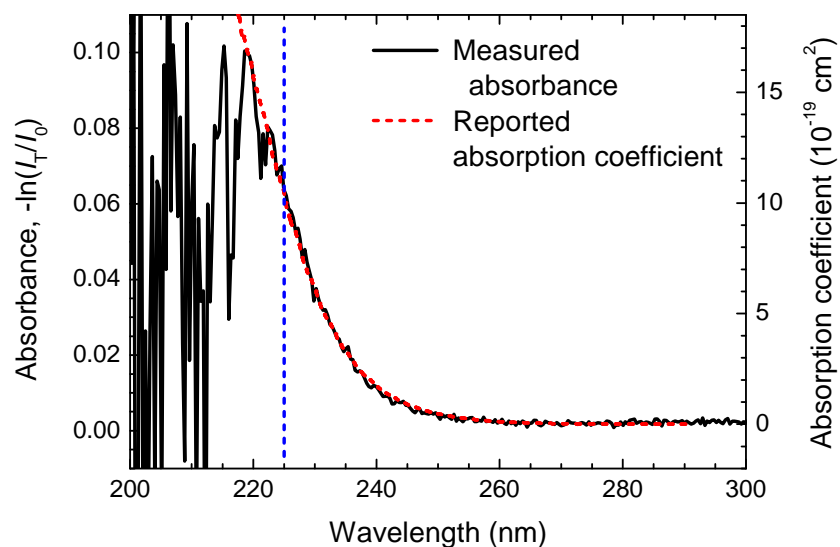Figure 5.15 Example absorbance spectrum of DUV-AS measurement in Ar/NH$_3$ gas flow after coaxial DBD, together with spectrum of reported absorption coefficient of hydrazine molecules. [5.15]
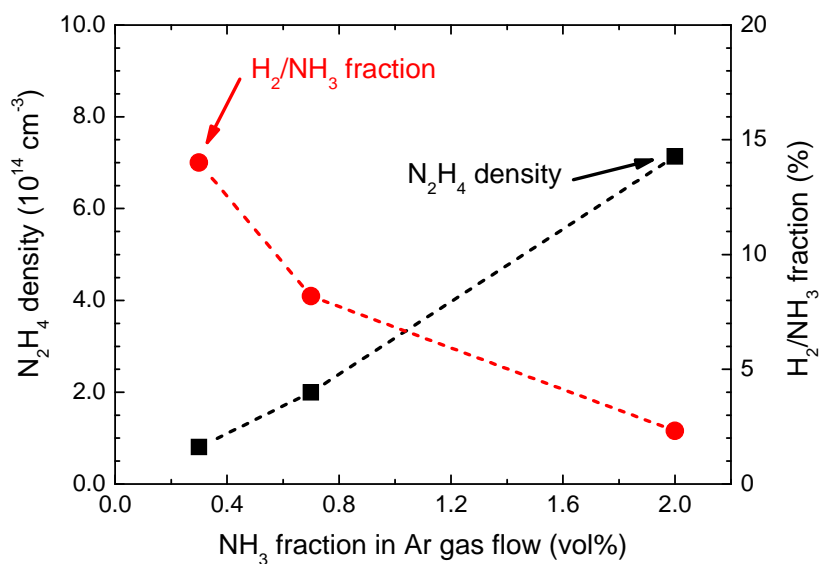
Figure 5.16 Dependences of hydrazine density and H$_2$ molecular fraction to input NH$_3$ molecules on NH$_3$ fraction in Ar gas flow. Frequency of applied voltage was fixed at 20 kHz in this measurement.

From the measurement results of the gas chromatography (table 5.1) and the DUV-AS in the three NH_3 fractions, the dependences of the hydrazine density and the ratio of the H_2 molecules to input NH_3 amount in the post-discharge gas, which can be a reference of the decomposition ratio of input NH_3 molecules, are plotted in Fig. 5.16. From this figure, the hydrazine density was not proportional to the decomposition ratio of the input NH_3 molecules, and it increased as increasing the NH_3 ratio. The reason why the hydrazine molecules are not produced in the smaller range of the NH_3 ratio is probably that the NH_3 molecules are decomposed to NH molecules, N, and H atoms and the fraction of NH_2, which is main radical forming hydrazine molecules, [5.18] is relatively small. This idea can be supported by the results of DUV-AS measurement in the small NH_3 ratio. In the absorbance spectra only measured in 0.3% of the NH_3 ratio as shown in Fig. 5.17, there was an absorption peak at 227 nm in addition to the

Figure 5.17   Absorbance spectrum of Ar/NH_3 mixed gas after coaxial DBD measured by DUV-AS method in smaller condition of NH_3 ratio aroung 0.3%. A absorption peak at 227 nm in addition to hydrazine absorption slope is NO A-X (0-0) band.

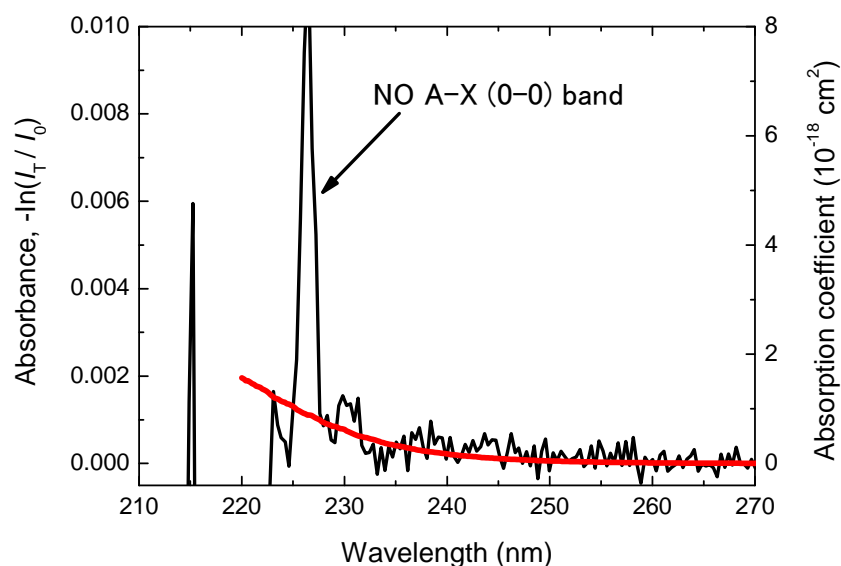hydrazine absorption slope and the NH_3 absorption dip. This abosrption peak was identified as NO $A^2\Sigma^+$-$X^2\Pi$ (0-0) molecular absorption band, and the NO molecules were probably generated by a reaction between N atoms generated in the coaxial DBD and O atoms at the inner surface of the tube. Therefore, the detection of NO molecules in the post-discharge gas indicates the production of N atoms inside the discharge by complete decomposition of the NH_3 molecules.

Following the experimental analysis of excited and produced species by the coaxial DBD in the Ar/NH_3 mixed flow, two kinds of novel applications using the discharge can be proposed. The first one is a surface nitrization process inside the coaxial DBD using small fractions of the NH_3 molecules, utilizing the NH molecules and N atoms generated in the discharge region. The nitrization process has not yet been realized using the thermal non-equilibrium APPs, but it is expected to be applied to improving hardness of thin films and controlling work functions of metal-oxide films. Also, in the post-discharge gas phase after the coaxial DBD using relatively large fractions of the NH_3 molecules, a surface reduction process by the hydrazine molecules can be realized. Different from the reduction processes using APPs in H_2 added noble gas which are recently being developed in many research institutes, [5.19–21] the hydrazine processes can be applied easily to larger-area and complex surfaces because the hydrazine molecules are stable molecules and have longer lifetimes than H atomic radicals.

5.4   Summary

In summary, a transition phenomena between filament and glow modes in two types of the DBDs using Ar/molecule mixed flows are investigated through spectroscopic and electrical experiments. Also, potential material-process applications of the DBDs in the Ar/molecule

flow are introduced in this chapter.

For long-running experiments using organic molecules, a two-gas-flow configuration using a tilted He coaxial DBD jet and a vertical Ar/acetone flow was newly developed. The spatial and temporal stabilities were much greater in the glow mode, similarly to the difference between He and Ar DBDs. From optical emission spectra, generation of C_2 and CH molecules due to decomposition of the acetone molecules could not be found in the glow mode, although the these molecular emission intensities increased with increasing acetone-vapor ratio in the filament mode. This result suggests that the changes of the ionization processes and electron energy distributions, which are related to Penning ionization between Ar metastable atoms and neutral acetone molecules having large influence on the He/N_2 DBD as discussed in chapter 2, probably have a strong effect on the discharge-mode transition. The deposited materials on the Cu plate were completely different in each discharge mode, and μm-order porous materials composed of nm-order particles were observed in the glow mode. From these results, the jet-type DBD in an Ar gas flow with small fraction of organic impurities has potentials to become a useful tool for the research on nonlinear reaction kinetics in the high-pressure plasmas and applications of novel material deposition processes at atmospheric pressure.

In addition to investigating influence of organic molecules on the Ar DBD, inorganic ammonia molecules were also tested as the added molecule into the Ar gas flow to confirm the glow-like DBD generation, because they have similar ionization energy to the acetone molecules. The discharge-mode transition was similarly observed in the coaxial DBD using Ar/NH_3 mixed flow; however, the difference between the two discharge modes was only in their appearance and could not be seen in their emission spectra. The critical factor triggering the discharge-mode transition should be discussed further in future studies considering the difference between or-

ganic and inorganic additive molecules and the nonlinear properties, for example, the discontinuous change in reaction kinetics and the hysteresis dependence of discharge appearance on the molecular fraction. The OES and DUV-AS measurement results suggest that this APP source has enough potential to be applied to surface reduction and nitrization process controlling suitable NH_3 fractions for each processes respectively.

References

[5.1] U. Kogelschatz, Y. S. Akishev, K. H. Becker, E. E. Kunhardt, M. Kogoma, S. Kuo, M. Laroussi, A. P. Napartovich, S. Okazaki, and K. H. Shoenbach: in *Non-Equilibrium Air Plasmas at Atmospheric Pressure*, eds. K. H. Becker, U. Kogelschatz, K. H. Schoenbach, and R. J. Barker (IOP Publishing, Bristol, 2005).

[5.2] U. Kogelschatz: Plasma Chem. Plasma Process. **23** (2003) 1.

[5.3] S. Kanazawa, M. Kogoma, T. Moriwaki, and S. Okazaki: J. Phys. D **83** (1988) 838.

[5.4] F. Massines, A. Rabehi, P. Decomps, R. B. Gadri, P. Segur, and C. Mayoux: J. Appl. Phys. **83** (1998) 2950.

[5.5] S. Okazaki, M. Kogoma, and H. Uchiyama: Proc. 3rd Int. Symp. High Pressure Low Temperature Plasma Chemistry, 1991, p. 101.

[5.6] F. Massines, N. Gherardi, N. Naude, and P. Segur: Plasma Phys. Control. Fusion **47** (2005) B577.

[5.7] T. Shirafuji, T. Kitagawa, T. Wakai, and K. Tachibana: Appl. Phys. Lett. **83** (2003) 2309.

[5.8] Y. Ito, Y. Fukui, K. Urabe, O. Sakai, and K. Tachibana: Jpn. J. Appl. Phys. **49** (2010) 066201.

[5.9] Y. Li, J.-D. Wang, Z.-H. Huang, H.-Q. Xu, and X.-T. Zhou: J. Environ. Sci. Health A **37** (2002) 1453.

[5.10] T. Somekawa, T. Shirafuji, O. Sakai, and K. Tachibana: J. Phys. D **97** (2005) 123301.

[5.11] K. Urabe, T. Morita, K. Tachibana, and B. N. Ganguly: J. Phys. D **43** (2010) 095201.

[5.12] N. Gherardi, G. Gouda, E. Gat, A. Ricard, and F. Massines: Plasma Sources Sci. Technol. **9** (2000) 340.

[5.13] R. W. B. Pearse and A. G. Gaydon: *The Identification of Molecular Spectra* (Chapman and Hall, London, U.K., 1976).

[5.14] Y. Ralchenko, A. E. Kramida, J. Reader, and NISR ASD Team: NIST Atomic Spectra Database (version 4.1.0, 2011) [http://physics.nist.gov/asd3].

[5.15] G. L. Vaghjiani: J. Chem. Phys. **98** (1993) 2123.

[5.16] P. J. Linstrom and W. G. Mallard: NIST Chemistry WebBook, NIST Standard Reference Database (No. 69, 2010) [http://webbook.nist.gov].

[5.17] J. A. Syage, R. B. Cohen, and J. Steadman: J. Chem. Phys. **97** (1992) 6072.

[5.18] A. Fateev, F. Leipold, Y. Kusano, B. Stenum, E. Tsakadze, and H. Bindslev: Plasma Process. Polym. **2** (2005) 193.

[5.19] Y. Sawada, H. Tamaru, M. Kogoma, M. Kawase, and K. Hashimoto: J. Phys. D **29** (1996) 2539.

[5.20] H. Inui, K. Takeda, H. Kondo, K. Ishikawa, M. Sekine, H. Kano, N. Yoshida, and M. Hori: Appl. Phys. Express **3** (2010) 126101.

[5.21] S. Tajima, S. Tsuchiya, M. Matsumori, S. Nakatsuka, and T. Ichiki: Thin Solid Films **519** (2011) 6773.

Chapter 6

Concluding Remarks

The spectroscopic studies on dielectric barrier discharges (DBDs) operated in dilute helium (He) and argon (Ar) gases at atmospheric pressure and future perspectives following the experimental research are summarized in this concluding chapter.

In chapter 2, formation mechanisms of electron-density distribution in a parallel-plate DBD, which is the most basic DBD electrode configuration, and influence of the nitrogen (N_2) impurity on the discharge behavior are discussed. The electron-density distribution was successfully measured by a newly developed combination method of the CO_2-laser heterodyne interferometry (CO_2-LHI) and the millimeter-wave (mm-wave) transmission. This combination spectroscopic measurement could derive spatiotemporal structures of electron density inside the small-scale plasmas having fast temporal evolutions. The temporal-peak electron density near the dielectric barrier approached 5×10^{12} cm^{-3}, and the presence of electrons near the middle of the discharge gap was detected only in the 0.25% condition of the N_2 impurity ratio. The laser absorption spectroscopy (LAS) measurement results indicated that the localization of electron density was due to formation of a negative glow region near the temporal cathode. Also, enhanced ionization in the 0.25% condition of the N_2 impurity ratio was confirmed from the numerical calculation of total ionization frequency using a zero-dimensional ionization model. The reason for the dependence of electron density on the N_2 impurity ratio was the contribution of a Penning ionization process by collisions between He metastable atoms and N_2 neutral molecules, and this could be confirmed from the experimental results of the optical emission

spectroscopy (OES) measurement. These results confirmed the accuracy of past studies of numerical calculations simulating the DBDs, and indicated that the combination measurement method developed in this study can be applied in the future to various kinds of small-scale plasma sources operated at high pressure.

For industrial applications using the DBD, various electrode configurations have been recently developed. Among them, a coaxial DBD jet, composed of a dielectric tube, one or two ring electrodes around the tube, and a noble gas flow in the tube, becomes one of the most widely used DBDs not only for material processes but also for liquid and biomedical processes. Unknown basic discharge mechanisms of the coaxial DBD jet were investigated by the laser spectroscopic measurements and their experimental results were introduced in chapter 3. It was revealed by the laser induced fluorescence spectroscopy (LIF) measurement that the main mechanism forming the plasma plume is an ionization-front propagation similarly to a positive corona discharge localized inside a noble-gas flow channel surrounded by ambient air. Also, novel electrode configurations using insulated wires enabled us to control the plasma plume length and the excited-species density in the plume independently. Calculated results of electrical potential distribution using estimated conditions obtained from the experimental results indicated that localized ignition of the ionization front was at the downstream edge of surface charges inside the tube, which was accumulated by the coaxial DBD in the previous discharge phase with the reverse polarity. The calculation results of temporal evolutions of the electrical potential in two kinds of the electrode configuration suggested that the potential decay at the ignition point of the ionization front strongly affected the plume length. The results of this basic study on the coaxial DBD jet can be reference data for the following development of applications and further improvement of the discharge properties.

In order to apply the coaxial DBD jet to material processes on a conductive substrate, it must be considered that there was large difference in the discharge behavior between with and without the conductive substrate in front of the plasma plume. In chapter 4, the discharge mechanisms in the driving mode with the conductive substrate called a jet-type DBD are investigated by the laser spectroscopic measurements, comparing the discharge behaviors with and without the grounded conductive plate. Using an inverse Abel transformation method, radial distributions of He metastable atoms and ground N_2^+ ions densities were derived in the jet-type DBD operated both with and without the conductive plate. In both discharge configurations, the radial distributions had a ring-like hollow structure in the rise timing of the applied voltage and a center-peaked structure in the fall timing. In addition to the ionization-front propagation observed in the coaxial DBD jet, in the jet-type DBD operated with the conductive plate, there were transient-glow discharges after the ionization-front propagation in both rise and fall timings of the applied voltage, and peak densities of excited species in the plasma plume are much greater than that operated without the conductive plate. Also, it was revealed that the ionization mechanism near the conductive plate was dominated by a direct electron-impact ionization process of N_2 molecules and this mechanism is different from the coaxial DBD jet whose dominant ionization mechanism was the Penning ionization process between He metastable atoms and N_2 neutral molecules. The revealed discharge mechanisms in the jet-type DBD in this chapter give us guidelines for controlling its discharge properties, and the material processes using the jet-type DBDs will be spreading wide application area following the well understandings of their discharge behaviors.

In chapter 5, a transition-like phenomenon between filament and glow discharge modes in the DBD using an Ar gas flow with molecular impurities were introduced. When the acetone

molecules were used as the additive molecule, a two-gas-flow configuration of the jet-type DBD composed of a tilted He coaxial DBD jet and a vertical Ar/acetone flow achieved long-running experiments under the same discharge conditions. Comparing the discharge currents in each discharge mode, the stability was much greater in the glow mode than in the filament mode, similarly to the difference between He and Ar DBDs. Ar, CH, and C_2 emission intensities have a strongly nonlinear dependence on the acetone-vapor ratio around the transition criterion, and this indicates that the discharge-mode transition can be identified as a nonlinear phenomenon in the reaction kinetics inside such small-scale high-pressure plasmas. The deposited materials on the Cu plate were completely different in each discharge mode, and μm-order porous materials composed of nm-order particles were observed in the glow mode. In addition to the organic acetone molecules, inorganic ammonia molecules are tested to generate homogeneous coaxial DBD. The discharge transition from filamentary to glow-like modes were also observed in the Ar/ammonia discharge; however, the difference of appearances and emission spectra between the two discharge modes was much less clearer than the Ar/acetone discharge. The deep-ultraviolet absorption spectroscopy (DUV-AS) measurement showed the potential of this Ar/ammonia DBD to be applied to reduction and nitrization processes utilizing hydrazine molecules in the post-discharge gas and N atoms and NH molecules inside the plasma, respectively.

Summarizing the results of spectroscopic studies described in each chapter, the overall discharge mechanisms, which are important for controlling the DBDs and applications, are as follows. At the ignition timing of the discharge, the spatial distribution of surface charges on the dielectric barrier layer accumulated in the previous discharge cycle has crucial influence on the discharge behaviors including spatial distribution of excited-species density in the gener-

ated plasma, especially when the electrode configuration is complex, for example, the coaxial DBD jet. After the discharge ignition and formation of the discharge channel, the main current of the DBD flows due to formation of the transient glow discharge with the typical glow-discharge structure. In and after the transient-glow discharge, Penning ionization processes between metastable atoms and neutral molecules contribute to increase the electron density in the lower electric field region, and this additional ionization process probably has the critical effect of homogeneous plasma generation in the DBDs. Considering these discharge mechanisms confirmed by the spectroscopic studies in this dissertation, the better understanding of the DBDs including behavior of minor excited species and electron energy distribution, which are very difficult to measure experimentally and cyclopaedically at this time, can be grown through computational studies based on the accurate experimental data. Also, the control of the spatial distributions and chemical kinetics of excited species inside the DBDs by utilizing the accumulated surface charges and Penning ionization processes will open the next door to improvement of the DBD science and engineering.

Acknowledgements

I would like to sincerely acknowledge all the people listed below who have supported and encouraged my work at Plasma Physics and Technology Laboratory in Kyoto University.

First of all, I express my sincere appreciation to Associate Professor Osamu Sakai at Kyoto University. He has provided me invaluable opportunity and appropriate direction throughout my study since I started experiments in our laboratory as an undergraduate student. I also would like to thank Professor Gikan Takaoka, Professor Masao Kitano, and Professor Yoichi Kawakami at Kyoto University very much for their profound advices during and for finishing this study.

During my six-years study in Kyoto University, I have received great supports from both teaching staffs and students in the laboratory. Especially, I would like to express my deepest appreciation to Professor Kunihide Tachibana, a professor emeritus at Kyoto University and now a professor at Osaka Electro-Communication University, for giving me advices and encouragements in learning spectroscopic diagnostic methods for high-pressure plasmas. I also appreciate Professor Tatsuru Shirafuji at Osaka City University (a former Associate Professor at Kyoto University), Lecturer Toshihiro Nakamura, and Mr. Makoto Kubo (a former Assistant Professor) for their helpful advice, and express my gratitude to all of postdoctoral researchers and students in my laboratory including the past members. Among them, I would like to express my special thanks to Dr. Yosuke Ito, Dr. Dae-Sung Lee, Dr. Nobuhiko Takano, and Dr. Joon-Young Choi for their kind advices and supports for my experiments, and Mr. Tadasuke Morita, Mr. Yutaka Fukui, Mr. Keitaro Yamada, and Mr. Yu Hiraoka for their substantial cooperations. Not only researchers, I am indebted to Ms. Keiko Yamada, a secretary in the Plasma Physics and Technology Laboratory, for her very considerate assistance.

In addition to the people at Kyoto University, I would like to acknowledge researchers at other institutes in Japan and United States of America who have promoted collaborated studies with me. Although all results of these collaborated experiments could not be included in this dissertation, they gave me a lot of meaningful comments and discussions on my study. Associate Professor Takanori Ichiki and Dr. Satomi Tajima at University of Tokyo gave me an opportunity to diagnose an Ar microplasma jet and improve my technique of spectroscopic measurements. With Professor Masafumi Jinno and Assistant Professor Hideki Motomura at Ehime University, collaborated experiments about discharge behaviors in an pure Ar gas flow and He_2 dimer generation in the coaxial DBD jet were successfully done in their laboratory. In Center for Advanced Power and Energy Conversion (CAPEC) at Wright State University (Dayton, OH, U.S.A.), trial experiments and detailed ICCD-camera observation of the jet-type DBD using He and Ar/acetone crossed flows was carried out with Dr. Biswa Ganguly and Dr. Brian Sands at Air Force Research Laboratory (AFRL). I also thank Dr. Robert Leiweke at AFRL, Professor George Huang, and all students in CAPEC at Wright State University for their kind supports in the experiments and my visit in Dayton. For the study about homogeneous DBD generation in Ar/acetone mixed gas, Dr. Sachiko Okazaki, a professor emeritus at Sophia University kindly gave me her past research materials, suggestions, and powerful encouragements, and Professor Akimitsu Hatta at Kochi University of Technology supported in the microscopic observations of deposited materials.

During my student years in Ph.D. course at Kyoto University, I received financial supports of monthly stipends for research fellows from Japan Society for the Promotion of Science (JSPS), and for research assistants from Global Center of Excellence (GCOE) program for Education and Research on Photonics and Electronics Science and Engineering in Kyoto University. This

List of Publications

[1. Scientific Journal and Book Chapter]

1.1. <u>Keiichiro Urabe</u>, Yosuke Ito, Kunihide Tachibana, and Biswa N. Ganguly, "*Behavior of N_2^+ Ions in He Microplasma Jet at Atmospheric Pressure Measured by Laser Induced Fluorescence Spectroscopy*", Applied Physics Express, **1** (2008) 066004 (3pp).

1.2. Joon-Young Choi, Nobuhiko Takano, <u>Keiichiro Urabe</u>, and Kunihide Tachibana, "*Measurement of electron density in atmospheric pressure small-scale plasmas using CO_2-laser heterodyne interferometry*", Plasma Sources Science and Technology, **18** (2009) 035013 (8pp).

1.3. <u>Keiichiro Urabe</u>, Tadasuke Morita, Kunihide Tachibana, and Biswa N. Ganguly, "*Investigation of discharge mechanisms in helium plasma jet at atmospheric pressure by laser spectroscopic measurements*", Journal of Physics D: Applied Physics, **43** (2010) 095201 (13pp). **[selected to "2010 Highlights" and "the most popular articles published in JPhysD" in 2011]**

1.4. <u>Keiichiro Urabe</u>, Yosuke Ito, Osamu Sakai, and Kunihide Tachibana, "*Interaction between Dielectric Barrier Discharge and Positive Streamer in Helium Plasma Jet at Atmospheric Pressure*", Japanese Journal of Applied Physics, **49** (2010) 106001 (6pp).

1.5. <u>Keiichiro Urabe</u>, Hideki Motomura, Osamu Sakai, and Kunihide Tachibana, "*Enhancement of visible He_2 emission by infrared laser excitation of He metastable atoms in atmospheric-pressure plasma jet*", Journal of Physics D: Applied Physics, **44** (2011) 042001 (5pp).

1.6. <u>Keiichiro Urabe</u>, Osamu Sakai and Kunihide Tachibana, "*Combined spectroscopic methods for electron-density diagnostics inside atmospheric-pressure glow discharge using He/N$_2$ gas mixture*", Journal of Physics D: Applied Physics, **44** (2011) 115203 (11pp).

1.7. <u>Keiichiro Urabe</u>, Keitaro Yamada, and Osamu Sakai, "*Discharge-Mode Transition in Jet-Type Dielectric Barrier Discharge Using Argon/Acetone Gas Flow Ignited by Small Helium Plasma Jet*" Japanese Journal of Applied Physics, **50** (2011) 116002 (11pp).

1.8. <u>Keiichiro Urabe</u>, Brian L. Sands, Osamu Sakai, and Biswa N. Ganguly, "*Temporally-Resolved Imaging of Jet-Type Dielectric Barrier Discharge using He and Ar/Acetone Crossed Gas Flows*" IEEE Transactions on Plasma Science, **39** (2011) in press (2pp).

1.9. <u>Keiichiro Urabe</u>, Brian L. Sands, Biswa N. Ganguly, and Osamu Sakai, "*Temporally and spectrally resolved observation of crossed-flow DBD plasma jet using pure helium and argon/acetone mixed gases*" submitted in Plasma Sources Science and Technology.

1.10. <u>Keiichiro Urabe</u> and Kunihide Tachibana, "*Heterodyne interferometer for measurement of electron density in high-pressure plasmas*" in *CO$_2$ Laser - Optimisation and Application* ed. D. C. Dumitras, (InTech, Rijeka, to be published in February, 2012).

[2. International Conference (presented by the author)]

2.1. <u>Keiichiro Urabe</u>, Yosuke Ito, Makoto Kubo, and Kunihide Tachibana, "*Spatiotemporally Resolved Spectroscopic Diagnostics of Low-frequency Driven Microplasma Jet*", 6th EU-Japan Joint Symposium on Plasma Processing, P-15 (Okinawa, Japan, April 2008), Poster presentation.

2.2. <u>Keiichiro Urabe</u>, Yosuke Ito, and Kunihide Tachibana, "*Spatiotemporal Resolved Diagnostics of a Microplasma Jet using Laser Spectroscopy Methods*", International Congress on Plasma Physics 2008, EAP P3-150 (Fukuoka, Japan, September 2008), Poster presentation.

2.3. <u>Keiichiro Urabe</u>, Yosuke Ito, Kunihide Tachibana, and Osamu Sakai, "*Investigation of Discharge Mechanisms in Microplasma Jet by Laser Spectroscopic Measurements*", Fundamentals and Applications of Microplasmas, P1-8 (San Diego, USA, March 2009), Poster presentation.

2.4. <u>Keiichiro Urabe</u>, Yosuke Ito, Joon-Young Choi, and Kunihide Tachibana, "*Measurement of Plasma Parameters in Microplasmas using Laser Spectroscopic Methods*", ISPC-19 Pre-Symposium in Japan "Toward the Next Generation of Plasma Science and Technology", (Kyoto, Japan, May 2009), Poster presentation.

2.5. <u>Keiichiro Urabe</u>, Joon-Young Choi, Yosuke Ito, Kunihide Tachibana, and Osamu Sakai, "*Diagnostics of Dielectric Barrier Discharge at Atmospheric Pressure by Laser Spectroscopic Measurements*", 19th International Symposium on Plasma Chemistry, P1.3.12 (Bochum, Germany, July 2009), Poster presentation.

2.6.   <u>Keiichiro Urabe</u>, Yosuke Ito, Joon-Young Choi, Osamu Sakai, and Kunihide Tachibana, "*Dynamics of dielectric barrier discharge in non-uniform gas composition investigated by laser spectroscopic measurements*", 62nd Annual Gaseous Electronics Conference, FT3-1 (Saratoga Springs, USA, October 2009), Oral presentation.

2.7.   <u>Keiichiro Urabe</u>, Joon-Young Choi, Osamu Sakai, and Kunihide Tachibana, "*Spatial Distribution of Electron Density in a Parallel-plate Dielectric Barrier Discharge Measured by CO_2-laser Heterodyne Interferometry*", 2nd International Symposium on Advanced Plasma Science and its Applications for Nitrides and Nanomaterials, 8p-A02OA (Nagoya, Japan, March 2010), Oral presentation.

2.8.   <u>Keiichiro Urabe</u>, Joon-Young Choi, Yosuke Ito, and Osamu Sakai, "*Spatiotemporal Distribution of Electron Density inside Parallel-Plate Dielectric Barrier Discharge*", 3rd GCOE International Symposium on Photonics and Electronics Science and Engineering, P-41 (Kyoto, Japan, March 2010), Poster presentation.

2.9.   <u>Keiichiro Urabe</u>, Osamu Sakai, and Kunihide Tachibana, "*Spatiotemporal structure of electron density inside atmospheric pressure glow discharge measured by spectroscopic methods*", 63rd Gaseous Electronics Conference / 7th International Converence on Reactive Plasmas, TF3.008 (Paris, France, October 2010), Oral presentation.

2.10. <u>Keiichiro Urabe</u>, Hideki Motomura, Osamu Sakai, and Kunihide Tachibana, "*Observation of He_2 Molecular Emission at Intersection of IR Laser Beam and Plasma Plume in DBD Microplasma Jet*", 6th International Workshop on Microplasmas, B16 (Paris, France, April 2011), Poster presentation.

2.11. <u>Keiichiro Urabe</u>, Keitaro Yamada, and Osamu Sakai, "*Discharge-mode transition of jet-type dielectric barrier discharge in mixed flow of argon gas and acetone vapor*", 20th International Symposium on Plasma Chemistry, ATM01 (Philadelphia, USA, July 2011), Poster presentation.

2.12. <u>Keiichiro Urabe</u>, Keitaro Yamada, and Osamu Sakai, "*Extraordinary properties of dielectric barrier discharge in argon gas flow triggered by molecular impurities*", 64rd Gaseous Electronics Conference, number (Salt Lake City, USA, November 2011), Oral presentation.

2.13. <u>Keiichiro Urabe</u>, Brian L. Sands, Osamu Sakai, and Biswa N. Ganguly, "*Spectrally filtered ICCD-camera imaging of dielectric barrier discharge plasma jet using two crossed gas flows*", 64rd Gaseous Electronics Conference, number (Salt Lake City, USA, November 2011), Poster presentation.

[3. Domestic Conference (presented by the author)]

3.1. <u>Keiichiro Urabe</u>, Yosuke Ito, Makoto Kubo, Osamu Sakai, and Kunihide Tachibana, "*Jet shape and electrode dependence of the low-temperature plasma jet at atmospheric pressure* ", 54th Spring Meeting of the Japan Society of Applied Physics, 29a-G-3 (Sagamihara, March 2007), Oral presentation.

3.2. <u>Keiichiro Urabe</u>, Yosuke Ito, Makoto Kubo, and Kunihide Tachibana, "*Diagnostics of Discharge Characteristics and Spectroscopic Measurements of Excited Species in Low-temperature Plasma Jet at Atmospheric Pressure using Covered Cable Electrodes*", 68th Autumn Meeting of the Japan Society of Applied Physics, 4p-ZB-3 (Sapporo, September 2007), Oral presentation.

3.3. <u>Keiichiro Urabe</u>, Yosuke Ito, Makoto Kubo, and Kunihide Tachibana, "*Time-resolved Spectroscopic Measurements of Excited Species in Low-temperature Plasma Jet at Atmospheric Pressure*", 25th Symposium on Plasma Processing, P1-05 (Yamaguchi, January 2008), Poster presentation.

3.4. <u>Keiichiro Urabe</u> and Kunihide Tachibana, "*Behavior of N_2^+ Ions in Low-temperature Plasma Jet at Atmospheric Pressure Measured by using Laser Induced Fluorescence*", 55th Spring Meeting of the Japan Society of Applied Physics, 28p-T-1 (Funabashi, March 2008), Oral presentation.

3.5. <u>Keiichiro Urabe</u>, Yosuke Ito, and Kunihide Tachibana, "*Influence of Substrate on Spatiotemporal Behavior of Low-temperature Plasma Jet at Atmospheric Pressure*", 69th Autumn Meeting of the Japan Society of Applied Physics, 4a-Y-2 (Nagoya, September 2008), Oral Presentation.

3.6. <u>Keiichiro Urabe</u>, Yosuke Ito, Yutaka Fukui, and Kunihide Tachibana, "*Influence of Substrate on Spatiotemporal Behavior of Low-temperature Plasma Jet at Atmospheric Pressure* II", 56th Spring Meeting of the Japan Society of Applied Physics, 1p-T-18 (Tsukuba, April 2009), Oral presentation.

3.7. <u>Keiichiro Urabe</u>, Joon-Young Choi, Yosuke Ito, Osamu Sakai, and Kunihide Tachibana, "*Spacially resolved diagnostics of electron density in atmospheric pressure plasmas using CO_2-lase heterodyne interferometry*", 70th Autumn Meeting of the Japan Society of Applied Physics, 9p-E-3 (Toyama, September 2009), Oral presentation.

3.8. <u>Keiichiro Urabe</u>, Joon-Young Choi, Yosuke Ito, Osamu Sakai, and Kunihide Tachibana, "*Spectroscopic Diagnostics of Electron Density Distribution inside Parallel-Plate Dielectric Barrier Discharge*", 57th Spring Meeting of the Japan Society of Applied Physics, 17a-ZC-8 (Hiratsuka, March 2010), Oral presentation.

3.9. <u>Keiichiro Urabe</u>, Brian L. Sands, Osamu Sakai, and Biswa N. Ganguly, "*Generation and time-resolved observation of jet-type dielectric barrier discharge using two crossed gas flows*", 71th Autumn Meeting of the Japan Society of Applied Physics, 14p-P4-8 (Nagasaki, September 2010), Poster presentation.

3.10. <u>Keiichiro Urabe</u>, Hideki Motomura, Osamu Sakai, and Kunihide Tachibana, "*Spectroscopic diagnostics of enhanced He_2 emission at intersection of IR laser beam and plasma plume in low-temperature plasma jet* ", 58th Spring Meeting of the Japan Society of Applied Physics, 24a-P10-1 (Atsugi, March 2011), Poster presentation.